UNIVERSITY OF CATANIA

DEPARTMENT OF CHEMICAL SCIENCES

INTERNATIONAL PhD IN CHEMICAL SCIENCES – XXXI CYCLE

Ivana Di Bari

Photoresponsive nanosystems for therapeutic applications

PhD Thesis

Tutor: Prof. S. Sortino

Dr. G.M.L. Consoli

PhD Coordinator:

Prof. Salvatore Sortino

Abstract

Oncological and bacterial diseases are certainly the most troubling illnesses of the twenty-first century, and the data in this regard are staggering. Indeed, anticancer chemotherapy is affected by low specificity/selectivity and undesired side effects, and drug resistance phenomena are responsible for the failure of many conventional treatments. Multidrug-resistant-bacteria (MDRB) infection is become another burden to modern healthcare. For such a reason, there is an increasing demand for the development of new strategies for anticancer and antibacterial treatments without antibiotics to save millions of lives every year.[1]

In this frame, the light-controlled generation of cytotoxic species, such as singlet oxygen ($^1O_2$) and nitric oxide (NO), by using appropriate photochemical precursors represents a fascinating and unconventional approach for the treatment of cancerous and microbial diseases in non-invasive manner. However, many precursors have a hydrophobic nature, which favors their aggregation in aqueous medium strongly precluding their photochemical behavior.[2] The entrapment of drugs and pro-drugs in nanocarriers permits to overcome all these drawbacks and ensures protection from degradation, site-specific delivery, enhanced bioavailability, increased local concentration.

Here in are reported studies of two different types of nanocarriers carrying different photoactivable guests. The first part of this dissertation focuses on the achievement of novel photoresponsive calix[4]arene-based nanoconstructs which vehicle, by not covalent or covalent approach, different kinds of chromophores. The second part concerns the design, synthesis, antitumoral and antibacterial activity of polymersomes containing a nitric oxide photoprecursor by covalent and non-covalent approach.

Table of contents

General aims of the project

The final goal of this research project is the design, synthesis and characterization of photoresponsive nanosystems as therapeutic devices able to release the transient cytotoxic species NO and $^1O_2$ upon light activation for anticancer and antibacterial treatments. Specific attention is paid on water-soluble molecular systems, based on calixarenes and polymersomens, functionalized with suitable ligands able to recognize receptors overexpressed on the surface of cancer cells and/or promote the penetration in bacteria, which are typically characterized by an impermeable outer cell membrane. These systems are devised in order to exhibit either the single or simultaneous photo-stimulated release of the two cytotoxic agents.

Fabrication of these photoresponsive nanoconstructs implies collective cross-disciplinary efforts because of synthetic methodologies and physical characterization techniques. However, photochemistry plays a dominant role. In most cases, the systems are designed in order to avoid interchromophoric communication upon light excitation. It is important to note that, unlike non photoresponsive-molecules, the preservation of photophysical and photochemical properties of the chromophores in a confined region of the space is not a trivial result, but the logical consequence of the appropriate design of any specific component. The efficiency and the nature of any involved process, in fact, can be drastically affected by the energy and/or electron transfer mechanisms that preclude the ultimate goal.

1. Introduction and background

1.1. Antineoplastic Resistance

One of the main causes for the failure of an anti-cancer treatment is the development of drug resistance by the cancer cells.[3] This is a very serious problem that can lead to the reappearance of the disease and even death.

While it is quite common to think that the majority of cancers arise from a single precursor cell, it would be a mistake to think that a tumor is made up of all genetically identical cells. One of the characteristics of cancer is the increase in genetic instability and speed of mutation. These changes mean that the cells that are dividing, acquire genetic changes very quickly. Practically, this means that the cells of a tumor are similar, but they are not identical. When exposed to an anti-tumor drug, the sensitive cells die, while the resistant ones survive and multiply. The result is the re-growth of a tumor that is not sensitive to the drug used in origin. There are several reasons that can explain the existence of a first-resistant cell in the original tumor (Fig. 1).

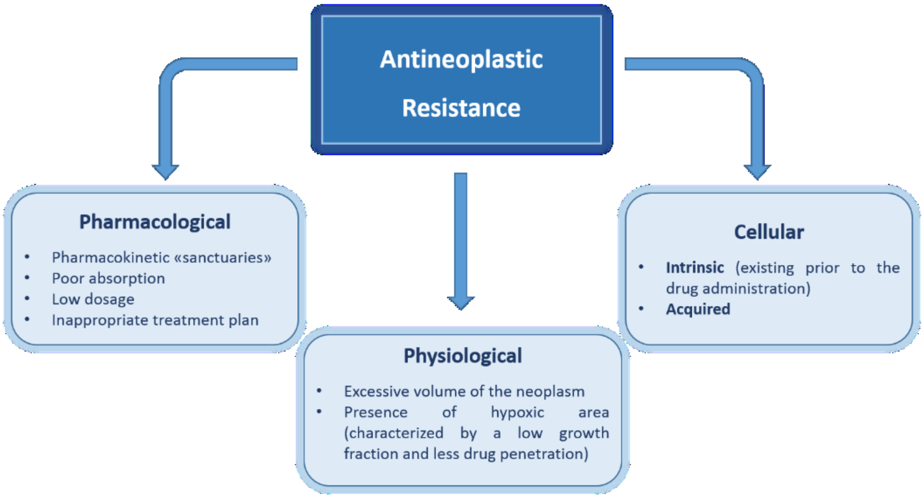

Fig. 1 Schematic representation of the main causes of resistance to antineoplastics.

The resistance in fact is established on the basis of anatomical and physiological factors. As an example when the cancer cells are confined into organs hardly accessible by the drugs, the so-called “sanctuaries” (for example, the central nervous system and testicle, due to the presence of the blood-brain barrier and the blood-testis barrier, respectively), the drug is not able to achieve or maintain cytotoxic concentrations for an appropriate period of time. In this case, the standard therapeutic scheme could result ineffective.

The drug resistance can also be induced by causes related to the peculiar physiology of the tumor mass. An excessive volume of the tumor determines in proximity of the same formation extensive ischemic areas, which make difficult both the drug release and the presence of oxygen in the proximity of the cancerous cells. Some antineoplastics cause cell death by the production of reactive oxygen species. Therefore, oxygen deficiency necessarily entails a reduction in activity.

There are also other factors typical of neoplastic cell, which oppose the action of antineoplastic drugs. These factors are responsible for intrinsic resistance, i.e. the resistance that develops during the first administration of the drug (a typical example of this is the *Multidrug Resistance*), or of secondary or acquired resistance, which occurs in tumor sensitive to a given molecule in the course of progression or recurrence of the disease. There are many types of intrinsic resistance mechanisms:

Decrease of intracellular transport: the intracellular concentration of a particular antineoplastic agent may be reduced due to an altered binding with a transport protein;

Increased extracellular drug transport: this mechanism has been described for many natural medicines, also called xenobiotics, such as vinca alkaloids, anthracyclines and epipodophyllotoxins. The increased outflow is due to the expression of specific proteins, which have the function of extruding xenobiotics from the inside of the cell. This mechanism is the basis of the phenomenon of multidrug resistance (MDR), i.e. of contemporary resistance to antineoplastic drugs with different structure and different mode of action;

Decreased activation of the drug: this mechanism interest drugs such as ARA-C (cytosine arabinoside) which for their operation require enzymatic activation. The cells are resistant to ARA-C because they are poor in kinase and phosphoribosyl-transferase (enzymes necessary for intracellular activation of the drug);

Increased inactivation of the drug.

For all these mechanisms and for many others, chemotherapy drugs come generally administered in combination. It is rather unlikely that a particular tumor cell will launch a mechanism of resistance to several drugs simultaneously, especially if the different administered drugs are active against different cellular processes, however, the large amount of cells present in a tumor mass makes the effect really possible.

1.2. Antimicrobial Resistance

After the development of penicillin in the 1940s, antibiotics have been used as “miraculous drugs” in clinical practice.[4] However, due to their extensive use in human, veterinary, and agricultural medicine, several bacterial strains have become resistant to numerous antibiotics. For this reason, the development of Antimicrobial Resistance (AMR) and MDRB (Multi drug resistance bacteria) have become critical issues not only in the battle against cancer, where antibiotics are crucial in helping chemotherapy patients to avoid and fight infections. Antimicrobial drugs in fact are medicines that are active against a range of infections, such as those caused by bacteria (antibiotics), viruses (antivirals), fungi (antifungals) and parasites (including antimalarials).

AMR arises when the micro-organisms which cause infection (e.g. bacteria) survive exposure to a medicine that would normally kill them or stop their growth. This allows those strains that are capable of surviving exposure to a particular drug to grow and spread, due to a lack of competition from other strains. This has led to the emergence of ‘superbugs’ such as Methicillin-resistant *Staphylococcus aureus* (MRSA) and extremely drug-resistant tuberculosis, bacteria which are difficult or impossible to treat with existing medicines. Fig.2 shows the trend of antibiotic-resistance for three common bacteria.

Resistance to antimicrobials is a natural process that has been observed since the first antibiotics were discovered and, indeed, the genes that confer drug resistance upon some strains of bacteria pre-date antibiotics by millions of years.

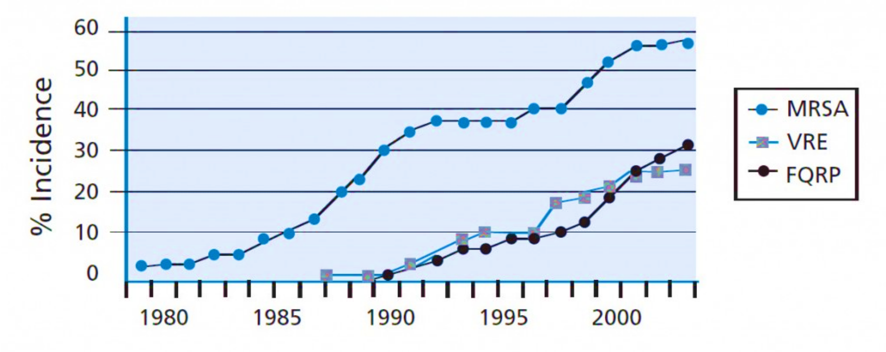

Fig. 2 The graph shows the rapid increase of the resistance of three species of bacteria: *Staphylococcus aureus* resistant to Methicillin (MRSA), Vancomycin-resistant *enterococci* (VRE), and *Pseudomonas aeruginosa* resistant to Fluoroquinolones (FQRP). - SOURCE: Center for Disease Control and Prevention. (IMAGE ADAPTED FROM[5])

However, AMR has increasingly become a problem in recent times because overuse of antimicrobials has increased the rate at which resistance is developing and spreading, but we lack new drugs to challenge these new superbugs. This results in us facing a growing enemy with a largely depleted armory.

In the past, resistant infections were predominantly associated with hospitals and care settings, but over the last decade resistant infections have been seen in the wider community too. With resistance on the rise, we stand to lose the immense ground we have gained in the last century. This includes: 1) the fight against life threatening infectious diseases such as pneumonia, TB, HIV and malaria; 2) the battle against conditions such as cancer; and 3) huge advances in surgical procedures like organ transplants and caesarean sections, which have now become routine and relatively low risk, thanks to our ability to effectively stave off or treat acute infections with antibiotics. It was estimated that in total about 700,000 people die every year from drug resistant strains of common bacterial infections, HIV, TB and malaria.[5] This number is likely to be an underestimate due to poor reporting and surveillance.

Based on scenarios of rising drug resistance for six pathogens to 2050, it was estimated that unless action is taken, the burden of deaths from AMR could balloon to 10 million lives each year by 2050, at a cumulative cost to global economic output of 100 trillion USD. On this basis, by 2050, the death toll could be a staggering one person every three seconds and each person in the world today will be more than 10,000 USD worse off.

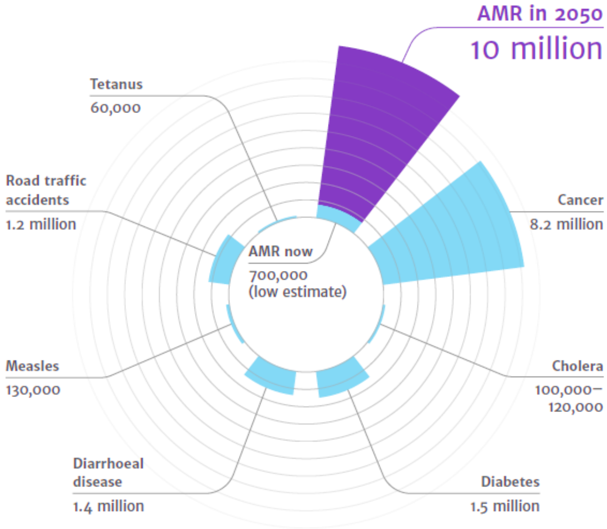

Fig. 3 Causes and number of deaths estimated to 2050. (IMAGE ADAPTED FROM[5])

It is impossible to predict the path of emerging drug resistance, but it is a trend that has largely run only in one direction so far. We can be certain that, in the absence of interventions to slow the emergence of resistance and increase the supply of new antibiotics, the impacts will be felt not just in isolated areas but at a far more fundamental level, across our societies and healthcare systems.

As the antibiotics available to us become less effective, so the risks of many treatments which rely upon antibiotics becomes higher. This will progressively undermine the viability of interventions that many may not directly associate with antibiotics. Cancer chemotherapy or organ transplantation are just two examples of medical treatments that leave the patient highly vulnerable to bacterial infections. Most invasive surgery (particularly ‘dirty’ procedures, such as those involving the gut) is today routinely and dependably ‘de-risked’ by effective antibiotic prophylaxis and by the availability of reliable therapy for infections that do occur despite best practices. Intubated patients in intensive care facilities already experience very high rates of infection, including drug-resistant ones, as a result of the ventilation that they receive and the mortality risk associated with this will rise further if treatment options for such infections deplete. These secondary impacts are difficult to quantify but they threaten to dramatically change healthcare as we know it today.[6]

1.3. Nanomedicine

In the early 1900s Paul Ehrlich thought to an ideal therapy a "*drug precisely targeted to an invader, which if linked to a toxic chemical would act like a missile, carrying a destructive payload directly to the disease"* but only in 1959 Richard Feynman invited all the scientific community to arrange the atoms as we want, looking beyond what our eyes can see. So only when we became able to manipulate atoms, the era of Nanotechnology was born. Nanometric scale materials showed different electrical, optical and magnetic properties respect to the bulk, giving the possibility to find new applications for these new materials.

Application of nanotechnology to medical science has been emerging as a new field of interdisciplinary research among medicine, biology, toxicology, pharmacology, chemistry, material science, engineering, and mathematics, and is expected to bring a major breakthrough to address several unsolved medical issues. Nanomedicine, namely the use of nanotechnology for medicine, is starting to make an impact in areas like disease imaging and diagnosis, drug delivery and as reporters of therapeutic efficacy and of disease pathogenesis. Many multifunctional nanostructures, capable of performing one or more of the above duties, are now in various stages of preclinical and clinical development.[7,8,9,10] Nanomedicine, represents an alternative approach[11] to oppose the development of resistance to antibiotics and anticancer drugs. Various systems able to assemble in nanosized structures, as biopolymers, macrocycles, liposomes, et al., are used to vehicle various molecules in cellular environment by exploiting supramolecular interactions for their transport and release. The entrapment of activatable agents in nanocarriers in fact can ensure their (i) solubilization in aqueous medium, (ii) protection from premature degradation, (iii) transport in the blood stream where dilution and interfering biomolecules are present, (iv) delivery to pathological cells by enhanced permeability and retention (EPR) effect and/or homing ligands exposed on the vehicle surface, (v) enhanced biocompatibility and bioavailability, (vi) increased local concentration, and (vii) sustained release. The selectivity and specificity in disease treatment can be enhanced by using externally activatable agents to produce localized cytotoxicity with minimized collateral damages. The ability to control the drug dosage in terms of quantity, location and time is a key goal for drug delivery science, allowing to maximize therapeutic effects. Systems responsive to stimuli such as temperature, pH, electric or magnetic applied field, ultrasound, light, or enzymatic action have been proposed as triggered delivery systems.[12]

1.4. Light stimulated therapy

In virtue of its simple manipulation in terms of wavelength, intensity and duration, low cost, low environmental impact, fast rate of photochemical processes, light represents the ideal external stimulus for the introduction of therapeutic agents in a desired bio-environment in a non-invasive way, mimicking an “optical microsyringe” with high spatio-temporal resolution. Moreover, it has the ability to not affect the values of physiological parameters such as temperature, pH and ionic strength, which is a prerequisite for biomedical application. For all these reasons activation of an appropriate precursor able to produce cytotoxic species under light stimulation represents an appealing strategy in biomedical field.

1.4.1. Photodynamic Therapy (PDT)

Photodynamic Therapy (PDT)[13] is a minimally invasive therapeutic approach in the treatment of cancer and infection diseases that involves the combination of visible light and a photosensitizer (PS). Each factor of this therapy (photosensitizer, light) is harmless by itself, but when combined with oxygen, can produce cytotoxic agents that can destroy cancer cells and bacteria.

PDT is based on the administration by intravenous, intraperitoneal or topical route, of a photosensitizing agent (PS) generally belonging to the class of porphyrins and phthalocyanines.[14] These species localize preferentially in diseased tissues, compared with normal cells, as only those cells that are simultaneously exposed to the photosensitizer, light and oxygen are exposed to the cytotoxic effect allowing to leave normal tissue intact.

After irradiation with opportune dose of appropriate wavelength light, the PS is excited and two different mechanisms can take place, Type I and II as reported in Fig. 4. In the Type II, which is the mechanism that takes place in PDT, the return to the ground state, starting from the lowest excited triplet state, occurs mainly by energy transfer to molecular oxygen generating highly reactive $^1O_2$, which induces damage and cell death.

This process competes with the radiative (fluorescence and phosphorescence) and not radiative (internal conversion) deactivation processes of the PS.

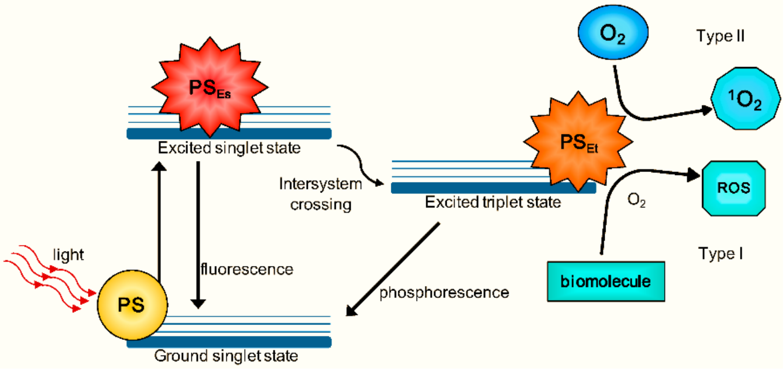

Fig. 4 Type I and Type II reactions in PDT (photodynamic therapy). Schematic Jablonski's diagram showing PDT's mechanism of action. Following light absorption, the PS reaches an excited singlet state. After an intersystem crossing, the PS, now in a triplet excited state, can react in two ways. It can react with biomolecules through a hydrogen atom (electron) transfer to form radicals, which react with molecular oxygen to generate ROS (type I reaction); or, it can react directly with oxygen through energy transfer, generating singlet oxygen (Type II reaction). (IMAGE ADAPTED FROM[15])

$^1O_2$ is one of the major cytotoxic agents produced by light excitation for treatment of many infectious and oncological diseases. This species is able to attack biological substrates of different nature like the plasma membrane, the mitochondria and the cell nucleus, and does not suffer Multidrug Resistance problems, typical for many anti-cancer and antibacterial drugs. Further, due to its short half-life in blood (μs), lack of charge and small sizes, $^1O_2$ diffuses in cellular environment over short distances (up to 150 nm), confining its region of action to the irradiated area and minimizing systemic side effects.[16]

1.4.2. Nitric oxide based therapy

NO, a small free radical, is involved in many physiological and pathological[17] processes such as stimulation of the immune system, smooth muscle relaxation[18], inhibition of platelet aggregation[19], inflammatory disorders[20], iron metabolism, neurotransmission and neurotoxicity[21] and vasodilatation[22] in living bodies. The role of nitric oxide in numerous dysfunctions has generated numerous debates in recent years and NO has been labelled as the causative agent of several pathophysiological mechanisms. However, it seems that it also protects against many chemical species, such as those generated by oxidation, and seems to be related to the tumoricidal and antibacterial activity of the immune system. The multifaceted role of NO is complex and its effects in many biological processes and in cancer biology[23] has attracted considerable interest. Several studies have associated NO production by immune cells, endothelial cells and others able to release NO to various aspects of anti-cancer therapy[24], such as the inhibition of cancer cells proliferation, angiogenesis and metastasis. Difficulties in the delivery of gaseous NO to selected targets have inspired the development of a range of NO releasing molecular and macromolecular scaffolds[25] as potential therapeutics that exploit NO's multifaceted biological roles, with the ambitious prospect to tackle important pathologies, including, of course, oncological and bacterial diseases. The biologic effects of NO are, however, strictly dictated by its concentration, delivery site and dosage, creating a complex role for the molecule in opposing beneficial and deleterious events.[26]

NO, as well as $^1O_2$, shows more or less the same properties respect to conventional drugs, but has a half-life in tissues of ca. 5 s and diffuses in the range of 40-200 µm, allowing to act on a wider range of action.

Furthermore, NO photorelease is independent from O_2 availability it can potentially very well complement the $^1O_2$ effects at the onset of hypoxic conditions typical of some tumors and infections by anaerobic bacteria. The possibility to obtain photo-activatable systems that are capable of releasing NO, conjugating the cytotoxic activity of the latter with the advantages offered by light stimulation, opens new perspectives for applications in bio-medical field.

1.5. Calix[n]arenes (CAs)

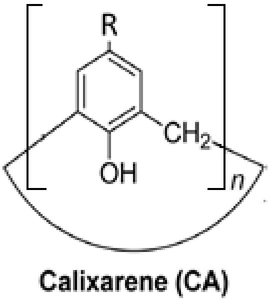

Fig. 5 CAs Structure.

Calix[n]arenes (CAs) (Fig. 5) have established their own status as the third generation of macrocyclic molecules. They are listed as one of the three major class of macrocyclic molecules together with cyclodextrins and crown ethers.

Typically, CAs are produced by chemical condensation between para-substituted phenols and formaldehyde. The phenolic units are linked by methylene bridges in *orto*-position to the OH groups. Because CAs with even numbers (n = 4, 6, 8) can be synthesized by one-step reaction and easily purified, they have been widely investigated. The distinctive feature of CAs is their cavity dimension according to the number of incorporated phenolic units.[27] Structurally, they contain two well defined rims (lower and upper rim) and an hydrophobic core (central annulus). Due to the presence of a hydrophobic cavity able to encapsulate many types of guests (small organic molecules, ions, sugars, etc), CAs are interesting host molecules in supramolecular chemistry.[28] The inclusion complexation is driven by various forces such as hydrophobic effect, ion-dipole interaction, and hydrogen-bonding interaction.

In the last decade, the favourable characteristics of CAs have been explored for diverse biomedical and pharmaceutical applications[29] as well as molecular recognition, sensing and self-assembly, catalysis and nanotechnology.[30] CAs have shown to have a great potential as drugs or drug delivery systems.[31] CA derivatives having activities such as anti-viral, anti-bacterial, enzyme activators/blocker, anti-coagulant, anti-cancer[32] etc. have been described. A few studies concern the application of CAs in anticancer PDT. A PEGylated bodipycalix(4)arene was proposed as a near infrared amphiphilic photosensitizer[33] and *p*-sulfonato-calix[6,8]arenes were found possess antitumor activity in a K562 myelogenous leukemia cell line irradiated with mercury light at 430 nm.[34] The photodynamic activity of a hydrophilic PEGylated calix[4]arene and a calix[4]arene–porphyrin forming supramolecular assemblies by host–guest interactions with chlorine6,[35] and biviologen derivatives,[36] respectively, was investigated on tumor cells *in vitro* experiments, but no photochemical and photophysical characterization of the nanostructured systems was carried out. To the best of our knowledge, calixarene–NO photodonor nanoassembly has never been investigated, some papers focused on calix[4]arene derivatives for storage of NO in the form of entrapped nitrosonium ions.[37] However, no reports on photoactivatable antibacterial systems based on calixarenes are known to date.

1.6. Polymersomes

Polymersomes (Fig. 6) are self-assembled polymer shells composed of block copolymer amphiphiles. The polymers used to make polymersomes are similar to lipids in that they are amphiphiles: at least one fraction or "block" of each molecule is hydrophilic, whereas the other fraction is hydrophobic. Either type of amphiphile, if made with suitable amphiphilic proportions, can self-assemble into vesicles when hydrated. The hydrophobic blocks of each molecule tend to associate with each other to minimize direct exposure to water, whereas the more hydrophilic blocks face inner and outer hydrating solutions and thereby delimit the two interfaces of a typical bilayer membrane. [1]The structure of the macromolecule is composed of three distinct regions (Fig. 6):

- Hydrophilic shell
- Hydrophobic bilayer
- Aqueous core.

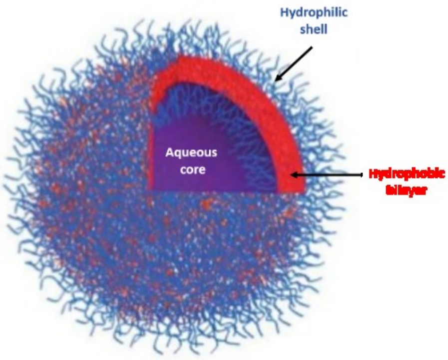

Fig. 6 Schematic representation of a polymersome structure.

This structure permits to load hydrophobic, hydrophilic or amphiphilic guests making these nanoconstructs an attractive supramolecular host to vehicle in contemporary different drugs and/or bio-active molecules with the aim to exploit additive and/or synergistic effects or multimodal therapeutic approach.[38,39]

Polymerosomes can be prepared from different polymeric building blocks from whose nature will depend the physical-chemical and biological properties of the resulting polymersomes, like dimensions,[40] encapsulation efficiency, pharmacokinetics including release rates,[41] degradability and cellular uptake.[42] Therefore, unlike the liposomes, polymersomes show a highest chemical versatility and tend to have a much ticker outer membrane owing to the higher molecular weight of the co-polymers used. The larger thickness of the membrane results in a greater stability and mechanical strength (Fig. 7).

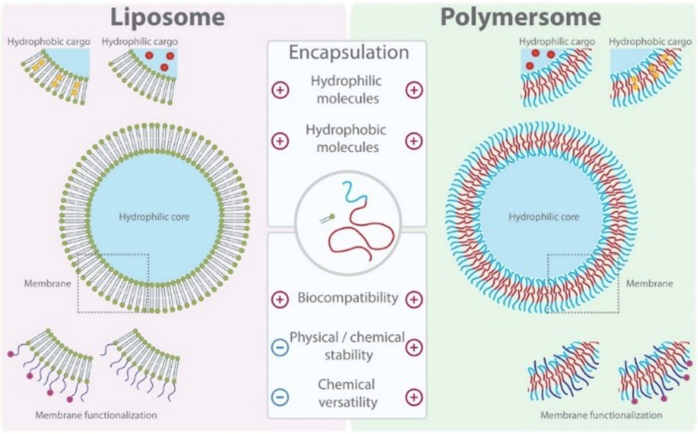

Fig. 7 Schematic representation of the advantages of polymersome respect to liposome.

Martin *et al.* have developed a charge neutral polymersome, using an amphiphilic PEGylated random copolymer, with an encapsulation efficiency of Fitc-CM-Dextran (Fluorescein isothiocyanate–Carboxymethyl–Dextran) of 70%, and the uptake of this guest by Hela cells was increased four-fold when encapsulated in the polymersomal system.[43] In literature, is well known that the use of PEG in nanoparticle preparations permits to enhance the circulation time in blood stream, reduce the aggregation in serum and prevents the elimination from reticuloendothelial system due to its immune-protection capabilities.[44,45,46]

However, it is also known that the PEGylation reduces cellular transfection and uptake due to interference with intracellular trafficking. A strategy to overcome these problems is the contemporary incorporation of PEG and lipid molecules such us cholesterol, since the latter is an essential structural component of cell membranes. Micelles and liposome formulated with cholesterol have shown increased cellular internalization, enhanced colloidal stability, higher encapsulation volume and slower release of payload compared to the ones without cholesterol.[47] For all these reasons FDA have only approved PEGylated liposomal drug delivery systems which incorporate cholesterol as a key component.[48] At this regard, recently Martin *et al*. have demonstrated that a polymersome containing an appropriate percentage of cholesteryl polymer showed a ten-fold increase in cellular uptake of Fitc-CM-Dextran compared to un-encapsulated drug.[38]

Part I

Calixarene-based photoresponsive nanosystems

2. Calixarene-based photoresponsive nanosystems entrapping different guests by non-covalent approach for antibacterial applications

2.1. Introduction

The good biocompatibility and low immunogenicity exhibited by water soluble calixarene derivatives, has paved the way for a variety of applications of these molecules in pharmaceutical and biomedical fields as drugs and/or drug delivery systems. With this in mind, we planned to synthesize the amphiphilic calix[4]arene scaffold **1** able to spontaneously self-assemblies in nano-sized aggregates, and to investigate the capability of the nanoconstruct to be a versatile supramolecular host and act as a nanocarrier of different types of photostimulable precursors.

In the first part of this study, the hydrophobic NO precursor **2** and two porphyrinoid PSs **4** and **5** were entrapped separately in the nanoaggregates of **1**. The calixarene-photostimulable supramolecular nanoassemblies represent novel potential antibacterial agents that under exclusive light-stimulation can produce cytotoxic species as singlet oxygen and nitric oxide radical useful in photodynamic therapy and NO-photostimulated therapy (Fig. 8).

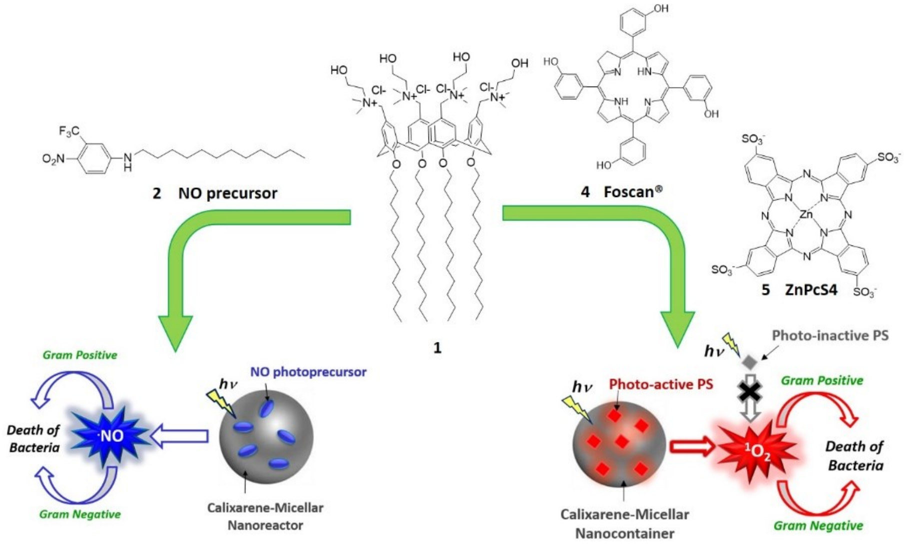

Fig. 8 Schematic representation of the photoresponsive calixarene-based nanosystems.

2.2. Results and discussion

2.2.1. Synthesis of compound **1**

The amphiphilic calix[4]arene **1** was synthetized by following the procedure reported in Fig. 9. In particular, commercial *p*-H-Calix[4]arene **6** was alkylated at the lower rim and chloromethylated at the upper rim in order to obtain derivative **10**, by passing through the formyl (**8**) and the alcohol (**9**) derivatives according the procedure reported by Eggers et al.[49] The treatment of compound **10** with *N,N*-dimethylethanolamine in THF as solvent gave compound **1**.[50] All the calix[4]arene derivatives were characterized by ^{1}H-NMR which agreed with the data reported in the literature.

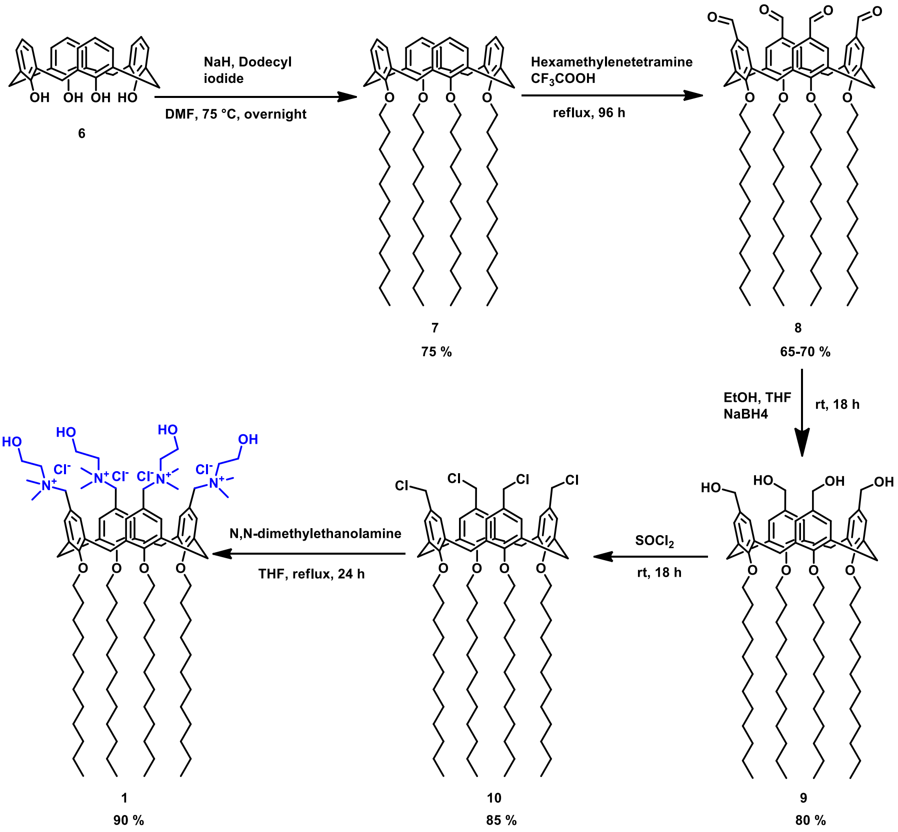

Fig. 9 Schematic representation of the synthetic steps involved in **1** obtaining.

2.2.2. *Synthesis of compound* **2**

The hydrophobic NO precursor **2** was synthetized starting from the commercial 4-Nitro-3-(trifluoromethyl)aniline treated with dodecyl iodide in CH_3CN (Fig.10). Compound **2** was characterized by ^{1}H-NMR and ^{13}C-NMR.

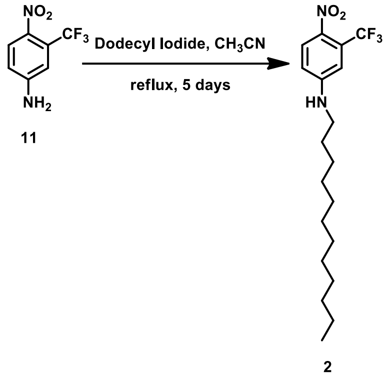

Fig. 10 Schematic representation of the synthesis of compound **2**.

2.2.3. *Characteristics of the components*

2.2.3.1. *Compound* **1** *– Calix[4]arene derivative*

Calix[4]arene **1** (Fig. 11) is characterized by the presence of four polar choline groups at the upper rim which confer solubility in aqueous environment and could favour cell membrane penetration by electrostatic interactions; and dodecyl chains at the lower rim which ensure an amphiphilic behaviour. Due to its structure this molecule has the capability to self-assemble in nano-sized systems and serve as supramolecular host for different guests.

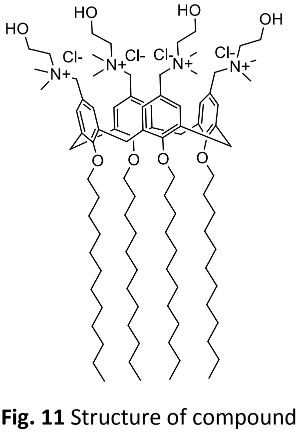

Fig. 11 Structure of compound **1**.

*2.2.3.2. Compound **2** – NO photoprecursor*

Compound **2** (Fig. 12A), a 4-nitro-3-(trifluoromethyl)aniline derivative, presents a dodecyl alkyl chain at the amino group useful to encourage the assembly with calix[4]arene **1** by hydrophobic interactions, in addition to the pie-pie interactions between the aromatic rings of the two partners.

Compound **2** as well as other derivatives is an eligible NO precursor because it is able to release NO under exclusive light stimulation.[51] The NO release mechanism (Fig. 12B) is based on a nitro-nitrite rearrangement with consequent formation of a phenoxy radical intermediate and a phenol derivative as a stable reaction product. The reason resides in the no-coplanarity of the nitro group respect to the aromatic ring due to the presence of the -CF3 substituent which brings an orbital overlap between the oxygen of the nitro group and one of the carbons of the aromatic ring.

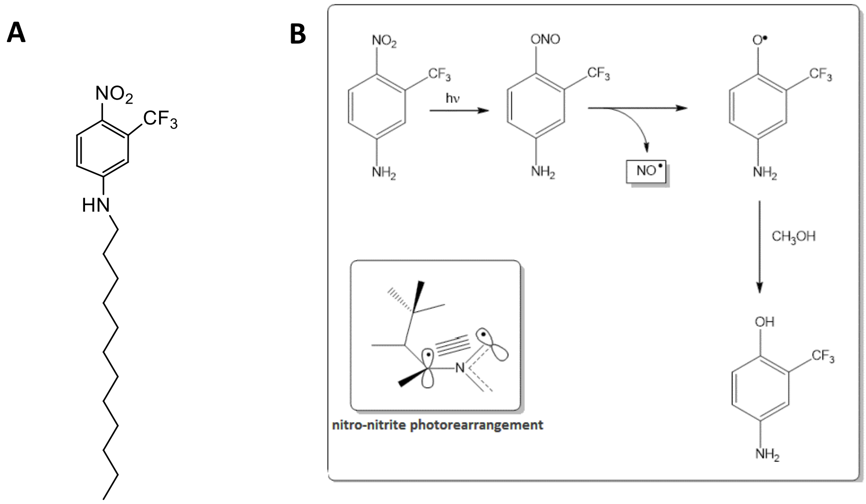

Fig. 12 (A) Structure of compound **2**. (B) Schematic representation of the NO-release mechanism.

2.2.3.3. Compound **4** *– Foscan®*

Foscan® (Fig. 13) is the brand name with which has been labeled in the European Union the Temoporfirin (INN), which is the common name of 3',3'',3'''(2,3-dihydroporphyrin-5,10,15,20-tetrayl)tetraphenol or more simply 5,10,15,20-Tetra(m-hydroxyphenyl)chlorin (*m*-THPC) a photosensitizer (based on chlorin) used in PDT for the treatment of squamous cell carcinoma of the head and neck. The EU approved its use in pharmacology in June 2001. Due to the poor solubility *m*-THPC can only be used with a formulation process prior to administration. Initial applications used formulations in PEG and ethanol or propylene glycol. Considerable effort has been spent on the preparation of nanocarrier formulations for *m*-THPC in fact in addition to the standard formulation (Foscan®) were prepared no-PEGylated and PEGylated liposomal formulations, Foslip® and Fospeg®.

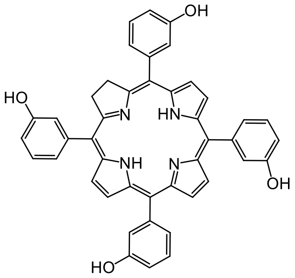

Fig. 13 Structure of compound **4**.

2.2.3.4. Compound **5** *– ZnPcS4*

Zinc phtalocyanine tetrasulfonate (Fig. 14) is a water soluble PS and allows its intravenous administration without the need for alternative delivery vehicles. The Zinc as the central metal ion confers short triplet lifetime, high triplet quantum yields and high singlet oxygen quantum yield. All these characteristics which make ZnPcS4 a suitable PS are precluded by aggregation phenomena in aqueous environment.

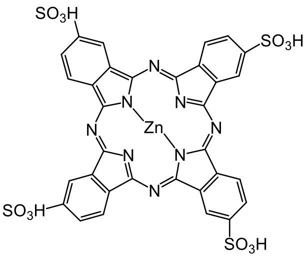

Fig. 14 Structure of compound **5**.

2.2.4. Characterization of the calix[4]arene **1***-based nanoassemblies*

Compound **1** due to its amphiphilic nature self-aggregates in 10 mM PBS solution, pH =7.4, at concentrations above ca. 8 µM, as demonstrated by the calculation of cac by pyrene method. The measurements were performed on aqueous solutions of **1** (from 0.5×10^{-6} M to 100×10^{-6} M) containing pyrene (0.3 µM) (Fig. 15A). Dynamic Light Scattering (DLS) measurements indicated an average hydrodynamic diameter of ca. 42 nm with a polydispersity index (PI) < 0.2 and a zeta potential ζ = +24.7 mV. TEM (Transmission Electron Microscopy) image confirmed approximately the dimensions acquired by DLS measurements and suggested that the calixarenes are aggregated in a micellar-like nanoassembly (Fig. 15B).

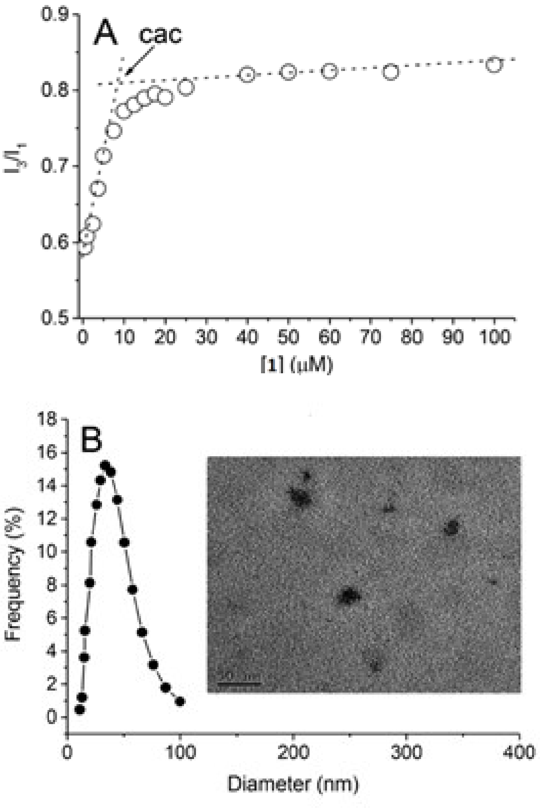

Fig. 15 (A) Intensity ratio I_3/I_1 of pyrene (0.3 µM) vs. the concentration of **1** in aqueous solution. The arrow indicates the critical aggregation concentration (cac). (B) Intensity weighted hydrodynamic diameter distribution of the micellar aggregates of **1** (300 µM) obtained by DLS. The inset shows a representative Transmission Electron Microscopy image of **1**.

2.2.5. Nanoassembly **1·2***: spectroscopic and dimensional characterization*

The hydrophobic structure of compound **2** makes this molecule totally insoluble in aqueous environment. We used the assembled compound **1** as a suitable nanocarrier to introduce compound **2** in PBS aqueous solution obtaining a light yellow colloidal dispersion.

In order to verify the efficient encapsulation of **2** in **1** we characterized the system by Uv-vis spectroscopy. The absorption spectrum of **2** entrapped in the calixarene aggregate shows the typical profile centered at 396 nm ca. which is approximately the same observed for the water soluble nitro-aniline derivative model compound **3**, at the same concentration (Fig. 16B). The amount of **2** loaded in **1** is ca. 8.3x10^{-5} M, which correspond to an EE of ca. 54% and a LC of ca. 22%.

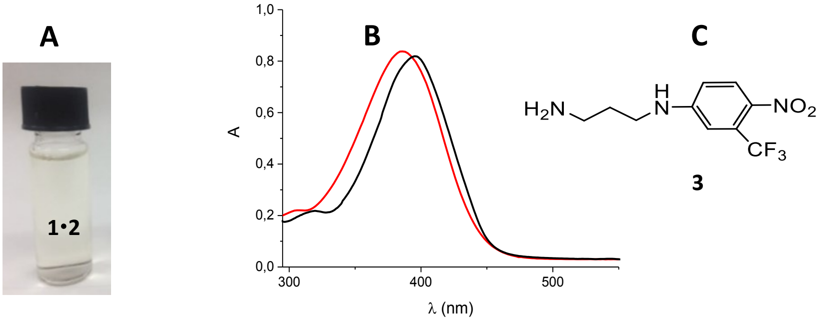

Fig. 16 (A) Picture of the **1•2** colloidal dispersion. (B) Absorption spectrum of **2** (83 μM) in phosphate buffer (pH 7.4, 10 mM) in the presence of **1** (300 μM) (black line) compared to absorption spectrum of the water soluble model compound **3** in PBS at the same concentration of **2**. (C) Structure of the model compound **3**.

DLS measurements (Fig. 17) have shown that the dimensions of the nanoassembly **1·2** are approximately the same of the empty NPs, distribution centered around 46 nm with a PDI = 0,24 and ζ = +23.7 mV, suggesting that the arrangement of the calixarene aggregates is not disrupted by the NO precursor loading.

DLS measurements have been repeated after 30 days and the data are about equal to those previously obtained, demonstrating the long-time stability of the system in PBS solution.

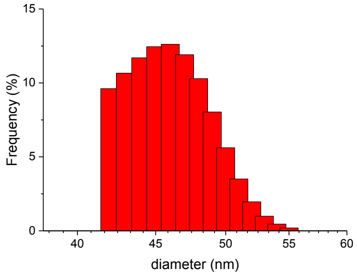

Fig. 17 Size distribution of the nanoassembly **1·2**.

2.2.6. NO photorelease from nanoassembly **1·2**

One of the most appropriate experimental methodologies to test NO photorelease capability of a system is to measure the concentration of NO species by an ultrasensitive electrode which directly detects NO with nM concentration. Irradiating with a 405 nm laser was monitored NO release by the samples, subjecting the photoactive component at regular intervals of light and darkness. The results illustrated in Fig. 18A provide evidence that the solution **1·2** and a PBS aqueous solution of **3** are stable in the dark and supply NO exclusively upon illumination with visible light. By comparison of the two NO release profiles is clear that the efficiency of NO photogeneration in the case of **1·2** is ca. 15 times higher than solution of **3**. It is possible to assert that the reason of this behaviour is due to the presence of calixarene scaffold which behaves as a nanoreactor probably producing a favourable low polarity environment and facilitating the extraction of close hydrogens to the phenoxy-radical intermediate involved in the NO photogeneration as previously described in section 4.3.2.

NO release issue of the solutions was further monitored by a photobleaching (Fig. 18B). Solution **1·2** was irradiated with a laser at 405 nm at regular intervals of 5 minutes. The absorbance profiles obtained show a clear reduction of the main signal relative to the formation of the phenol derivative as the only product obtained. This shows that there are not collateral or additional reactions which compete with the NO photorelease.

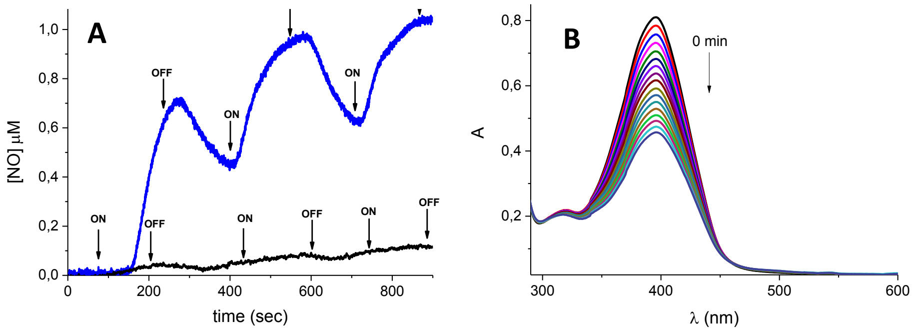

Fig. 18 (A) NO release profile observed for the nanoconstruct **1·2** (blue line, [**1**] = 300 μM; [**2**] = 83 μM) and an optically matched solution of the model compound **3** (black line) in water medium. λexc = 405 nm. (B) Absorption spectral changes observed upon 405 nm light irradiation of an aqueous solution of the nanoconstruct **1·2** ([**1**] = 300 μM; [**2**] = 83 μM) for regular irradiation intervals of 5 min.

2.2.7. *Antibacterial activity of nanoassembly* **1·2**

Antibacterial activity tests were performed at the SIFI S.p.A. by Dr. Blanco and Dr. Picciotto. Two different bacterial strains were chosen, *Staphylococcus aureus* ATCC 6538 and *Pseudomonas aeruginosa* ATCC 9027, as Gram positive and Gram negative bacteria, respectively. These two species have acquired a high antibiotic resistance towards traditional antibiotics and, in some forms, are responsible for serious nosocomial infections. The bacterial cultures were kept in the dark or irradiated at different times with a 470 W Xenon lamp equipped with a cut-off filter at 380 nm. In Fig. 19 are reported the time-inhibition curves obtained testing the antibacterial activity of **1** and **1·2** on both bacterial strains. It is evident that calixarene **1** did not have any effect, while the nanoassembly **1·2** shows an evident action dependent on the irradiation time. In fact, the colloidal dispersion containing compound **2** is able to induce an inhibition of the growth of approximately 100% for both bacteria after 30 minutes of irradiation. Control experiments carried out with normal human skin fibroblast cells showed a negligible (<15%) antiproliferative effect of **1·2** with concentrations identical to those in Fig. 19 and up to 30 min irradiation.

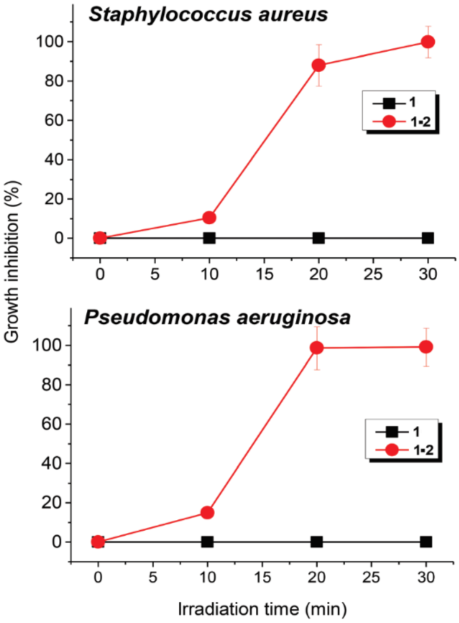

Fig. 19 Comparison of the time-inhibition curves of *Staphylococcus aureus* and *Pseudomonas aeruginosa* treated with **1·2** and, for comparison, **1** alone. [**1**] = 300 μM; [**2**] = 83 μM.

2.2.8. Nanoassembly **1·4***: spectroscopic and dimensional characterization*

In Fig. 20B is reported the absorption spectrum of compound **4** in methanol solution which shows the typical porphyrin profile characterized by an intense peak centered at 416 nm (Soret band or B-band) to which followers of lesser intensity at higher wavelengths (Q-Band signals). Compound **4** which is totally insoluble in phosphate-buffered aqueous solution becomes fairly soluble in the presence of aqueous dispersion of **1** giving a colloidal solution as confirmed by the typical spectrum profile shown in Fig. 20B. The amount of **4** loaded was 3 µM, corresponding to an EE of 100% ca.

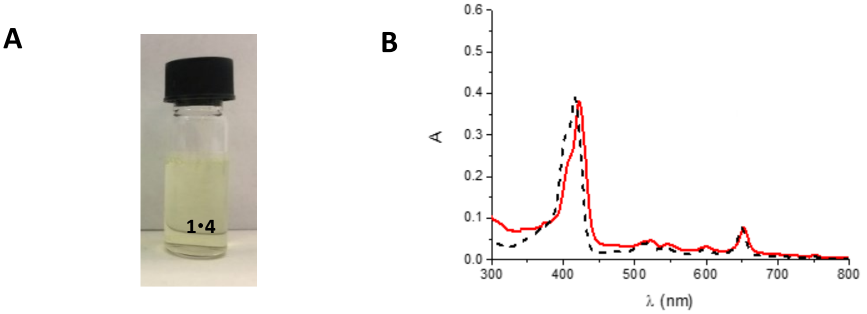

Fig. 20 (A) Picture of the colloidal solution **1·4** (B) Absorption spectra of **4** (3 µM) in methanol (dashed line) and in phosphate buffer (pH 7.4, 10 mM) in the presence of **1** (300 µM) (red line).

The efficient encapsulation is confirmed by the emission spectra acquired exciting at 590 nm that corresponds to third Q-Band of Foscan. As shown in Fig. 21, the emission profile of **4** in **1** shows a similar trend to that observed in methanol confirming the effective encapsulation of **4** within the calixarene assembly mainly under its monomeric form with a fluorescence quantum yield of $\phi_f = 0.053$.

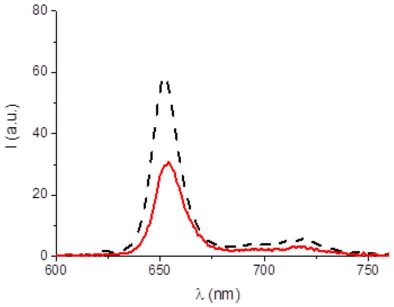

Fig. 21 Fluorescence emission spectra of **4** (3 µM) in methanol (dashed line) and in phosphate buffer (pH 7.4, 10 mM) in the presence of **1** (300 µM) (red line). λ_{exc} = 590 nm.

The dimensions of the system **1·4** obtained by DLS measurements (Fig. 22) gave a distribution centered around 90 nm with a PDI = 0.28 and a substantially unvaried value of the zeta-potential respect to the empty calixarene nanoparticles. The measurements performed again after 20 and 77 days from preparation, gave approximately the same values showing the long-time stability of the system.

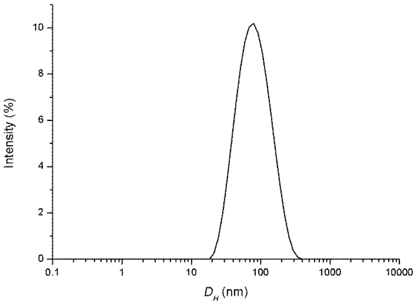

Fig. 22 Size distributions of the nanoassembly **1·4**.

2.2.9. Nanoassembly **1·5***: spectroscopic and dimensional characterization*

As shown in Fig. 23B the hydrophilic phthalocyanine PS **5** is soluble in PBS medium (10 mM pH=7.4) but in aggregated form. The aggregate shows an absorption spectrum centered at about 602 nm, while the profile in DMSO is characterized by an intense peak centered at 680 nm, relative to the monomeric species, preceded by a lower intensity peak relative to the aggregate one, as reported in literature.[52] Absorption spectrum obtained for **5** loaded in the calixarene nanoassembly **1** shows that the phtalocyanine is present almost totally in its monomeric form.

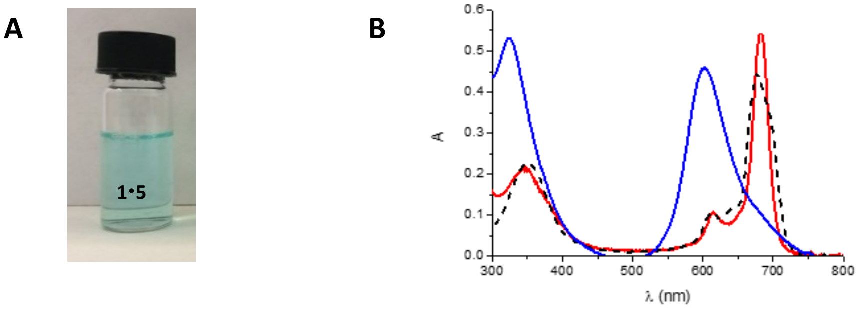

Fig. 23 (A) Picture of the colloidal solution **1·5**. (B)Absorption spectra of **5** (15 µM) in phosphate buffer (pH 7.4, 10 mM) in the absence (*blue*) and in the presence (*red*) of **1** (300 µM). Dashed line is absorption spectra of **4** in DMSO, where it is present as monomeric species.

As shown in Fig. 24, the fluorescence emission spectra of **5** in PBS solution is totally quenched due to the aggregation phenomena, while emission profile of **5** in **1**, though is lower in intensity, shows a similar trend to that observed in DMSO confirming the effective encapsulation of **5** within **1**, mainly under its monomeric form with a fluorescence quantum yield of $\phi_f = 0.031$.

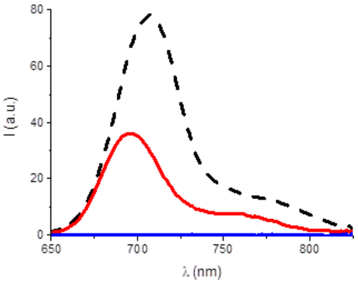

Fig. 24 Fluorescence emission spectra of **5** (15 µM) in phosphate buffer (pH 7.4, 10 mM) in the absence (*blue*) and in the presence (*red*) of **1** (300 µM). Dashed line is the spectrum of 5 in DMSO. λ_{exc} = 540 nm.

Dynamic Light Scattering measurements (Fig. 25) gave hydrodynamic diameters of ca. 100 nm for the system **1·5** with a PDI = 0.3. The size increase compared to the empty nanoparticles could be ascribed to a rearrangement of the calixarene assembly, and the presence of surface electrostatic interactions between the positive charges of the choline moieties and the negative charge of the phtalocyanine. This explanation agrees with a slight decrease of the zeta potential to a value ζ= + 20.8 mV. The measurements performed again after 20 and 77 days gave approximately the same values showing the long time stability of the system.

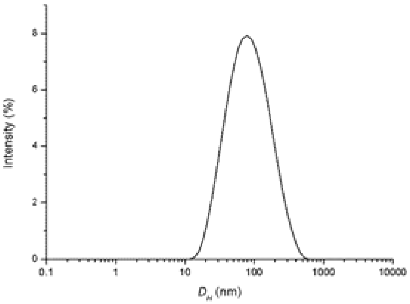

Fig. 25 Size distributions of the nanoassembly **1·5**.

Thanks to a collaboration with Dr. Conoci and Dr. Petralia of ST Microelectronics-Catania the supramolecular nanoassembly was also investigated by Atomic Force Microscopy (AFM). In Fig. 26 is reported the two-dimension topography (A) obtained by compound **1·5** and its height profile (B). AFM measurements show a smaller dimension for the aggregate **1·5** respect to DLS measurements probably due to the different type of environment in which the measurements are recorded.[53] In Fig. 26 C is reported the distribution which is centered about 25 nm.

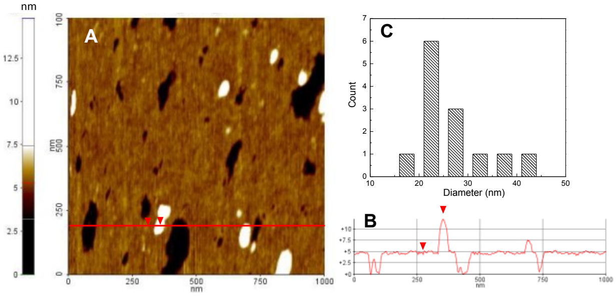

Fig. 26 A) Contact mode AFM of the supramolecular nanoassembly **1·5** deposited on cleaned silicon surface. B) Height line profile of line shown in A. C) Diameter distribution of the nanoassembly **1·5**.

2.2.10. $^1O_2$ photogeneration from **1·4** *and* **1·5** *nanoassemblies*

The generation of singlet oxygen, $^1O_2$, was detected by time resolving near infrared luminescence with sub-microsecond time resolution. We have examined the singlet oxygen produced by energy transfer from **4** and **5** to molecular O_2, in totally deuterated buffer solution of calix[4]arene **1.** The presence of the calixarene **1** permits to ensure the photochemical behaviour of the two PSs, otherwise precluded by low solubility and aggregation phenomena, in aqueous environment. Fig. 27 shows the typical phosphorescence signal at 1270 nm[54] observed for all samples investigated. The quantum yield for $^1O_2$ photogeneration, Φ_Δ, were 0.89 and 0.57 respectively. These values are significantly higher than those observed for **4** in methanol ($\Phi_\Delta = 0.43$)[55] and the **5** in CTAC micelles ($\Phi_\Delta = 0.31$)[56] and in DMSO ($\Phi_\Delta = 0.46$).[57]

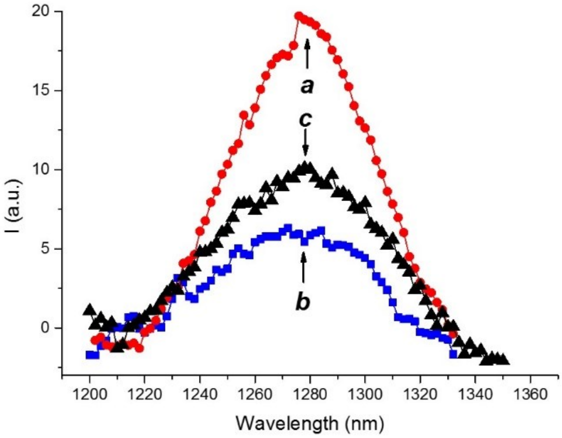

Fig. 27 $^1O_2$ luminescence detected upon excitation of the nanoassembly **1·4 at** λ_{exc} = 405 nm (***a***) and the nanoassembly **1·5** at λ_{exc} = 680 nm (***b***) in deuterated phosphate buffer (pH 7.4, 10 mM). The $^1O_2$ luminescence spectrum observed for **4** in methanol is also shown, for sake of clarity (**c**).

2.2.11. Antibacterial activity of the nanoassemblies **1·4** *and* **1·5**

Bactericidal action of **1·4** and **1·5** systems were performed by SIFI S.p.A. always on *Staphylococcus aureus* ATCC 6538 and *Pseudomonas aeruginosa* ATCC 9027, at the same conditions reported in the section relative to the antibacterial activity of **1·2.** The supramolecular nanoassemblies **1·4** and **1·5** did not show any significant action in the dark, but they exhibited a meaningful antibacterial activity under irradiation. No antibacterial activity was instead observed for the calix[4]arene nanoassembly alone (Fig. 28). The time-kill curves depicted in Fig. 28A, show that nanoassembly **1·5** has a faster antibacterial activity than **1·4** with total bactericidal effect in only 10 minutes of irradiation on both the bacteria strains. The reason of a greater slowness of **1·4** is could be due to a smaller fraction of absorbed light by the PS owing to the chemical filter used during the test which has a little absorption region in correspondence to that of the porphyrin **4.** In Fig. 28B and C we report two pictures relative to the plates containing *Staphylococcus aureus* ATCC 6538 and *Pseudomonas aeruginosa* ATCC 9027, respectively, treated with calixarene **1** alone and nanosystem **1·4** at different time of irradiation**.** It is evident that after five minutes, the system **1·4** shows obvious bactericidal effect on both bacteria, even if, as expected, *Pseudomonas* shows a greater resistance.

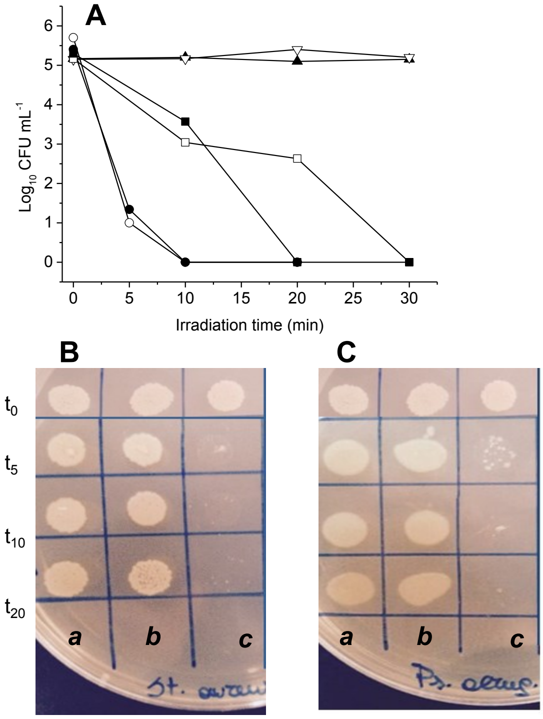

Fig. 28 (A) Time-kill curves of the nanoassembly **1·4** (squares), **1·5** (circles) and, for comparison, **1** alone (triangles) observed for *Staphylococcus aureus* ATCC 6538 (open symbols) and *Pseudomonas aeruginosa* ATCC 9027 (filled symbols). Representative images for the antibacterial effect observed on *Staphylococcus aureus* ATCC 6538 (B) and *Pseudomonas aeruginosa* ATCC 9027 (C) at different irradiation times of (***a***) control, (***b***) **1** and (***c***) **1·5**. [**1**] = 300 µM, [**4**] = 3 µM, [**5**] = 15 µM.

2.3. Experimental section

2.3.1. Materials

All reagents were of high commercial grade and were used without further purification. All solvents used were analytical grade. The PS **4** and **5** were purchased from Frontier Scientific Inc. (FSI) and Porphyrin Pdts, respectively and were used as received. *Staphylococcus aureus (ATCC 6538)* and *Pseudomonas aeruginosa (ATCC 9027)* were purchased from LGC Standards. Human skin fibroblast cells were obtained from biopsy after the informed consent of the subjects, according to the laws of the Italian Government and the Declaration of Helsinki Principles.

2.3.2. Synthesis

25,26,27,28-Tetradodecyloxycalix[4]arene (7)

p-H-Calix[4]arene **(6)** (5.72 g, 13.5 mmol) and 5.4 g NaH (60% dispersion in oil, 135 mmol) were stirred in 140 mL of dry DMF for 15 min under argon. Dodecyl iodide (33.2 mL, 135 mmol) was then added and the mixture was stirred at 75 °C overnight. DMF was removed under vacuum and 0.5 N HCl (200 mL) was added. After stirring overnight, the solid was recovered by filtration and washed several times with MeOH and small amount of acetone. This operation can be repeated to reach the desired purity of compound **7** (75 %).

5,11,17,23-tetra-formyl-25,26,27,28-tetra-dodecyloxy-calix[4]arene (8)

Under an inert gas atmosphere a mixture of compound **7** (3.3 g, 3 mmol) and hexamethylenetetramine (16.2 g, 120 mmol) in CF_3COOH (100 mL) was stirred for 96 h under reflux. The mixture was cooled to room temperature and then poured into a stirring solution of 2 M HCl (200 mL) and CH_2Cl_2 (200 mL), and vigorously stirred for 1 h. The mixture was extracted with CH_2Cl_2 (2 x 100 mL) and the combined organic layers were washed with saturated aqueous Na_2CO_3 (2 x 100 mL) and brine (2 x 100 mL), dried over sodium sulfate and the solvent was then removed under reduced pressure. The raw product was further purified by column chromatography (silica gel 60; hexane: ethyl acetate: CH_2Cl_2, 7:3:2) to give a white solid (2.73 g, 65-70%).

5,11,17,23-tetra-hydroxymethyl-25,26,27,28-tetra-dodecyloxy-calix[4]arene (9) Under an inert gas atmosphere ethanol (50 mL) was added to a stirring solution of **8** (2.73 g, 2 mmol) in THF (10 mL). $NaBH_4$ (2.6 g, 70 mmol) was then added and the mixture stirred for 18 h at room temperature. The mixture was then concentrated under vacuum and the resulting solid dissolved in CH_2Cl_2 (100 mL). 2 M HCl (100 mL) was added slowly and the solution was stirred for 1 h. The reaction mixture was then extracted with CH_2Cl_2. The combined organic fractions were washed with 2 M HCl (3 x 100 mL) and dried over Na_2SO_4. The solvent was removed *in vacuo* to obtain a white solid (1.5 g, 80%).

5,11,17,23-tetra-methylchloride-25,26,27,28-tetra-dodecyloxy-calix[4]arene (10) Under an inert gas atmosphere thionylchloride (2 mL) was added to calix[4]arene derivative **9** (0.5 g, 0.4 mmol) and then stirred at room temperature for 18 h. The mixture was concentrated under vacuum and the resulting solid was dissolved in CH_2Cl_2 (50 mL), washed with saturated aqueous Na_2CO_3 (3 x 50 mL) and dried over Na_2SO_4. The solvent was removed under reduced pressure to obtain an off-white solid (0.436 g, 85%).

5,11,17,23-Tetra(*N*,*N*-dimethyl-*N*-hydroxyethylammonium)-methylene-25,26,27,28-tetradodecyloxycalix[4]arene tetrachloride (1)

A solution of *N,N*-dimethylethanolamine (1.33 g, 1.5 mL, 14.9 mmol) in THF (15 mL) was added to a stirring solution of **10** (4.1 g, 3.2 mmol) in THF (60 mL). The reaction mixture was refluxed for 24 h. After cooling, the suspension was centrifuged at 4000 rpm, 5 min. The precipitate was washed with THF (40 mL) and with acetonitrile (4 x 20 mL) by repeated centrifugation (4000 rpm, 5 min) and removal of the solvent. The solid precipitate was recovered and dried under vacuum to give a white compound (4.7 g, yield: 90%). 1H-NMR (MeOD): δ 0,91 (t, 12 H, J = 6.8 Hz, 4 x CH_3), 1,31 (br m, 64 H, 32 x CH_2), 1,47 (br t, 8 H, 4 x CH_2), 2,01 (t, 8 H, J = 7.0 Hz, 4 x CH_2), 2,98 (s, 24 H, 8 x CH_3), 3,39 (br t, 8 H, 4 x CH_2N), 3,41 and 4,52 (AX system, 4 H each, J = 13,2 Hz, 4 x CH_2), 3,97-4,03 (overlapped, 16 H, 4 x OCH_2 and 4 x CH_2OH), 4,50 (s, 8 H, 4 x $ArCH_2$), 7,04 (s, 8 H, 8 x ArH).

***N*-dodecyl-4-nitro-3-(trifluoromethyl)aniline (2)**

4-Nitro-3-(trifluoromethyl)aniline **(11)** (200 mg, 0.96 mmol) was dissolved in acetonitrile (20 mL) and dodecyl iodide (0.92 mL, 3.72 mmol) was added. The reaction mixture was stirred at reflux for 5 days. The solvent was removed under vacuum and the solid was purified by preparative TLC (CH_2Cl_2/hexane 7:3) to give compound **2** as a yellow solid. ^{1}H NMR ($CDCl_3$): δ 0.88 (t, 3 H, *J* = 7.0 Hz, CH_3), 1.26 (br s, 16 H, CH_2), 1.42 (m, 2 H, CH_2), 1.66 (m, *J* = 7.0 Hz, 2 H, CH_2), 3.20 (m, *J* = 7.0 Hz, 2 H, CH_2), 4.56 (br t, 1H, NH), 6.63 (dd, *J* = 9.0 and 2.6 Hz, 1 H, ArH), 6.86 (d, *J* = 2.6 Hz, 1 H, ArH), 8.02 (d, *J* = 9.0 Hz, 2 H, CH_2). ^{13}C-NMR ($CDCl_3$): δ 13.9 (q), 22.6, 26.8, 28.7, 29.1, 29.2, 29.3, 29.4, 29.5, 31.8, 43.4 (t), 110.9, 111.0, 112.2 (d), 120.8, 129.0, 136.4, 151.7 (s).

2.3.3. *Preparation of the nanoassemblies*

Nanoassembly **1•2**. Calixarene **1** (5 mg, 3 × 10-4 M) and compound **2** (0.58 mg, 1.55×10^{-4} M) were dissolved in 10 mL of 10 mM PBS, pH 7.4. The mixture was vortex, sonicated for 15 min and stirred for 48 h, at rt. Then, the colloidal solution was filter through a 0.2 µm filter (GHP, Acrodisc) to remove unentrapped compound **2**. The amount of **2** entrapped in the nanoassembly of **1** after filtration was determined spectrophotometrically at 396 nm (ε= 10.000 M^{-1} cm^{-1}). Encapsulation efficiency (EE %) and drug loading capacity (LC %) were calculated using the formulae below:

$$EE\ \% = (W_{IN}/W_i) \times 100$$

$$LC\% = W_{IN} / (W_{IN} + W_{NP}) \times 100$$

where W_{IN} is the amount of drug in the nanoassembly, W_i is the total amount of drug added initially during preparation, and W_{NP} is the amount of calixarene in the nanoassembly.

Nanoassembly **1·4**. For the preparation of the nanoassembly **1·4**, compound **4** was firstly dissolved in methanol and slowly evaporated to form a thin film. The film was then hydrated with a phosphate buffer solution of **1** (5 mg, 300 µM). The mixture was stirred for 10 days at room temperature and then filtered with 0.2 µm filter to remove any unentrapped compound **4**.

Nanoassembly **1·5**. The supramolecular nanoassembly **1·5** was prepared by mixing the calixarene **1** (5 mg, 300 µM) and compound **5** (15 µM) in 10 mL of 10 mM phosphate buffer, pH 7.4. The mixture was stirred for 15 days at room temperature and then filtered with 0.2 µm filter (GHP, Acrodisc) to remove any residual aggregate form.

2.3.4. Instrumentation

Spectra ^1H and ^{13}C NMR were recorded on a Bruker Avance 400.13 and 100.61 MHz, respectively.

The unstained specimens for the electron microscopy were prepared by placing a drop of calixarene **1** (1 mg/mL) on copper TEM grids coated with a thin amorphous carbon film. The grids were dried in air and the dried specimens were examined by a JEOL transmission electron microscope, using an accelerating voltage of 200 kV, at room temperature.

UV-Vis spectra absorption and fluorescence emission spectra were recorded with a JascoV-560 spectrophotometer and a Spex Fluorolog-2 (mod. F-111) spectrofluorimeter, respectively, in air-equilibrated solutions, using either quartz cells with a path length of 1 cm.

Irradiation of the samples in solution was performed in a thermostated quartz cell (1 cm pathlength, 3 mL capacity) under gentle stirring, by using a continuum laser with λexc = 405 nm (ca. 100 mW) having a beam diameter of ca. 1.5 mm.

$^1O_2$ emission was registered with the same spectrofluorimeter equipped with a NIR-sensitive liquid nitrogen cooled photomultiplier, exciting the air-equilibrated samples of the nanoassemblies **1·4** and **1·5** at 405 nm with a 200 mW continuum laser or at 680 nm with the fluorimeter lamp, respectively.

DLS measurements of **1·2** were performed on Horiba LS 550 apparatus equipped with a diode laser with a wavelength of 650 nm, whereas DLS measurements of assemblies **1**, **1·4** and **1·5** and zeta potential measurements of all systems were performed with a ZetaSizer NanoZS90 Malvern Instrument (UK), equipped with a 633 nm laser. (Scattering angle = 90°, T = 25 °C).

AFM images of **1·5** were acquired in air by using a Digital 3100 in tapping mode. Commercially available tapping etched silicon probes (Digital) with a pyramidal shape tip having a nominal curvature of 10 nm and a nominal internal angle of 35◦ were used. The samples for AFM analysis were prepared as a follows: an aliquot (10 µl) of the nanoassembly solution a was deposited on freshly cleaned Silicon flat substrate (silicon substrate was cleaned by Plasma-O_2 process for 10 min at 100W). Afterwards, the residue liquid on the surface was removed. The sample was dried in air before the measurement.

NO release for samples in solution was measured with a World Precision Instrument, ISO-NO meter, equipped with a data acquisition system, and based on direct amperometric detection of NO with short response time (< 5 s) and sensitivity range 1 nM – 20 µM. The analog signal was digitalized with a four-channel recording system and transferred to a PC. The sensor was accurately calibrated by mixing standard solutions of $NaNO_2$ with 0.1 M H_2SO_4 and 0.1 M KI according to the reaction:

$$4H^+ + 2I^- + 2NO_2^- \rightarrow 2H_2O + 2NO + I_2$$

Irradiation was performed in a thermostated quartz cell (1 cm pathlength, 3 mL capacity) using the above continuum laser with λ_{exc} = 405 nm. NO measurements were carried out under stirring with the electrode positioned outside the light path in order to avoid NO signal artefacts due to photoelectric interference on the ISO-NO electrode.

2.3.5. Determination of fluorescence and $^1O_2$ quantum yield

Fluorescence quantum yields were determined by using optically matched solution at the excitation wavelength of the nanoassemblies and the standard. solution **C.** Compound **4** in MeOH ($\phi_f = 0.095$)[58] and **5** in DMSO ($\phi_f = 0.07$)[59] were used as a standard for **1·4** and **1·5**, respectively. The values of ϕ_f were determined by using the following equation:

$$\phi_f = \phi f(s)\ (In^2 / In^2(s))$$

where $\phi_f(s)$ is the fluorescence quantum yield of the standard; I and I(s) are the areas of the fluorescence spectra of the compounds and the standard, respectively; n and $n_{(s)}$ are the refraction index of the solvents used for the compounds and the standard. In any case the absorbance at the excitation wavelength were less than 0.1.

$^1O_2$ quantum yield were determined by using optically matched solution at the excitation wavelength of the nanoassemblies and the standard. Compound **4** in methanol ($\Phi_\Delta = 0.43$)[55] and Methylene blue in CH_2Cl_2 ($\Phi_\Delta = 0.57$)[60] and were used as a standard for **1·4** and **1·5**, respectively . The values of Φ_Δ for the nanoassemblies were determined by using the following equation:[61]

$$\phi_\Delta = \phi_{\Delta\,(s)}\ (In^2 k_{r(s)} / I_{(s)} n^2_{(s)} k_r)$$

where $\phi_{\Delta(s)}$ is the $^1O_2$ quantum yield of the standard, I and $I_{(s)}$ are the areas of the emission spectra of the nanoassembly and the standard, respectively; k_r and $k_{r(s)}$ are the $^1O_2$ radiative rate in the solvents used (ref) for the compound and standard; n and $n_{(s)}$ are the refraction index of the solvents used for the compound and the standard.

2.3.6. Antibacterial experiments

The day before performing the experiments, pure cultures were inoculated in 100 mL Nutrient Broth and incubated (37^0 C, 24 hrs) to allow complete growth in the liquid growth medium. The overnight incubated broth culture was centrifuged at 4000 rpm for 15 minutes. Supernatant Nutrient Broth was discarded leaving bacterial pellet at the bottom of the centrifuge tube. PBS (5 mL) was added to the tube and the bacterial pellet was washed by shaking it gently. The washed pellet was again centrifuged at 2933 × g for

15 minutes. The pellet thus formed was then diluted with PBS. For experiment with **1** and **1·2**, bacteria were inoculated in 96 well plate to yield a final inoculum of 1.5 × 10^5 CFU mL^{-1} for Staphylococcus aureus and 1.9 × 10^5 CFU mL^{-1} for Pseudomonas Aeruginosa. Then calixarene **1** only and **1·2** were added. For experiment with **1·4** and **1·5**, bacteria were inoculated in 96 well plate to yield a final inoculum of 2-5 × 10^5 CFU mL^{-1} for both bacteria. Then nanoassemblies **1·4** and **1·5** were added.

For both experiments two different control samples were also prepared in PBS and Mueller Hinton.

Before exposure to light, the samples to be irradiated were incubated in dark for 30 minutes. 15 µL of each sample was taken and seeded as a spot in a ground plate of Mueller Hinton supplemented with agar (time t_0). Irradiation was performed with a Xenon Lamp SUNTEST 470 W lamp mounting a cut-off filter at 400 nm. The light source was designed in such a way so as to fit over the 5 cm culture plate with a fixed distance of irradiation of 15 mm. The surface temperature of the samples was continuously recorded in order to avoid any significant rise in temperature. At different time, 15 µL of each sample was taken and seeded as a spot in a ground plate of Mueller Hinton supplemented with agar. The viability count for each sample was done in duplicate plates. The % of growth inhibition was calculated by the following equation:

$$\text{Growth inhibition \%} = [1 - (\text{CFU } t_x / \text{CFU } t_0)]100$$

2.3.7. Phototoxicity assay

The photocytotoxicity experiments were carried out by irradiating human skin fibroblast cells incubated with **1·2** for 30 min (with the same lamp used for the antibacterial tests). Call proliferation was assessed by MTT assays, based on the conversion of a substrate containing tetrazolium ring to spectrophotometrically-detectable formazan by mitochondrial dehydrogenases. Briefly, cells were seeded at an initial density of $8x10^3$ cells per microwell in flat-bottomed 200 µL microplates and incubated at 37 °C in a humidified atmosphere containing 5% CO_2 for 24 hours. Subsequently, some cells were maintained as media controls, while others were incubated with **1•2**. In both cases, complete DMEM without phenol red was used 20 µL of 0.5% 3-(4,5-dimethyl-thiazol-2-yl)2,5-diphenyl-tetrazolium bromide in PBS was then added to each microwell. Following 4 h of incubation at 37 °C, the supernatant was removed and replaced with 100 µL of DMSO. The optical density of the contents of each well was measured with a microplate spectrophotometer reader (Digital and Analog Systems, Rome, Italy) at 550 nm. Cell viability (%) was calculated from the following equation:

$$\text{Cell viability (\%)} = [A_{\text{Before}} - (A_{\text{After}}/A_{\text{Before}})] \text{ x } 100$$

Where A_{Before} and A_{After} are the absorbance value of the wells, treated with the samples solutions, before and after irradiation respectively.

3. Simultaneous supramolecular activation of NO photodonor/photosensitizer ensembles by a calix[4]arene nanoreactor

3.1. Introduction

The possibility to release NO independently from O_2 availability allows to achieve multimodal nanoconstructs able to release in contemporary NO and $^1O_2$ with the aim to be active under normoxic and hypoxic conditions. During this study in contemporary a PS, **4** or **5**, and NO photodonor **2** (NOPD) have been entrapped in the same micellar choline-calix[4]arene **1**. The preservation of the photophysical and photochemical properties of all components, even if co-entrapped in the same restricted area, is due to the lack of reciprocal interferences, that allow them to work independently under visible light excitation.

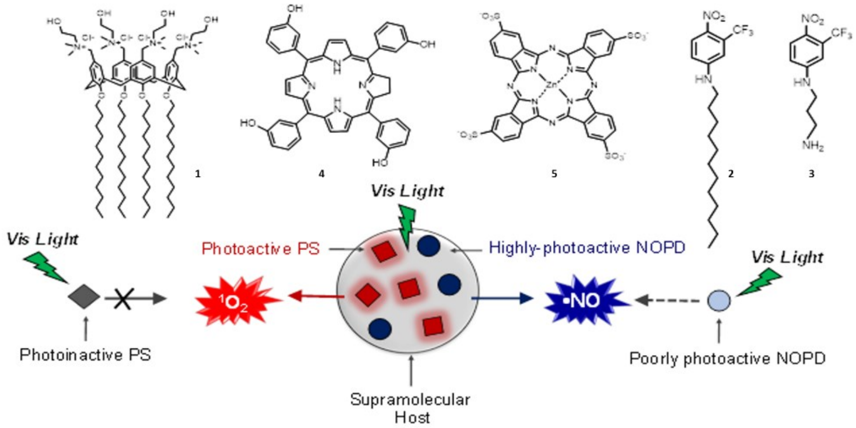

Fig. 29 Schematic representation of the photoresponsive calixarene-based nanosystems.

3.2. Results and discussion

3.2.1. Synthesis and characteristics of the components

Informations relative to this section are reported in the paragraphs *2.2.1.*, *2.2.2.*, *2.2.3.* and *2.2.4.*.

3.2.2. Spectroscopic and dimensional characterization of the nanoassemblies **1·2·4** *and* **1·2·5**

The entrapment of the chromophores in the micellar nanocarrier **1** has been monitored by Uv-vis and fluorescence emission spectra. The absorption spectrum (Fig. 30A) of **4** within **1** shows the typical profile centered around 400 nm. Compound **4** as well as **2** are totally insoluble in phosphate-buffered aqueous solution, but the absorption profile obtained for the nanoassembly **1·2·4** suggests an effective co-encapsulation of **2** and **4** within **1**.

The Fluorescence emission spectra profiles in Fig. 30B of **4** within **1**, in presence and in absence of **2**, show that the presence of NO donor does not influence the emissive properties of fluorophore. This data is confirmed by the fluorescence quantum yields of **4** with and without NO photodonor, which are ϕf = 0.052 and 0.053 respectively.

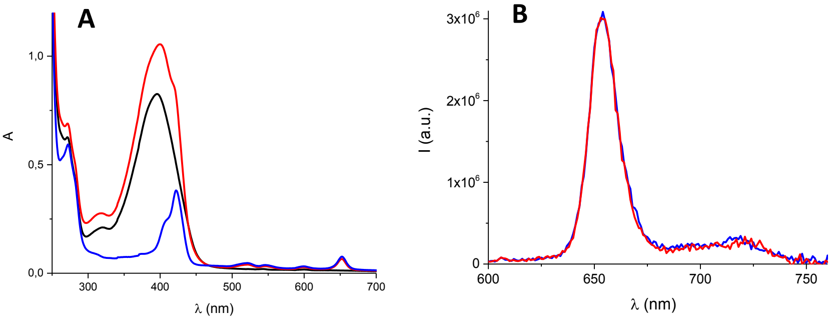

Fig. 30 (A) Absorption spectra of **1·4** (*blue*), **1·2** (*black*) and **1·2·4** (*red*). (B) Fluorescence emission spectra of **1·4** (*blue*) and **1·2·4** (*red*).

In the frame to obtain a bimodal systems able to release simultaneously $^1O_2$ and NO, it is important to underline that the generation of $^1O_2$ is based on photocatalytic process which, in principle, does not consume the PS. On the other side photogeneration of NO involves a photochemical reaction with consequent consumption of the precursor. Therefore, the concentration of the NO photoprecursor is the limiting NO concentration factor. For these reasons, in the preparation of **1·2·4** and **1·2·5** we planned to entrap in **1** an amount of **3** higher than that of **4** and **5**.

Encapsulation efficiency (EE%) was about 100 % for **4** and **5** whereas the EE% for **2** was 54 % (loading capacity 22 %) in **1·2·4** and 27 % in **1·2·5** (loading capacity 29 %).

As well as for **1·2·4** the encapsulation of the cromophores is visible at the naked eye by the colours of the colloidal solutions. Particularly, the co-encapsulation of **2** and **5** within **1** gives a green coloration that matched very well the combination of the yellow colours of **2** and the light blue of **5** as clearly visible in Fig. 31.

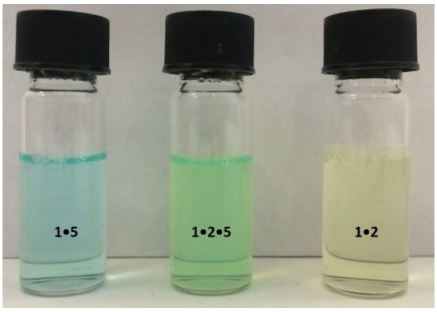

Fig. 31 Picture of the colloidal solutions of **1·5**, **1·2·5** and **1·2**.

Looking at the absorption spectra reported in Fig. 32A it is evident that in the case of the ternary complex **1·2·5**, the absorption of **2** at 399 nm is followed by the typical absorption band of the monomeric form of **5** at 680 nm.[24] This signal confirms that encapsulation in the micellar host breaks the aggregates of **5** in aqueous environment whose absorption is at 600 nm.

Emission spectra in Fig. 32B were acquired exciting at 540 nm and the obtained profile confirm the effective encapsulation of **5** within **1**, mainly under its monomeric form, independently from the presence of **2** or not. In fact, as found, also in this case the value of fluorescence quantum yield for **5** is the same for both samples, **1·5** and **1·2·5**, $\phi_f = 0.031$ and $\phi_f = 0.029$, respectively.

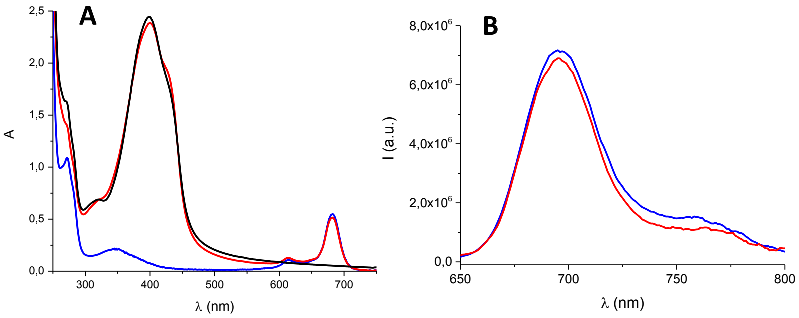

Fig. 32 (A) Absorption spectra of **1·5** (*blue*), **1·2** (*black*) and **1·2·5** (*red*). (B) Fluorescence emission spectra of **1·5** (*blue*), **1·2·5** (*red*).

The hydrodynamic diameters of the ternary supramolecular ensembles **1·2·4** and **1·2·5** were in the nanometric size regime being ca. 45 and 150 nm, respectively. Both the ternary nanoassemblies showed a polydispersity index of 0.2, indicative of a narrow size distribution in PBS medium. The zeta potential found for **1·2·4** (+23.7 mV) was the same for nanoassembly empty of **1**, while the value for **1·2·5** (+20.8 mV) was lower, according to the anionic structure of **5**, which can establish electrostatic interactions with the polycationic **1**.

3.2.3. NO photorelease from ternary **1·2·4** *and* **1·2·5** *nanoassemblies*

The NO photorelease properties of **2** are demonstrated by the direct and real-time monitoring of this transient species using an ultrasensitive NO electrode which directly detects NO with nM concentration sensitivity by an amperometric technique. The results illustrated in Fig. 33A and 33B provide evidence that all the colloidal solutions are stable in the dark and supply NO exclusively upon illumination with visible light. The same trends observed by the comparison of **1·2/1·2·4** and **1·2/1·2·5** show that the PS chromophores do not influence the capability of the NO photorelease.

It is very important to stress that the capability of the nanoassembly of **1** to act as a nanoreactor, amplifying of more than one order of magnitude the photochemical efficiency of the NO release, is also retained in the ternary complexes.

The spectral changes observed upon irradiation in Fig. 33C and 33D show a very clear bleaching of the main absorption band, attributed to the formation of a phenol derivative absorbing in the UV region as the sole stable product formed after NO photogeneration. At the same time no significant spectral changes are observed in the spectral region of the PSs, suggesting that no parallel reactions beside to the NO release and involving the PSs occur upon light-irradiation.

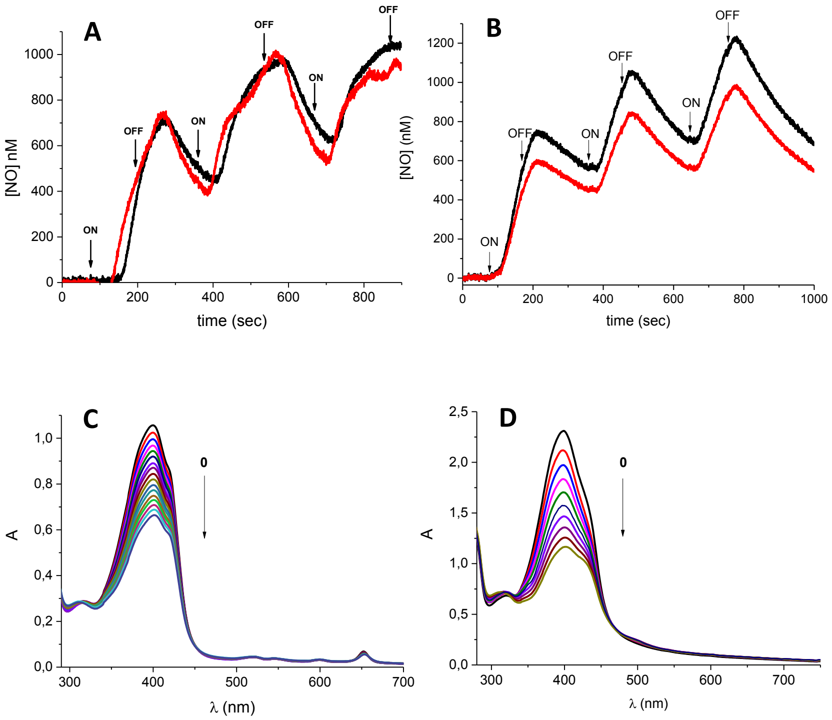

Fig. 33 NO release profile (PBS medium, λ_{exc} = 405 nm, 55 mW, 25 °C) of (A) **1·2·4** (*red*) and, for comparison, **1·2** (*black*) ([**1**] = 300 μM; [**2**] = 83 μM; [**4**] = 3 μM) and (B) **1·2·5** (*red*) and, for comparison, **1·2** (*black*) ([**1**] = 600 μM; [**3**] = 250 μM; [**2b**] = 15 μM).
Absorption spectral changes observed upon 405 nm light irradiation of **1·2·4** (C) and **1·2·5** (D) for regular irradiation intervals of 5 min (concentrations as in A and B, respectively).

3.2.4. $^1O_2$ photogeneration from ternary **1·2·4** *and* **1·2·5** *nanoassemblies*

The generation of singlet oxygen, $^1O_2$, was detected by time resolving near infrared luminescence with sub-microsecond time resolution. We have examined the singlet oxygen produced by energy transfer from **4** and **5** to molecular O_2, in totally deuterated buffer solution of calix **1** in presence of **2**. Fig. 34 shows the typical phosphorescence signal at 1270 nm[54] observed for both samples investigated. The quantum yield of $^1O_2$ (ϕ_Δ) for **4** in **1·2·4** and for **5** in **1·2·5** are 0.89 and 0.74 respectively.

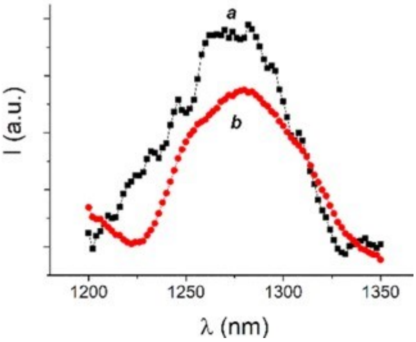

Fig. 34 $^1O_2$ luminescence detected upon excitation at λ_{exc} = 680 nm of the ternary complexes **1·2·4** (*a)* and **1·2·5** (*b*) in deuterated phosphate buffer (pH 7.4, 10 mM).

3.3. Experimental Section

3.3.1. *Materials*

All chemicals were obtained from commercial sources and used as received. Compound **4** was purchase from Frontier Scientific and **5** from Allorachem SRL and used without further purification. Choline-calix[4]arene **1** and tailored NO photodonor **2** were synthesized according to the procedures reported in Chapter 2. All solvents used were of spectrophotometric grade.

3.3.2. *Preparation of the ternary nanoassemblies*

1·2·4. Choline-calix[4]arene **1** (0.5 mg/ml, 3×10^{-4} M) was dissolved in 10 mL of 10 mM PBS, pH 7.4, to give a clear colloidal solution. NO donor **2** (1.55×10^{-4} M) as a powder was added to the colloidal solution of **1** and the mixture was sonicated for 15 min, stirred for 48 h, at room temperature, and then filtered with 0.2 µm filter (GHP, Acrodisc) to remove the unentrapped compound **2**. The photosensitizer **4** (3×10^{-6} M) was dissolved in methanol and the solvent was slowly evaporated to form a thin film which was hydrated with the **1·2** colloidal solution. The mixture was sonicated for 15 min and stirred for 10 days at room temperature. The mixture was passed through a 0.2 µm GHP filter.

1·2·5. Choline-calix[4]arene **1** (1 mg/ml, 6×10^{-4} M) was dissolved in 10 mL of 10 mM PBS, pH 7.4 and photosensitizer **5** (1.55×10^{-5} mL) was added. The mixture was stirred for 15 days at room temperature and then filtered with

0.2 µm filter (GHP, Acrodisc) to remove unentrapped drug. To the **1•5** colloidal solution, NO donor **2** (9×10^{-4} M) as a powder was added and the mixture was stirred for 10 days at room temperature. The mixture was passed through a 0.2 µm GHP filter.

After filtration the concentration of **1**, **4** and **5** was almost unchanged, whereas the amount of **2** underwent a reduction. The amount of entrapped **2** after filtration was determined spectrophotometrically at 396 nm (ε = 10.000 M^{-1} cm^{-1}) and encapsulation efficiency (EE %) and loading capacity (LC %) were calculated using the formulae below:

$$EE\,\% = (W_{IN}/W_i)\times100$$
$$LC\% = W_{IN} / (W_{IN} + W_{NP})\times100$$

where W_{IN} is the amount of drug in the nanoassembly, W_i is the total amount of drug added initially during preparation, and W_{NP} is the amount of calix[4]arene in the nanoassembly.

3.3.3. *Instrumentations*

UV/Vis absorption and fluorescence spectra were recorded on a Jasco V-560 spectrophotometer and Fluorolog-2 (Model, F-111) spectrofluorometer, respectively. $^1O_2$ emission was registered with the same spectrofluorimeter equipped with a NIR-sensitive liquid nitrogen cooled photomultiplier irradiating an air saturated sample. All measurements were performed in a thermostated quartz cell 1 cm path length, 3 mL capacity.

Size, polydispersity index and Zeta potential of the nanoassemblies were measured by Dynamic Light Scattering and Electrophoresis Light Scattering measurements, performed on a ZetaSizer NanoZS90 Malvern Instrument (UK), equipped with a 633 nm laser. (Scattering angle = 90°, T = 25 °C), and on Horiba LS 550 apparatus equipped with a diode laser with a wavelength of 650 nm. Hydrodynamic diameter of the aggregates was deduced through the Einstein-Stokes equation. Each measurement was performed three times.

NO release was measured with a World Precision Instrument, ISO–NO meter, equipped with a data acquisition system, and based on direct amperometric detection of NO with short response time (<5 s) and sensitivity range 1 nM–20 mM. The analogue signal was digitalized with a four-channel recording system and transferred to a computer. The sensor was accurately calibrated by mixing standard solutions of $NaNO_2$ with 0.1 M H_2SO_4 and 0.1 M KI according to following equation:

$$4H^+ + 2I^- + 2NO_2^- \rightarrow 2H_2O + 2NO + I_2$$

Irradiation was performed in a thermostated quartz cell (1cm path length, 3 mL capacity 25° C) by using a 200 mW continuum laser with λ_{exc} = 405 nm. NO measurements were carried out under stirring with the electrode positioned outside the light path in order to avoid NO signal artefacts due to photoelectric interference on the ISO–NO electrode.

3.3.4. Determination of fluorescence and $^1O_2$ quantum yields

Fluorescence quantum yields were determined by using optically matched solutions at the excitation wavelength of **1·2·4** or **1·2·5** solution and a solution of 3,3′,3′′,3′′′-(2,3-dihydroporphyrin-5,10,15,20-tetrayl) phenol in MeOH as a standard (Φ_f = 0.095)[58] through the following equation:

$$\Phi_f = \Phi_{f\,(s)}\,(In^2/I_{(s)}n^2_{(s)})$$

where $\Phi_{f(s)}$ is the fluorescence quantum yield of the standard; I and $I_{(s)}$ are the areas of the fluorescence spectra of the compounds and the standard, respectively; n and $n_{(s)}$ are the refraction index of the solvents used for the compounds and the standard. In any case the absorbance at the excitation wavelength were less than 0.1.

$^1O_2$ quantum yields were determined by using optically matched solutions at the excitation wavelength of **1·2·4** and **1·2·5** solution and a solution of 3,3′,3′′,3′′′-(2,3-dihydroporphyrin-5,10,15,20-tetrayl) phenol in MeOH as a standard (Φ_Δ =0.43).[55] The values of Φ_Δ were determined by using the following equation:[61]

$$\Phi_\Delta = \Phi_{\Delta\,(s)}\,(In^2k_{r(s)}/I_{(s)}n^2_{(s)}k_r)$$

Where $\Phi_{\Delta\,(s)}$ is the $^1O_2$ quantum yield of the standard, I and $I_{(s)}$ are the areas of the fluorescence spectra of the compounds and the standard, respectively; k_r and $k_{r(s)}$ the $O_2\,(^1\Delta_g)$ radiative rate in the solvents used[31] for compound and standard; n and $n_{(s)}$ are the refraction index of the solvents used for the compounds and the standard.

4. Photophysical and photochemical properties preservation of Iodurate Bodipies PSs in aqueous environment – Preliminary studies

4.1. Introduction

Boron-dipyrromethene (Bodipy) dyes, have received a considerable attention in the last decade as a new class of fluorescent dye molecules. These classes of fluorescent molecules exhibit a small Stokes shift, high fluorescence quantum yields, sharp excitation-emission peaks and good photochemical stability. Due to their unique photophysical, optical properties and synthetic versatility Bodipy dyes represent an interesting new class of PSs for PDT applications.

Herein we report the entrapment of two water unsoluble Bodipy, compounds **12** and **13**, in the polycationic calixarene **1** nanoassembly with a different encapsulation method, respect to **4** and **5**, and the study of the photophysical and photochemical properties in aqueous environment for their use as PSs.

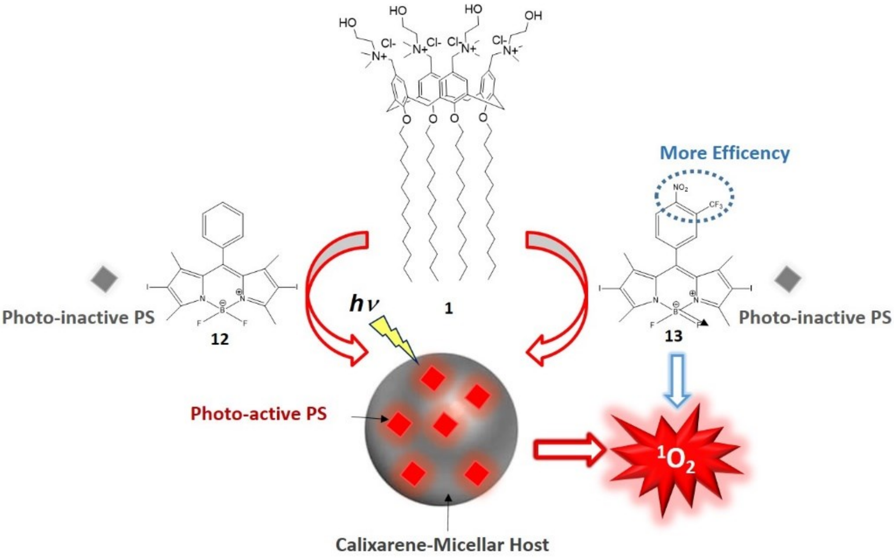

Fig. 35 Schematic representation of the photoresponsive nanosystems obtained.

4.2. Results and discussion

4.2.1. Characteristics of the components

Compounds **12** and **13** (Fig. 36) were synthesized in the research groups of Professors Gasco and Fruttero, Department of Sciences and Technology, University of Turin.

The two Bodipy were designed in order to be able to release singlet oxygen under irradiation with opportune wavelength. The presence of Iodine in the structure causes a significant bathochromic shift of absorption maxima in crc 30 nm respect to not Iodinate analogues. Moreover, the heavy atom increases the singlet to triplet transition and is hence valuable in the synthesis and design of PSs. In compound **13** the presence of two electronegative groups gives to this PS the capability to be more stable and efficient under irradiation respect to the analogous **12**.

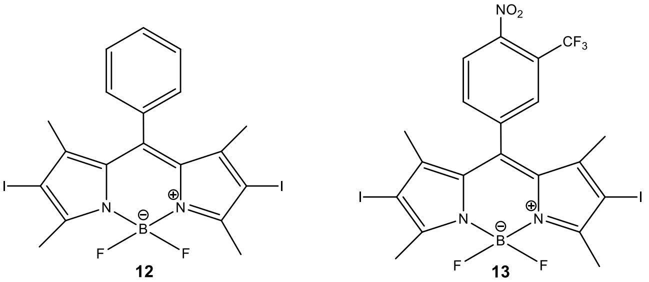

Fig. 36 Structure of compounds **12** and **13.**

4.2.2. Spectroscopic and dimensional characterization of the nanoassemblies **1·12** *and* **1·13**

In Fig. 37A are reported absorption spectra of compound **12** and **13** in CH_3CN, which show a profile characterized by an intense peak centered at 528 nm and 538 nm, respectively. We have found the same profile in calixarene nanoassembly for both PSs but the two peaks reported in Fig. 37B show a red shift of 10 and 15 nanometers, respectively. By the calculation of EE (%) before and after filtration was found an $\mathrm{EE}(\%)_{\mathrm{before}}$= 75% *ca.* for both nanoassemblies **1·12** and **1·13**. After filtration was found a little difference, $\mathrm{EE}(\%)_{\mathbf{1\cdot 12}\ \mathrm{after}}$ = 67% and $\mathrm{EE}(\%)_{\mathbf{1\cdot 13}\ \mathrm{after}}$ = 61%.

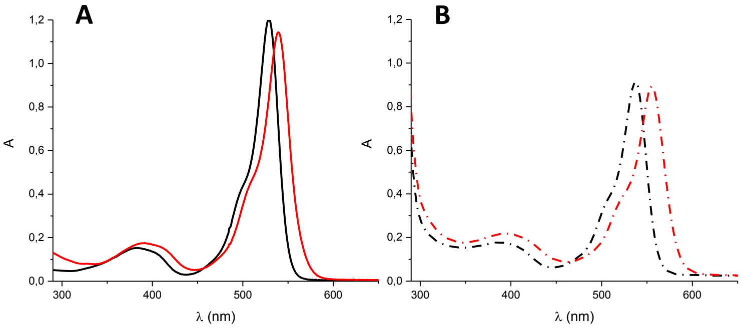

Fig. 37 Absorption spectra of **12** (black line) and **13** (red line) in CH_3CN (A) and in phosphate buffered saline (pH 7.4, 10 mM) in the presence of **1** (900 µM) (B).

DLS measurements (Fig. 38) indicate a size distributions centered between 140÷150 nm for both nanoassemblies **1·12** and **1·13** with a PDI ~ 0.45. Filtration at 0.2 µm does not influence to much the hydrodynamic diameters which result of *ca.* 110 nm with a PDI of 0.3.

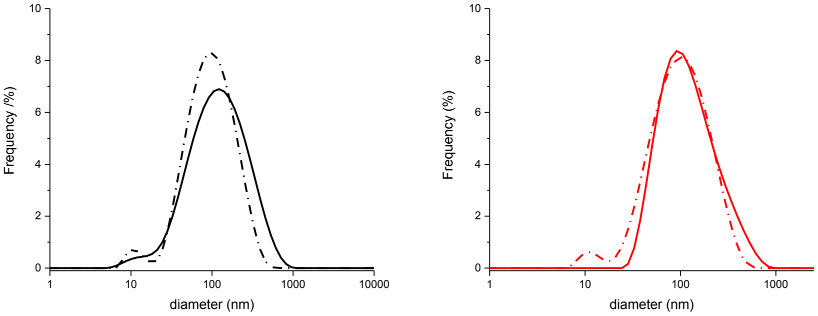

Fig. 38 Intensity weighted hydrodynamic diameter distributions of **1·12** (on the left) and **1·13** (on the right) before (continuous line) and after (dashed line) filtration at 0.2 µm obtained by DLS.

4.2.3. *Photobleaching*

In order to study the photostability of the two compounds **12** and **13** firstly we would investigate their behaviour in organic solvent. In Fig. 39 are reported absorption spectral changes observed upon 532 nm light irradiation – 100 mW of optically matched solutions of **12** and **13** in CH_3CN at regular irradiation intervals of 5 minutes. The comparison of the two maximum absorbance trends (Fig. 40) shows that compound **13** is more stable than **12** as clearly also confirmed in the maximum absorbance evolutions.

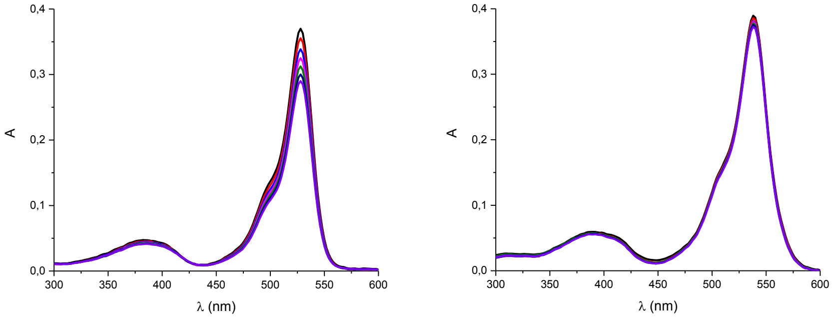

Fig. 39 Absorption spectral changes observed upon 532 nm light irradiation of of **12** (on the left) and **13** (on the right) in CH_3CN at regular irradiation intervals of 5 min.

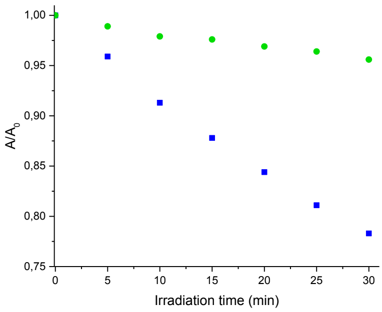

Fig. 40 Maximum absorbance evolutions observed upon 532 nm light irradiation of of **2** (blue squares) and **3** (green dots) in CH_3CN at regular irradiation intervals of 5 min followed at 528 nm and 538 nm respectively.

In a second moment we have investigated the behaviour of the two compounds in the calixarene nanoassemblies at the same irradiation conditions (Fig. 41). Also in this case looking at Fig. 42 was observed that compound **12** is less stable under irradiation than **13**, but furthermore it was observed that both maximum absorbance evolutions decrease much faster in aqueous environment than in CH_3CN.

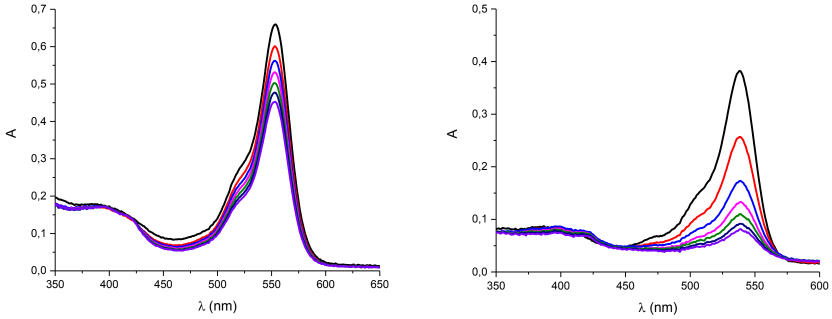

Fig. 41 Absorption spectral changes observed upon 532 nm light irradiation of an aqueous solution of the nanoconstruct **1·12** (on the left) and **1·13** (on the right) at regular irradiation intervals of 5 min.

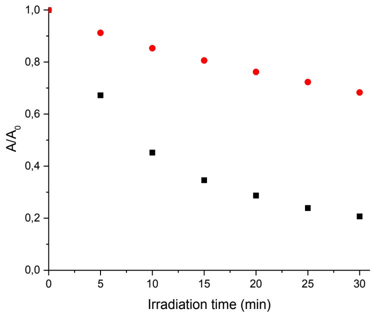

Fig. 42 Maximum absorbance evolutions observed upon 532 nm light irradiation of **1·12** (black squares) and **1·13** (red dots) at regular irradiation intervals of 5 min followed at 538 nm and 553 nm respectively.

4.2.4. $^1O_2$ Photogeneration from the nanoassemblies **1·12** *and* **1·13**

The generation of singlet oxygen, $^1O_2$, was detected by time resolving near infrared luminescence with sub-microsecond time resolution. We have examined the singlet oxygen produced by energy transfer from PSs to molecular O_2, in totally deuterated buffer solution of **12** and **13** in calix **1** respect to compound **12** in CH_3CN. The typical phosphorescence signal at 1270 nm[54] was observed for all samples investigated as showed in Fig. 43. The quantum yield of $^1O_2$ (ϕ_Δ) for **12** and **13** in calixarene nanoassemblies is 0.34 and 0.19 respectively.

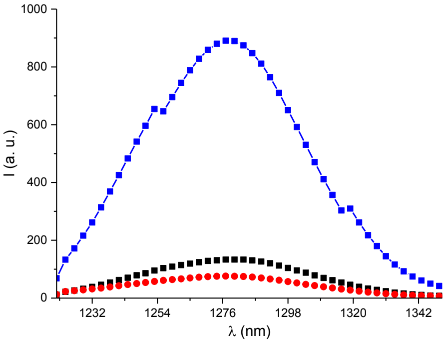

Fig. 43 $^1O_2$ luminescence detected upon excitation of the nanoassemblies **1·12** (black squares) and **1·13** (red dots) λ_{ex} = 532 nm (b) in deuterated phosphate buffered saline (pH 7.4, 10 mM). The $^1O_2$ luminescence spectrum observed for **12** in CH_3CN is also shown, for sake of clarity (blue squares).

4.2.5. Relative Efficency (E_{rel}) of the two PSs

On the basis of the previous experiments we would investigate the Relative Efficiency (**E_{rel}**) of the two PSs through the following equation:

$$\mathbf{E_{rel} = \phi_\Delta \cdot \tau}$$

Where **ϕ_Δ** is the singlet oxygen quantum yield and **τ** is the lifetime. On the basis of the values reported below compound **13** seems to be a better PS in terms of photostability and efficiency although it has a lower singlet oxygen quantum yield than **12** in the calixarene nanoassembly. These results suggest that the presence of electronegative groups on the ring protects the bodipy structure from the photodegradation process making compound **13** a better PS for treatments of longer duration.

Compound	**ϕ_Δ**	**τ**	**$E_{rel\ (normalized)}$**
12 in CH_3CN	0.79	57.84	14.19
12 in calix **1**	0.34	9.46	1
13 in calix **1**	0.19	28.75	1.69

Table 1. Values of ϕ_Δ, τ and E_{rel} obtained for **12** in CH3CN, **12** and **13** within **1**.

4.3. Experimental section

4.3.1. *Preparation of the nanoassemblies*

For the preparation of both nanoassemblies **1·12** and **1·13**, compounds **12** and **13** were firstly dissolved in CH_3CN (1.35 x10^{-5} M) and slowly evaporated to form thin films. After compound **1** was added as solid (4.5 mg) and then the mixture was dissolved in 1 ml of EtOH, were all compounds are soluble, and sonicated for 10 minutes. Under vigorous agitation, an aqueous solution (3 ml PBS 10 mM pH=7.4 +7 ml of water) was quickly added and the mixture was stirred for 15-20 minutes at room temperature. Afterwards solvent was removed under reduced pressure (30°C) up to a final volume of 3 ml ([**1**] = 1.5 mg/ml – 900 µM/ [**12**] and [**13**] = 1.1x10^{-5} M). The samples have been filtered with 0.2 µm GHP filter to remove any unentrapped compound **12** and/or **13**. The amount of **12** and **13** entrapped in the nanoassembly of **1**, before and after filtration, was determined spectrophotometrically at 538 and 553 nm respectively (ε = 89000 M^{-1} cm^{-1}).

Encapsulation efficiency (EE %) was calculated using the formula below:

$$EE\ \% = (W_{IN}/W_i) \times 100$$

where W_{IN} is the amount of drug in the nanoassembly, W_i is the total amount of drug added initially during preparation.

4.3.2. *Instrumentations*

UV-Vis absorption spectra were recorded with a JascoV-560 spectrophotometer in air equilibrated solutions, using either quartz cells with a path length of 1 cm. $^1O_2$ emission was registered with Spex Fluorolog-2 (mod. F-111) spectrofluorimeter equipped with a NIR-sensitive liquid nitrogen cooled photomultiplier, exciting the air-equilibrated samples of the nanoassemblies **1·12** and **1·13** at 532 nm with the fluorimeter lamp and 532 nm with a 100 mW continuum laser.

DLS measurements were performed with a ZetaSizer NanoZS90 Malvern Instrument (UK), equipped with a 633 nm laser (scattering angle = 90°, T =25 °C).

4.3.3. Determination of the $^1O_2$ quantum yields

$^1O_2$ quantum yields were determined by using optically matched solution at the excitation wavelength of the nanoassemblies and the standard. Compound **12** in CH_3CN ($\phi_\Delta = 0.79$)[62] was used as a standard. The values of ϕ_Δ for the nanoassemblies were determined by using the following equation:[61]

$$\phi_\Delta = \phi_{\Delta\,(s)}\ (In^2 k_{r(s)}/I_{(s)} n^2_{(s)} k_r)$$

Where $\phi_{\Delta(s)}$ is the $^1O_2$ quantum yield of the standard, I and $I_{(s)}$ are the areas of the fluorescence spectra of the compounds and the standard, respectively; k_r and $k_{r(s)}$ the O_2 ($^1\Delta_g$) radiative rate in the solvents used for compound and standard; n and $n_{(s)}$ are the refraction index of the solvents used for the compounds and the standard.

5. Design, synthesis and antibacterial activity of a multivalent polycationic calix[4]arene-NO photodonor conjugate

5.1. Introduction

In the previous parts of this dissertation an amphiphilic calix[4]arene scaffold was able to give nano-sized aggregates, and it showed the capacity to be a versatile supramolecular host and acted as a nanocarrier of different types of photostimulable precursors. In this case we wanted to test the antibacterial activity of a nanoaggregate formed by molecular scaffold containing multiple units of a NO photodonor by covalent linkage. The attention has been focused on the achievement of a novel multivalent photoresponsive NO donor, obtained by grafting multiple units of nitric oxide photoprecursor onto the upper rim of a calix[4]arene backbone.

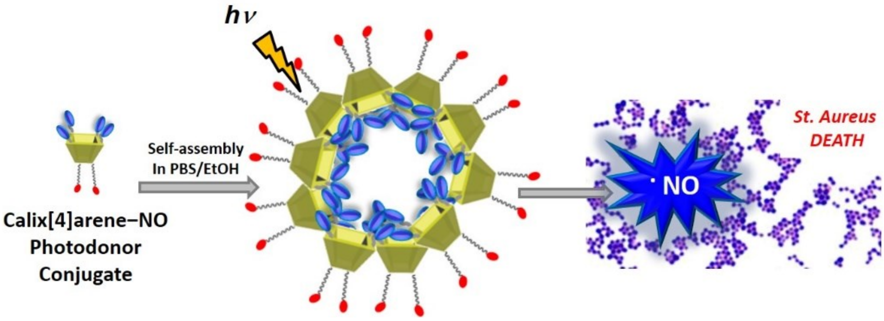

Fig.44 Schematic representation of the photoresponsive calixarene-based nanosystems.

5.2. Results and discussion

5.2.1. Synthesis of compound **17**

The NO-amphiphilic calix[4]arene **17** was synthetized by following the procedure depicted in Fig. 45. In particular, the *p*-chloromethyl-calix[4]arene (**14**), obtained by chloromethylation[63] of the commercial *p*-H-calix[4]arene, was treated with 3-(trifluoromethyl)-4-nitrobenzenamine to give compound **15**. To confer water-solubility to the calix[4]arene–NO donor conjugate, we introduced two quaternary ammonium groups at the calix[4]arene lower rim by passing through the intermediate compound **16** having two 3-bromopropyloxy pendants at the calix[4]arene lower rim in 1,3 distal position.

Finally, compound **16** was treated with N,N-dimethyl-ethanol amine to achieve calix[4]arene derivative **17**.

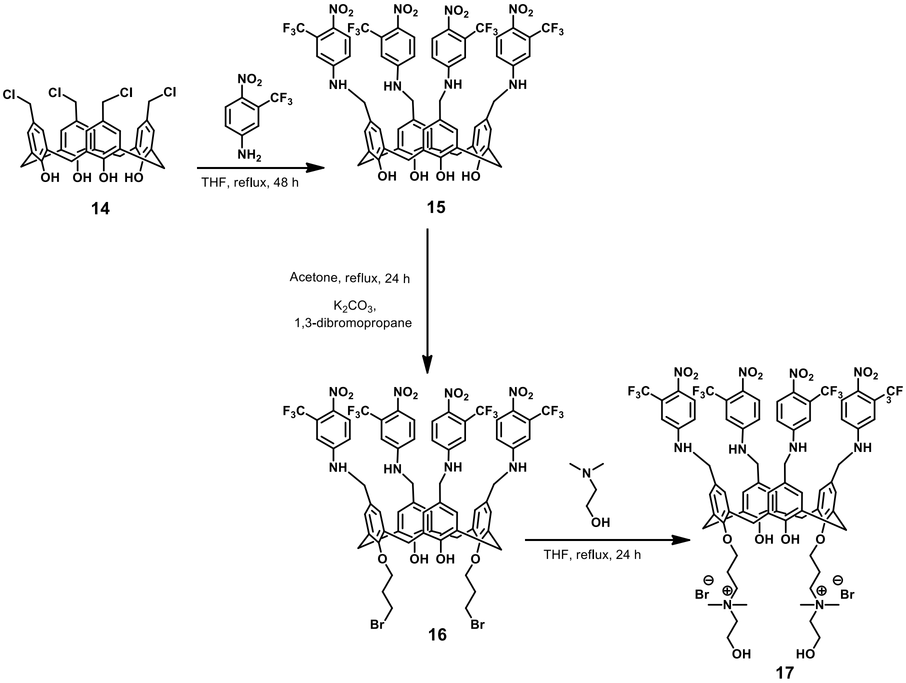

Fig. 45 Schematic representation of the synthetic steps involved in **17** obtaining.

5.2.2. Characteristics of **17**

Calix[4]arene **17** is characterized by the presence of four nitroaniline photoprecursor groups at the upper rim to confer to the calixarene scaffold the capability to release nitric oxide under light stimulation in a confined region of the space; and two choline groups, two quaternary ammonium salts, at the lower rim which give solubility in acqueous environment to the structure, ensure an amphiphilic behaviour and help to destibilize the cell membrane. Due to its structure this molecule has the capability to self-assembly in nano-sized systems.

5.2.3. Nanoassembly of **17***: spectroscopic and dimensional characterization*

The absorption spectrum of compound **17** in MeOH is characterized by the typical band with a maximum at ca. 400 nm of the nitroaniline[19] and an UV signal due to the calixarene scaffold. The molar absorbivity at 400 nm was 39,000 M^{-1} cm^{-1}, a value, about four-fold larger than that of the 3-(trifluoromethyl)-4-nitrobenzenamine in the same solvent. This shows that the presence of multiple units of nitroaniline in the same scaffold does not influence the spectrophotometrical properties of the chromophoric groups. Because of the important hydrophobic component in our scaffold, compound **17** is not totally soluble in water and in 10 mM PBS (pH 7.4), but it can be dissolved in a PBS/MeOH mixture (80:20) as demonstrated by UV-vis spectrum in Fig. 46A.

DLS measurements (Fig. 46B), show that **4** in PBS/MeOH mixture (80:20) forms nanoassemblies of 321.4 nm ± 43.2 with an average hydrodynamic diameter of 271 nm ± 18 (Z average) and PDI = 0.18 ± 0.02.

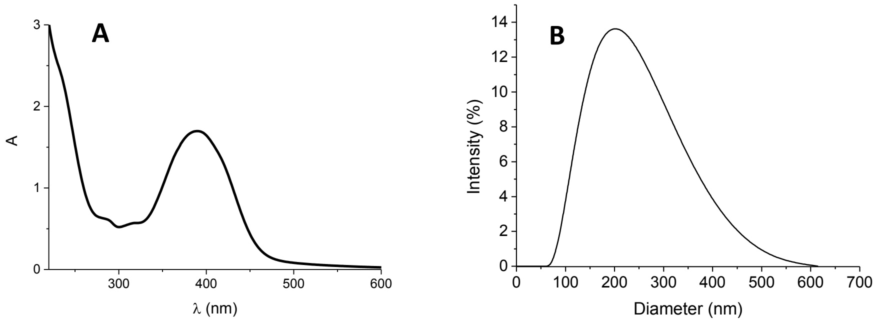

Fig. 46 (A) Absorption spectrum of **17** in PBS/MeOH (80:20). (B) Size distribution of the nanoassembly **17**.

5.2.4. NO photorelease from **17**

Irradiating with a 405 nm laser, NO release by the samples was monitored subjecting the photoactive component at regular intervals of light and darkness. The results illustrated in Fig. 47A provide evidence that a water/alcholic solution of **17** and a PBS aqueous solution of **3**, a water soluble model compound, are stable in dark and supply NO exclusively upon illumination with visible light. By comparison of the two NO release profiles is clear that the efficiency of NO photogeneration in the case of **17** is higher than that of the model compound **3**, even though they have the same absorbance at the excitation wavelength. This suggests an active role of the calixarene scaffold in the NO release process analogously to what found for not covalent entrapping nitric oxide photoprecursor approach.[64]

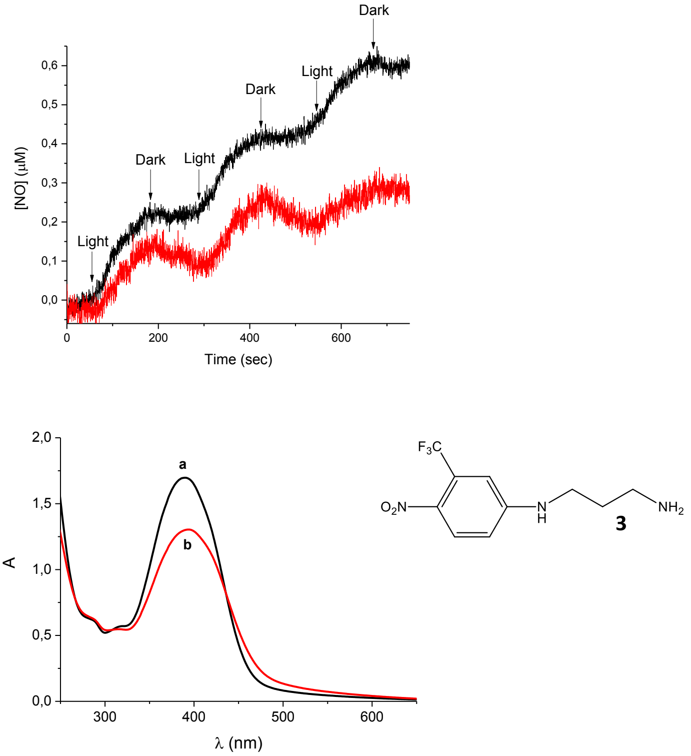

Fig. 47 (A) NO release profile observed for hydro-alcholic (PBS/MeOH 80:20) solution of **17** (black line) and an optically matched solution of the model compound MC **3** (red line) in PBS. (λ_{exc} = 405 nm). (B) Absorption spectra of compound **17** before (***a***) and after the NO photorelease experiment (***b***).

NO release issue of the solutions was further monitored by a photobleaching (Fig. 48). Solution of **17** was irradiated with a laser at 405 nm at regular intervals of 6 minutes. The absorbance profiles obtained show a clear reduction of the main signal relative to the formation of the phenol derivative as the only product obtained. From the spectra it is evident that after 36 minutes of irradiation the production of NO seems to be stopped even though the spectrophotometric signal of the nitroaniline is still clearly visible. This phenomenon may be due to non-twisted conformation of the nitroaniline groups covalently linked to the macrocyclic structure locked in a cone-conformation.

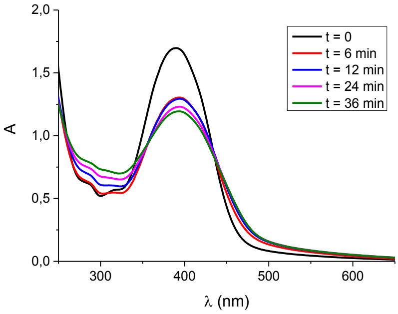

Fig. 48 Absorption spectral changes observed upon 405 nm light irradiation of for hydro-alcholic (PBS/MeOH 80:20) solution of **17** for regular irradiation intervals of 6 min.

5.2.5. Antibacterial activity of **17**

Antibacterial activity tests of **17** were performed by Dr A. R. Blanco (Alfa Intes ITS), Dr. A. Nostro and Dr. M. D' Arrigo (Department of Chemical, Biological, Pharmaceutical and Environmental Science, University of Messina). Two different bacterial strains were chosen, *Staphylococcus aureus* ATCC 6538 and *Escherichia coli* ATCC 10356, as Gram positive and Gram negative bacteria, respectively. The bacterial cultures were kept in the dark or irradiated at different times with a 450 W Xenon lamp equipped with a cut-off filter at 380 nm. Fig. 49B reports the time-inhibition curves obtained testing the antibacterial activity of **17** in dark and in light on *St. Aureus*. It is evident that the hydro-alcoholic solution (PBS:EtOH 10%) of **17** has shown a significant reduction in dark after 30 min (reduction of 98.9 % and 1.96-log in CFU/mL).

According to the data reported in literature it is known that ammonium quaternary salts are able to destabilize the cell membrane. The effect is increased under irradiaton. We observed in fact a significant antimicrobial activity after 10 min (reduction of 99.2 % and 2.1-log in CFU/mL) to reach a decrease in CFU/mL > 99.95 % (reduction > 3.31-log) after 20 minutes of irradiation.

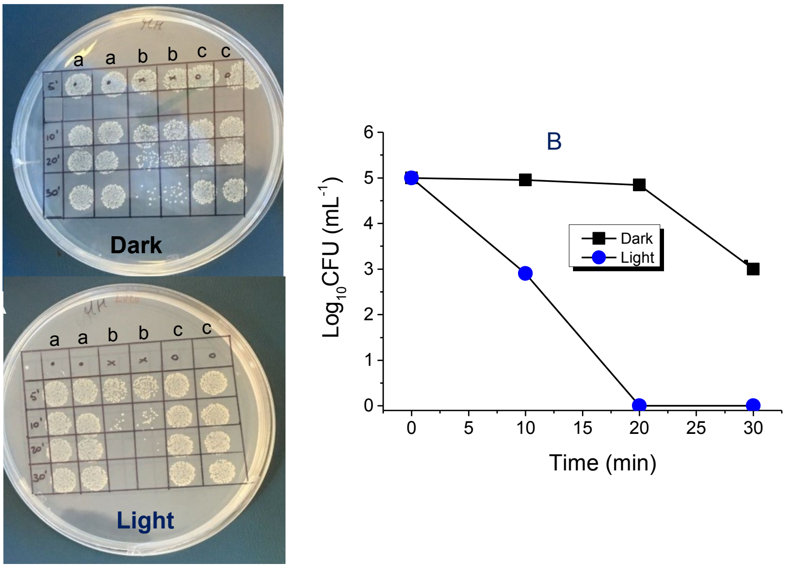

Fig. 49 (A) Representative images for the antibacterial effect of a solution of **17** on *S.aureus* in the dark and under illumination at different times. Samples in duplicate: (a) control in PBS; (b) compound **17** (0.25 mM, 5 % EtOH/PBS); (c) control in 5 % EtOH/PBS; (B) Time-inhibition curves of *S. aureus* growth treated with compound **17** in the dark and under visible light irradiation (λ_{exc} > 400 nm).

The antibacterial effect of **17** on *E. coli* did not show the same effect, in fact Gram negative resist better than Gram positive bacteria to quaternary ammonium salts[34] effects. In any case we observed an effective decrease of 93.5 % in CFU/mL (1.2-log reduction) after 30 min irradiation, visible in the diluition 1:10, as shown in Fig. 50.

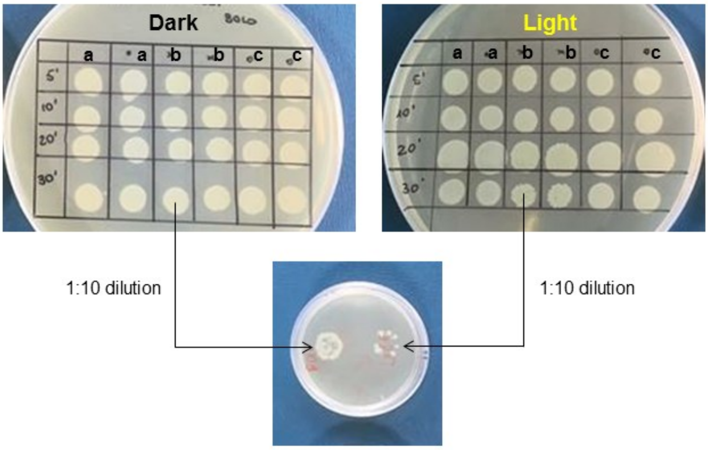

Fig. 50 Representative images for the antibacterial effect of a solution of compound **17** on E. coli in the dark and under illumination at different times. Samples in duplicate: (a) control in PBS; (b) compound **17** (0.25 mM, 5 % EtOH/PBS); (c) control in 5 % EtOH/PBS.

5.3. Experimental section

5.3.1. Materials

All reagents were of high commercial grade and were used without further purification. All solvents used were analytical grade.

Staphylococcus aureus ATCC 6538, *Escherichia coli* ATCC 10356 were purchased from LGC Standards.

5.3.2. Synthesis

Chloromethyl-calix[4]arene (14)

Chloromethyl derivative was synthesized according to the procedure reported in *J. Am. Chem. Soc.*, **2003**, 125, 15140.

4-Nitro-3-(trifluoromethyl)aniline-N-methyl-calix[4]arene (15)

To compound **14** (500 mg, 0.8 mmol) dissolved in THF (40 mL), 3-(trifluoromethyl)-4-nitrobenzenamine (83.3 mg, 3.6 mmol) was added. The reaction mixture was refluxed for 48 h, then the solvent was removed *in vacuo* and the solid was purified by chromatographic column (eluent: dichloromethane to 1% acetone/dichloromethane gradient) to give compound **15** (419 mg, 0.32 mmol) in 40 % yield. ^{1}H-NMR (400.13 MHz, Acetone-d_6): δ 3.64 (br signal, $ArCH_2Ar$), 4.25 (d, 8 H, *J* = 5.2 Hz, 4 ×$ArCH_2N$), 6.84 (dd, 4 H, *J* = 2.4 Hz, *J* = 9.2 Hz, 4 × aniline ArH), 6.90 (br t, 4 H, 4 × NH), 7.13 (d, 4 H, *J* = 2.0 Hz, 4 × aniline ArH), 7.28 (s, 8 H, 8 × calixarene ArH), 7.99 (d, 4 H, *J* = 9.2 Hz, 4 × aniline ArH), 9.98 (br s, 4H, 4 × OH). ^{13}C-NMR (100.64 MHz, Acetone-d_6): δ 30.9, 46.3, 111.3, 112.4, 116.9, 122.0, 124.7, 128.4, 128.8, 129.0, 130.6, 135.5, 148.9, 152.6. ESI-MS: m/z calcd for $C_{60}H_{44}F_{12}N_8O_{12}$ $[M-H]^-$ 1295.3; found 1295.2.

4-Nitro-3-(trifluoromethyl)aniline-N-methyl-calix[4]arene-O-propyl bromide (16). To compound **15** (250 mg, 0.19 mmol) dissolved in acetone (7 mL), K_2CO_3 (66.3 mg, 0.48 mmol) and 1,3-dibromopropane (194 µL mg, 1.9 mmol) were added. The mixture was refluxed for 24 h, then the solvent was removed *in vacuo* and the solid was purified by preparative TLC (100 % dichloromethane) to give compound **16** (116 mg, 0.075 mmol) in 40 % yield. ^{1}H-NMR (400.13 MHz, $CDCl_3$): δ 2.55 (t, 4 H, *J* = 5.6 Hz, 2 × $OCH_2\mathit{CH_2}CH_2Br$), 3.40 and 4.29 (AX system, 8 H, *J* = 13.2 Hz, 4 ×$ArCH_2Ar$), 3.98 (t, 4 H, *J* = 6.4 Hz, 2 × OCH_2), 4.05-4.20 (overlapped, 12 H, 4 × $ArCH_2N$ and 2 × CH_2Br), 4.88 (t, 2 H, *J* = 4.3 Hz, 2 × NH), 5.05 (t, 2 H, *J* = 5.0 Hz, 2 × NH), 6.02 (dd, 2 H, *J* = 9.2 Hz, *J* = 2.4 Hz, 2 × ArH), 6.59 (dd, 2 H, *J* = 9.5 Hz, *J* = 2.0 Hz, 2 × ArH), 6.73 (d, 2 H, *J* = 2.0 Hz, 2 × ArH), 6.87 (s, 4 H, 4 × calixarene ArH), 6.88 (d, *J* = 2.0 Hz, 2 × ArH), 6.97 (s, 4 H, 4 × calixarene ArH), 7.51 (d, 2 H, *J* = 9.2 Hz, 2 × ArH), 7.94 (d, 2 H, *J* = 8.8 Hz, 2 × ArH), 8.08 (s, 2 H, 2 × OH). Elemental analysis: Calcd. for $C_{67}H_{58}Br_2F_{12}N_8O_{12}$: C, 51.75; H, 3.76; Br, 10.28; F, 14.66; N, 7.21%. Found: C, 51.61; H, 3.48; N, 7.20%.

4-Nitro-3-(trifluoromethyl)aniline-N-methyl-calix[4]arene-O-propyl-N-(dimethyl)-ethanol (17).

To compound **16** (107 mg, 0.07 mmol) dissolved in dry THF (8 mL), *N,N*-dimethyl-ethanolamine (31 µL, 0.3 mmol) was added. The mixture was stirred and refluxed for 24 h and the precipitate was recovered by centrifugation. After removal of the solvent, the solid was washed with THF by repeated centrifugation and removal of the solvent (three times), to give compound **17** (103 mg, 0.06 mmol) in 86 % yield. ^{1}H-NMR (400.13 MHz, MeOD): δ 2.49 (br m, 4 H, 2 × $OCH_2\mathit{CH_2}CH_2N$), 3.34 (overlapped methanol, 12 H, 4 × CH_3), 3.49 and 4.25 (AX system, 8 H, *J* = 13.2 Hz, 4 × $ArCH_2Ar$), 3.62 (br t, 4 H, 2 × $N\mathit{CH_2}CH_2OH$), 3.80 (br m, 4 H, 2 × $OCH_2CH_2\mathit{CH_2}N$), 4.05 (s, 4 H, 4 × $ArCH_2N$), 4.07 (br s, 4 H, 2 × CH_2OH), 4.13 (br t, 4 H, 2 × $O\mathit{CH_2}CH_2CH_2N$), 4.19 (s, 4 H, 4 × $ArCH_2N$), 6.12 (d, 2 H, *J* = 9.2 Hz, 2 × ArH), 6.71 (dd, 2 H, *J* = 9.6 Hz, *J* = 2.2 Hz, 2 × ArH), 6.88 (br s, 2 H, 2 × ArH), 6.92 (s, 4 H, 4 × calixarene ArH), 7.01 (br s, 2 H, 2 × ArH), 7.12 (s, 4 H, 4 × calixarene ArH), 7.62 (d, 2 H, *J* = 8.8 Hz, 2 × ArH), 7.90 (d, 2 H, *J* = 9.2 Hz, 2 × ArH). ^{13}C-NMR (100.64 MHz, MeOD): δ 24.6, 32.3, 47.2, 47.3, 52.6, 56.9, 63.5, 67.4, 74.3, 112.4, 112.9, 113.6, 122.5, 125.3, 126.8, 126.9, 127.3, 129.2, 129.3, 129.5, 130.0, 130.2, 134.7, 135.8, 136.3, 136.4, 152.3, 153.4, 154.1, 154.2. ESI-MS: m/z calcd for $C_{74}H_{76}F_{12}N_{10}O_{14}^{2+}$ 778.26 $[M]^{2+}$; found 778.2.

5.3.3. Preparation of the hydro-alcoholic solution of compound **17**

Compound **17** (500 mg) was solubilized in MeOH or EtOH (100 µL) and PBS (10 mM, pH 7.4) was added up to the reported concentrations and alcohol percentage.

5.3.4. Instrumentations

Spectra ^{1}H and ^{13}C NMR were recorded on a Bruker Avance 400.13 and 100.61 MHz, respectively.

ESI-MS spectra were recorded in MeOH/H_2O (80:20, v:v) on a Thermo Finnigan LCQ Classic Ion trap.

UV-Vis absorption spectra were recorded with a JascoV-560 spectrophotometer in air-equilibrated solutions, using either quartz cells with a path length of 1 cm.

Irradiation of the samples in solution was performed in a thermostated quartz cell (1 cm pathlength, 3 mL capacity) under gentle stirring, by using a continuum laser with λ_{exc} = 405 nm (ca. 100 mW) having a beam diameter of ca. 1.5 mm

DLS measurements of assembly of and zeta potential measurements of all systems were performed with a ZetaSizer NanoZS90 Malvern Instrument (UK), equipped with a 633 nm laser. (Scattering angle = 90°, T = 25 °C).

Antibacterial experiments were performed with 450 W Xenon Lamps equipped with a cut-off filter at *crc* 400 nm.

NO release for samples in solution was measured with a World Precision Instrument, ISO-NO meter, equipped with a data acquisition system, and based on direct amperometric detection of NO with short response time (< 5 s) and sensitivity range 1 nM – 20 µM. The analog signal was digitalized with a four-channel recording system and transferred to a PC. The sensor was accurately calibrated by mixing standard solutions of $NaNO_2$ with 0.1 M H_2SO_4 and 0.1 M KI according to the reaction:

$$4H^+ + 2I^- + 2NO_2^- \rightarrow 2H_2O + 2NO + I_2$$

Irradiation was performed in a thermostated quartz cell (1 cm pathlength, 3 mL capacity) using the above continuum laser with λ_{exc} = 405 nm. NO measurements were carried out under stirring with the electrode positioned outside the light path in order to avoid NO signal artefacts due to photoelectric interference on the ISO-NO electrode.

5.3.5. Antibacterial experiment

Pure cultures were inoculated in 10 mL Muller Hinton Broth and incubated (37 °C, 24 hrs) to allow complete growth in the liquid growth medium. The overnight broth culture was centrifuged at 4000 rpm for 15 minutes. Supernatant Muller Hinton Broth was discarded leaving bacterial pellet at the bottom of the centrifuge tube. PBS (5 mL) was added to the tube and the bacterial pellet was washed by shaking it gently. The washed pellet was again centrifuged at 4000 rpm for 15 minutes. The pellet thus formed was standardized to 2×10^5 CFU/mL by optical density measurements. For experiments, bacteria (50 µL) were inoculated in 96 well plate to yield a final inoculum of 1×10^5 CFU/mL. Then calix[4]arene derivative **17** (0.5 mM in 10 % EtOH/PBS) was added and the final concentration was equal to 0.25 mM in 5 % EtOH/PBS. Two different control samples were also prepared in PBS and 5 % EtOH/PBS. The titer of the inoculum was counted by decimal dilutions and 20 µL of each dilution was seeded in a ground plate of Mueller Hinton agar (time t0). Irradiation was performed with a 450 W Xenon lamp equipped with a cut-off filter at crc 400 nm. The light source was designed in such a way so as to fit over the 5 cm culture plate with a fixed distance of irradiation of 15 cm. At different time, 20 µL of each sample was taken and seeded in duplicate as a spot in a ground plate of Mueller Hinton agar. The viability count for each sample was done in duplicate plates. CFU counts were carried out after incubation at 37 °C for 24-48 h. The % of growth inhibition was calculated by the following equation:

$$\text{Growth inhibition \%} = [1 - (\text{CFU tx} / \text{CFU t0})]100$$

where t_x is CFU at different time x (x = 5, 10, 20, 30 min) and t_0 is CFU at time zero. The time kill plots were constructed.

Part II

Polymersomes-based nanoconstructs for anticancer and antibacterial photoactivated treatments

6. Design, synthesis, antitumoral and antibacterial activity of polymersomes containing a nitric oxide photoprecursor by covalent and non-covalent approach

6.1. Introduction

The second part of this PhD research project has been essentially done at Ulster University where I spent nine months in the group of Dr. Bridgeen Callan, under the supervision of Dr. Nino Marino for the synthetic strategies and antitumoral activity, while the antibacterial properties have been tested in collaboration with Prof. Ibrahim Banat. The activity has been focused on the achievement of amphiphilic copolymers, containing an opportune quantity of cholesterol in their structure. A series of polymersomes functionalized, by covalent and non-covalent approach, with a nitric oxide photoprecursor were obtained and their antitumoral and antimicrobial properties tested.

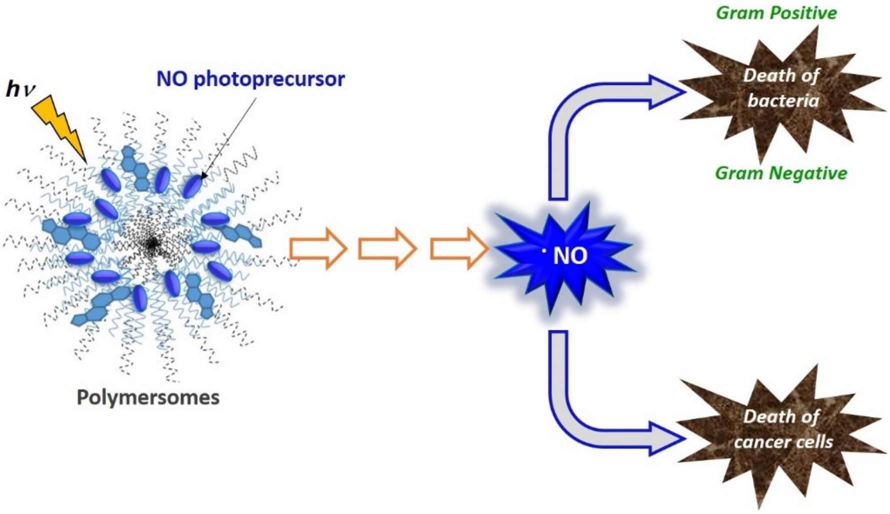

Fig. 51 Schematic representation of the polymersomes realized.

6.2. Results and discussion

6.2.1. Synthesis of polymers

In order to obtain polymersomes with specific characteristics of biocompatibility, ability to penetrate cell membrane and capability to entrap different kind of guests were synthetized different polymers having in their structure the same backbone. A schematic representation of the synthetic pathway followed is depicted in Fig 52. All hydrophobic (**19**,**20, 22** and **23**) and hydrophilic (**18** and **24**) monomers synthetized are methacrilyc acid derivatives to allow the polymerisation. The polyethylene glycol (PEG) methacrylate used has an average molecular weight of 500 Da.

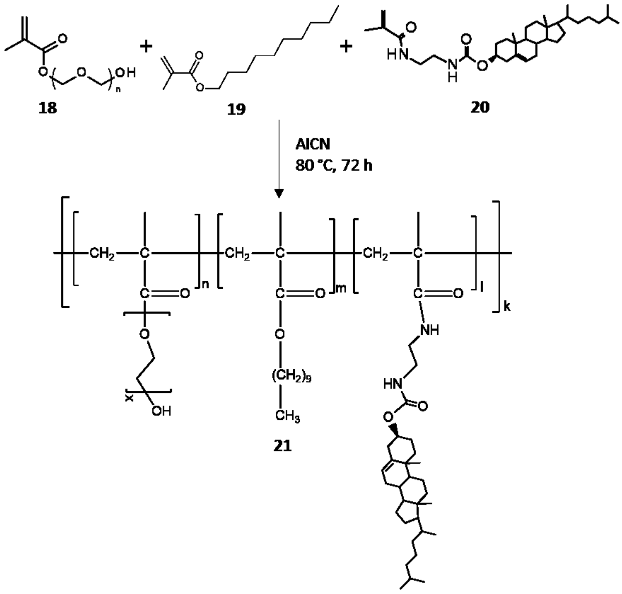

Fig. 52 Schematic representation of the synthetic steps involved in polymer **21** obtaining.

Components	MW	Molar Ratio	% (mol)
Methacrylic PEG	500	5	75
Colesteryl	540	0,75	9
Decyl	226	2.25	0.11
AICN	244	0,3	4,5

Table 2. MW, Molar Ratio and % (mol) values of the monomers used to obtain **21**.

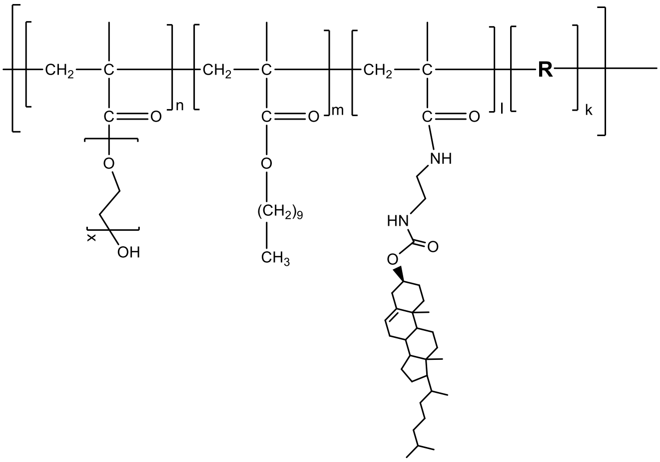

Fig. 53 General structure of the polymer to obtain polymers **25**,**26** and **27**.

R =

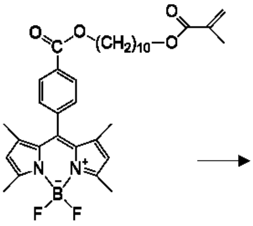

22

→ **25**

Components	MW	Molar Ratio	% (mol)
Methacrylic PEG	500	5	75
Colesteryl	540	0,75	9
Decyl	226	2.25	0.11
Bodipy	592	0.1	1
AICN	244	0,3	4,5

R =

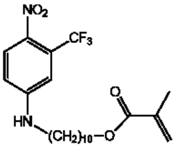

23

→ **26**

Components	MW	Molar Ratio	% (mol)
Methacrylic PEG	500	5	60,2
Colesteryl	540	0,75	9
Decyl	430	1,125	13,5
Bodipy	226	1,125	13,5
AICN	244	0,3	3,6

R =

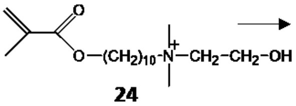

24

→ **27**

Components	MW	Molar Ratio	% (mol)
Methacrylic PEG	500	5	60,2
Colesteryl	540	0,75	9
Met Colina	314	2.5	23
Decyl	226	2.2	20
AICN	244	0,3	3,6

Fig. 54 Chemical Structures of substituents R = **22**, **23** and **24** used to obtain polymers **25**, **26** and **27** respectively (on the left). Tables showing MW, Molar Ratio and % (mol) values of the monomers used to obtain **25**, **26** and **27**.

6.2.2. Synthesis of compound **16**

Compound **28**, a 4-nitro-3-(trifluoromethyl)aniline derivative, contains a hexyl alkyl chain at the amino group useful to encourage the entrapping inside polymersomes **21** and **27** by hydrophobic interactions. The hydrophobic NO precursor **28** was synthetized starting from the commercial 4-Nitro-3-(trifluoromethyl)aniline treated with Hexyl iodide in CH_3CN (Fig. 55).

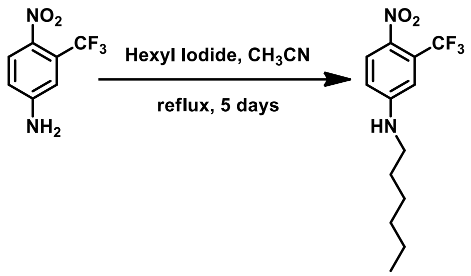

28

Fig. 55 Schematic representation of the synthetic route in **28** obtaining.

6.2.3. Characterization of polymersome **21**

All the polymers synthetized, due to their structure, are able to self-aggregates in 10 mM PBS solution, pH =7.4. In Fig. 56 are reported DLS measurements of **21** at two different concentrations, 5 (A) and 10 (B) mg/ml respectively. By the comparison of the two size distributions it is evident that there is not variation in term of dimensions, d = 100÷130 nm, and Poly Dispersity Index, PDI = 0.3÷0.4.

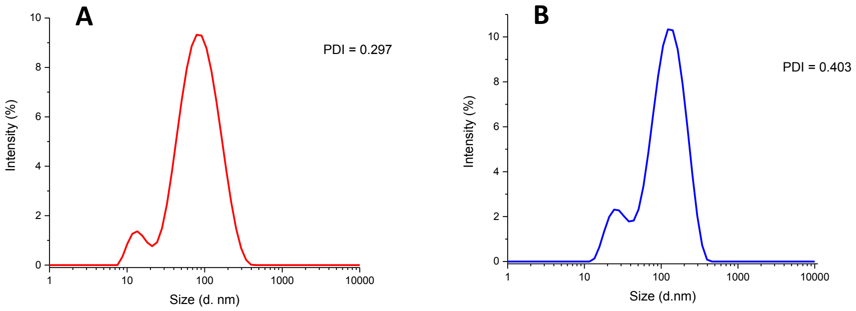

Fig. 56 Intensity weighted hydrodynamic diameter distributions of polymersomes of **21** at concentrations of 5 mg/ml (A), 10 mg/ml (B) obtained by DLS.

6.2.4. Nanoassembly **21·29***: spectroscopic and dimensional characterization*

In order to verify the cellular uptake of this system we decided to entrap inside polymersome **21** (5 mg/ml) a hydrophobic fluorescent label (**29**)[65] by non-covalent approach. In Fig. 57B is reported absorption spectrum of compound **29** (Fig. 57A) in chloroform which shows the typical profile characterized by an intense peak centered at *crc* 500 nm. Compound **29** is totally insoluble in phosphate-buffered aqueous solution, while it is soluble when entrapped in polymersome **21** as confirmed by overlapping spectra in Fig. 57B. The efficient encapsulation is also confirmed by the emission spectra acquired exciting at 480 nm (Fig. 57C). As demonstrated by the emission profile, **29** in **21**, shows a similar trend to that observed in chloroform, confirming the effective encapsulation of **29** within polymersome **21**.

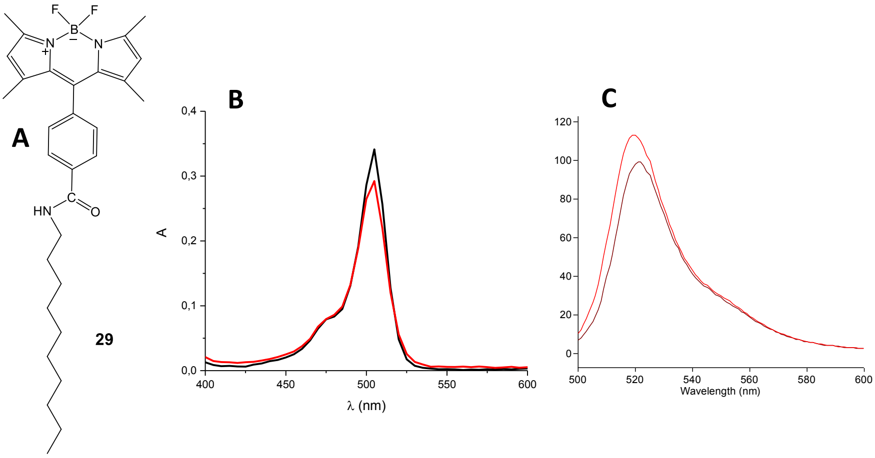

Fig. 57 (A) Structure of 29. (B) Absorption spectra of **29** (75 μM) in chloroform (black line) and in phosphate buffer (pH 7.4, 10 mM) in presence of **21** (5 mg/ml) (red line). (C) Fluorescence emission spectra of **29** in chloroform (black line) and in phosphate buffer (pH 7.4, 10 mM) in presence of **21** (5 mg/ml) (red line). – Spectra collected by samples diluted 20 times.

The dimensions of the system **21·29** are approximately the same observed for empty polymersome **21**. DLS measurements (Fig. 58) gave in fact a distribution centered around 110 nm with a PDI slightly higher than 0.4. Therefore, the presence of a hydrophobic guest inside the polymersome does not influence the properties of the host.

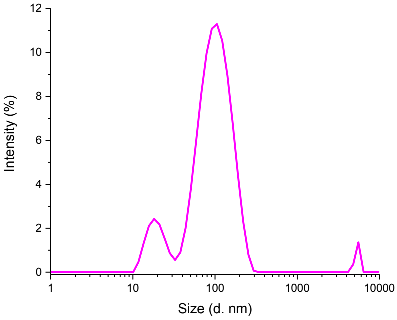

Fig. 58 Intensity weighted hydrodynamic diameter distributions of **21·29** nanoassembly.

6.2.5. *Cellular uptake of nanoassembly* **21·29** *on HeLa cells*

Cellular uptake was established in Hela cells by encapsulation of **29** into the hydrophobic bilayer of the polymersome **21**. Bodipy **29** was chosen because of its low solubility in water. HeLa cells were incubated with polymersome **21** empty and nanoassembly **21·29** for 24 h. Successfully the media was removed and the cells washed with PBS before being analysed for intracellular bodipy content. The results of this study are shown in Fig. 59.

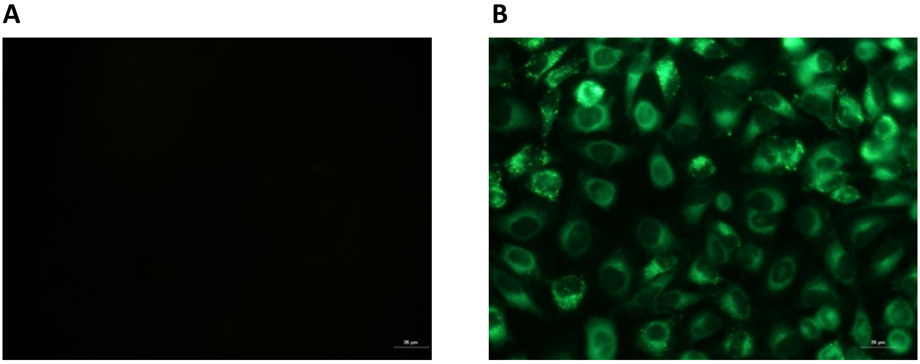

Fig. 59 Fluorescence microscopy images (λ_{ex} = 480 nm, scale bar = 25 µm, magnification = 40X) of HeLa cells recorded after incubation with (A) empty polymersome **21** and (B) nanoassembly **21·29**.

The evident fluorescence of HeLa cells in presence of nanoassembly **21·29** proves the presence of the bodipy within the cells. It is not possible to predict if this phenomenon is because of the presence of the nanoassembly or just by compound **29**. The structure of polymersome **21**, in fact approaching to the cells, could penetrate the cell membrane or allows the release of **29** into hydrophobic compartments.

6.2.6. Cellular uptake of polymersomes **25**

Polymer **25** (Fig. 60A) has the same structure of **21**. Although, it differs for the presence of a fluorescent tag **22** in the skeleton. Its capability to self-assembly in polymersomes is not influenced by the presence of **22** in the structure. Obtained polymersome **25**, in fact, as confirmed by DLS measurements (Fig. 60B) shows the same dimensional trend of **21** with a diameter of *crc* 110 nm and a PDI = 0.394. This polymer was synthetized in order to be sure that the nanocarrier is able to overcome the cell membrane and penetrate inside the cells.

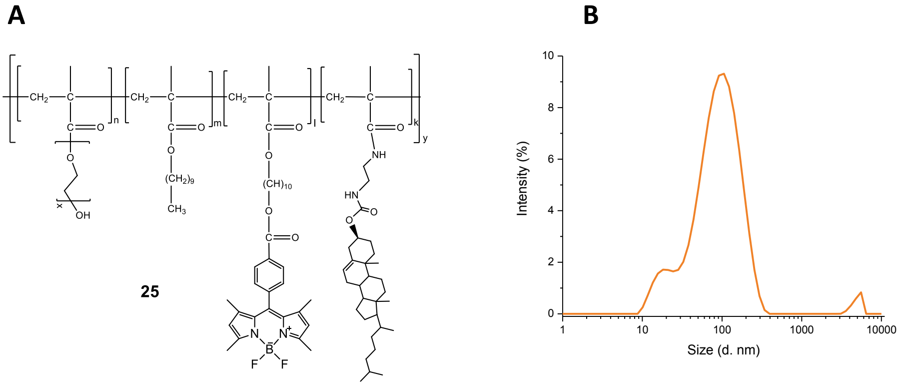

Fig. 60 (A) Structure of polymer **25**. (B) Intensity weighted hydrodynamic diameter distributions of **25.**

Fig. 61 reports images of HeLa cells acquired with microscopy fluorescence technique, after staining with DAPI. The green fluorescence of the bodipy was detected at 520 nm. Microscopy images show that the bodipy fluorescence is probably located in endosomial vescicles. In this case is possible to assert that there is a penetration of polymersome inside the cellular environment.

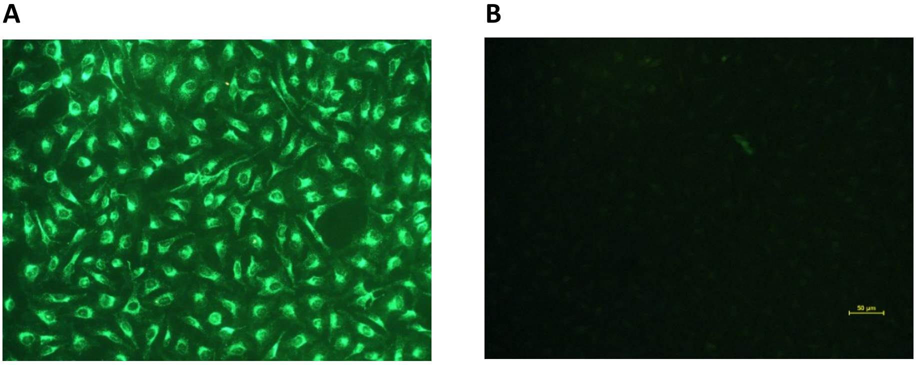

Fig. 61 HeLa cells, fluorescence microscopy images (λ_{ex} = 480 nm, scale bar = 50 µm, magnification = 20X) recorded after incubation with (A) and without (B) polymersome of **25**.

6.2.7. Nanoassembly **21·28***: spectroscopical and dimensional characterization*

The hydrophobic structure of compound **28** makes this molecule totally insoluble in aqueous environment. We used compound **21** as a suitable nanocarrier to introduce compound **28** in PBS aqueous solution obtaining a light yellow colloidal dispersion.

In order to verify the efficient encapsulation of **28** in **21** we have characterized the system by Uv-vis spectroscopy. The absorption spectrum of **28** entrapped in polymersome **21** shows the typical profile centered at *crc* 400 nm. which is the same observed for **28** in MeOH (Fig. 62). The amount of **28** loaded in **21** is *crc*. 800 µM, which correspond to an EE 100%.

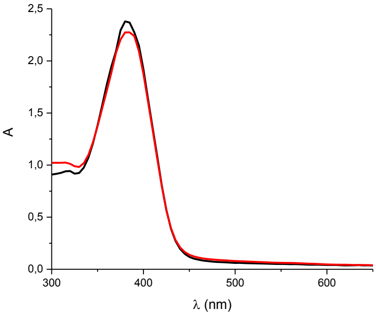

Fig. 62 Absorption spectra of **28** in methanol (black line) and in phosphate buffer (pH 7.4, 10 mM) in presence of **21** (5 mg/ml) (red line). – Spectra collected by samples diluted 5 times.

DLS measurements (Fig. 63) show that the dimensions of the nanoassembly **21·28** are approximately the same of the empty polymersome **21**, with a distribution centered around 130 nm and PDI = 0.3. As found for nanoassembly **21·29**, also in this case the results suggest that the arrangement of the aggregates is not altered by the loading of a hydrophobic guest.

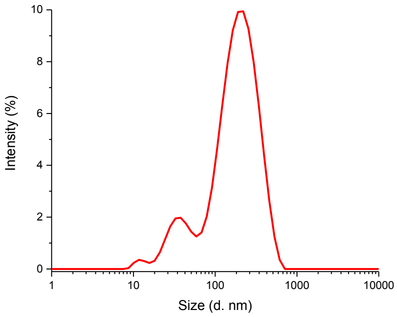

Fig. 63 Intensity weighted hydrodynamic diameter distributions of **21·28**.

6.2.8. Comparison of EE (%) between polymersomes and micelles obtained by polymer **21**

Polymersomes, respect to nanosized systems as micelles, are able to entrap hydrophobic and hydrophilic guests. In addition, due to their structure, which shows a hydrophobic bilayer region, polymerosomes can enpsulate higher amount of hydrophobic guests. Fig. 64 reports two bar graphs related to the EE (%) of polymersome respect to micelles obtained from **21** at the same concentration. It is evident that the EE (%) of micelles (Fig. 64A) decreases in the range between 0.075 and 0.1 mg of **28**, showing that micelles can encapsulate up to 0.075 mg of **28** with an EE= 100%. Polymersomes, instead, are able to load an amount of guest 5 times higher keeping an EE (%) = 100% (Fig. 64B).

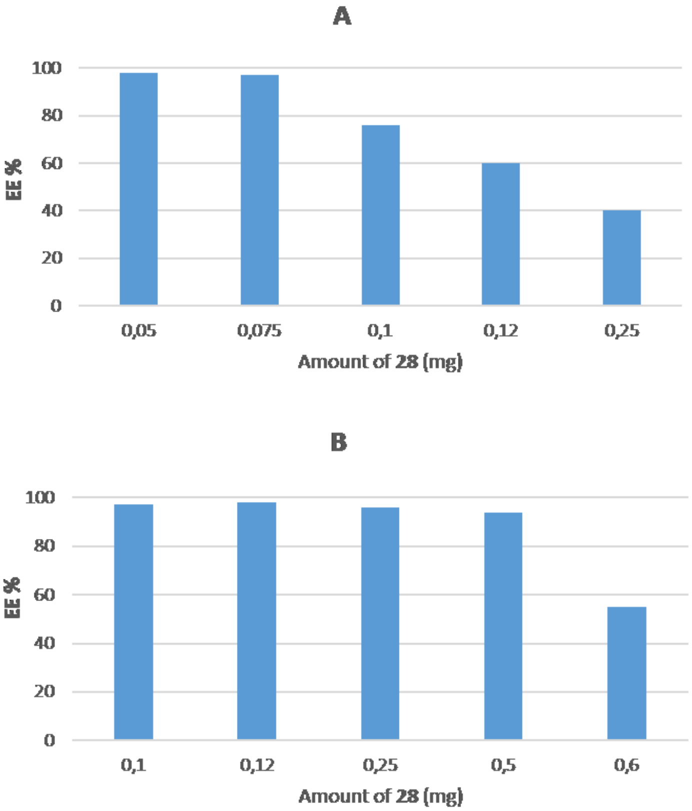

Fig. 64 EE% trend of micelles (A) and polymersomes (B) obtained from polymer **21** (1 mg/ml) *vs.* the amount of **28** (mg).

6.2.9. NO detection

NO photorelease from **21·28** was monitored by the direct detection by using an ultrasensitive NO electrode, alternating cycles of light/dark. Fig. 65A shows the NO release profile obtained from **21·28** compared with **21** empty as blank. Variations of absorption spectrum of **28** in **21** (Fig. 65B), collect irradiating with a laser at 405 nm, show a progressive bleaching of the main signal of nitroaniline, proving that there are not collateral or additional reactions which compete with the NO photorelease.

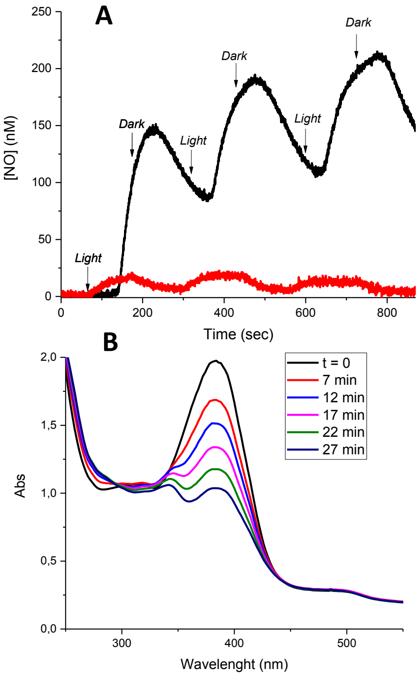

Fig. 65 (A) NO release profile observed for PBS solution of **21·28** (black line) and and **21** empty in PBS (red line). (λ_{exc} = 405 nm). (B) Absorption spectral changes observed upon 405 nm light irradiation of **21·28**.- Starting sample (t=0) diluted *crc* 5.5 times.

6.2.10. In vitro study: antitumoral activity of **21·28** *on cervical (HeLa) and pancreatic (BxPc3) cancer cells*

The antitumoral efficacy of **21·28** was tested on two different cancer cells line: Hela and BxPc3. The experiments were carried out in order to test the biocompatibility of **21** and the anticancer properties of **21·28** nanoassembly. After overnight incubation with **21** and **21·28**, cells were washed twice with PBS and irradiated for 40 minutes with UVP UVGL-58 lamps, operating at 365 nm – 6 Watt (0.4 mW cm^{-2}). As demonstrated by MTT assay results (Fig. 66), polymersome **21** has shown not only a good biocompatibility but also a non-toxicity towards HeLa cells, in fact, a higher number of cells was found in presence of **21**. The exposure to light of cells treated with nanoassembly **21·28** led a cell viability percentage less than 5%, while in dark, as expected, there was no mortality.

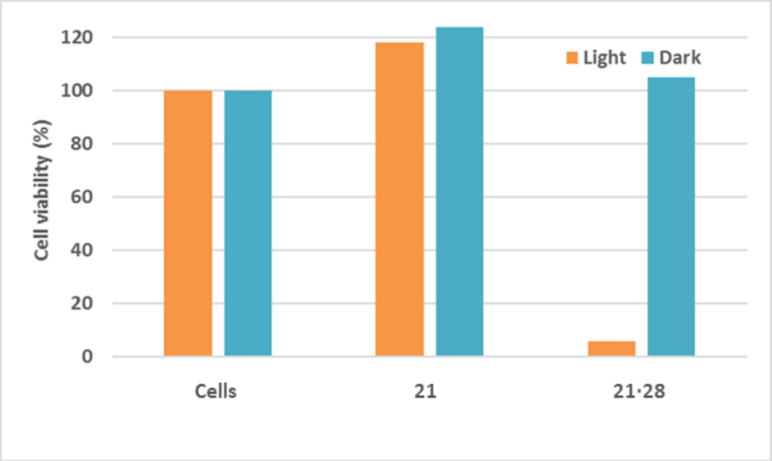

Fig. 66 HeLa cells MTT assay treated with **21·28** nanoassembly.

Fig. 67 reports the results of MTT assay on BxPc3. It is known that pancreatic cancer cells are among the worst tumoral cells lines due to their drug resistance characteristics and high propensity for metastasis. Indeed, their behavior towards nanoassembly **21·28** proved to be more resistant than HeLa cells. In this case was not observed a further growth of the cells in presence of **21**, however the activity of nitric oxide released by **21·28** under irradiation led a remarkable reduction of the cell viability.

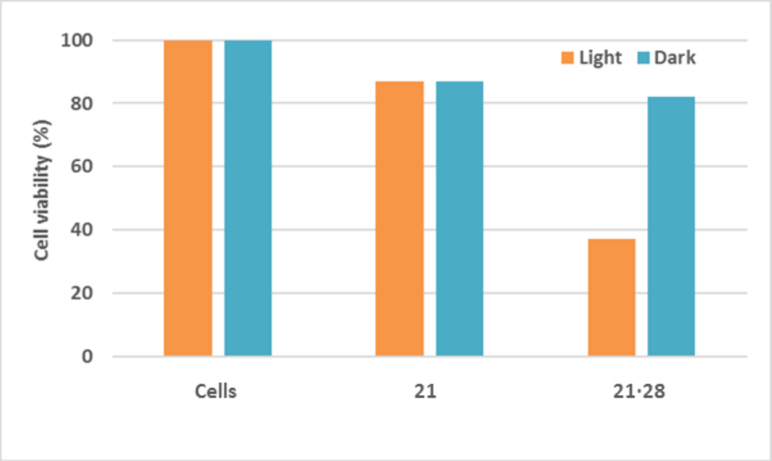

Fig. 67 BxPc3 cells MTT assay treated with **21·28** nanoassembly.

6.2.11. Characterization of polymersome **26**

Polymer **26** (Fig. 68A) was synthetized to study the behaviour of a polymersome containing in its structure a nitric oxide photoprecursor covalently linked. The amount of nitroaniline in the polymer structure is 13.5%. Spectroscopic characterization (Fig. 68B) has shown a profile containing a signal in the UV region relative to the backbone of all the other polymers studied and the presence of the typical band of nitroaniline in the visible region.

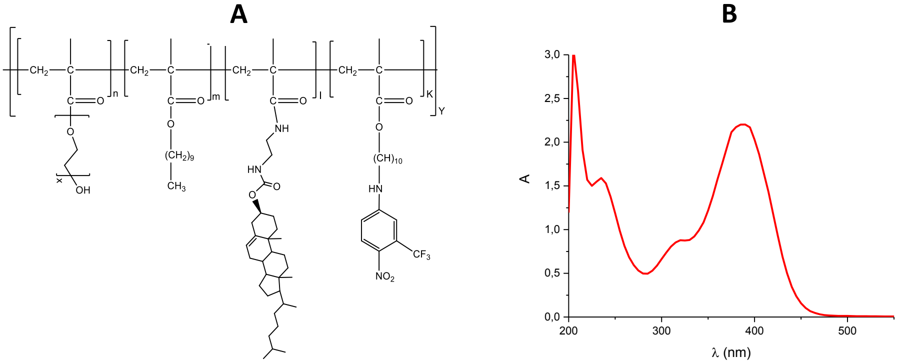

Fig. 68 (A) Structure of polymer **26**. (B) Uv-vis spectrum of polymersome **26** – spectrum collected by a sample diluted 4.35 times.

DLS measurements (Fig. 69) gave a size distribution with two families: the bigger one centered around 190-200 nm, and a smaller one around at 10 nm with a ratio *crc* 60:40. In this case PDI value is 0.693, higher than in the previous cases.

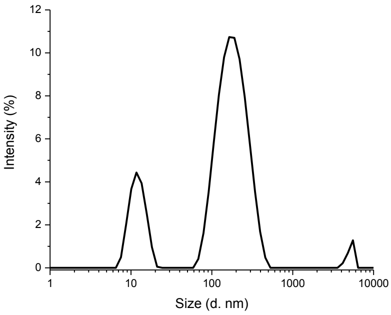

Fig. 69 Intensity weighted hydrodynamic diameter distributions of **26**.

6.2.12. NO release by photobleaching monitoring of polymersome **26**

The NO release from **26** was followed irradiating polymersome **26** with two UVP UVGL-58 lamps monitoring variations of the absorption spectrum at different times. As clearly shown in Fig. 70 the behaviour of polymer **26** is totally different than nanoassembly **21·28**. In this case, in fact, there is not only a hypochromic effect, but also a bathochromic shift. This effect might be due to collateral reactions competitive with the NO photorelease.

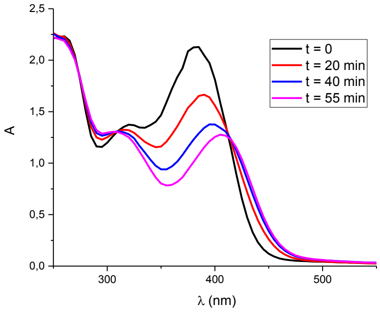

Fig. 70 Absorption spectral changes observed upon 365 nm light irradiation of **26**. Starting sample (t=0) diluted *crc* 4.35 times.

6.2.13. In vitro study: antitumoral activity of polymersome **26** on HeLa cells

Even though the anomalous behaviour observed during the photobleaching, a MTT assay was conducted on HeLa cells to see if there was in any case an antitumoral effect of **26**. Results shown in Fig. 71 suggest that there is not effect under light irradiation as well as in dark, confirming the failure release of nitric oxide as cytotoxic species.

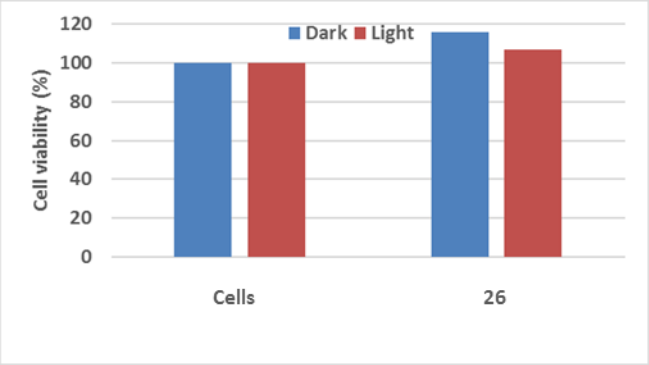

Fig. 71 Hela cells MTT assay treated with polymersome **26**.

6.2.14. Polymer **27**

It is known in literature that quaternary ammonium salts because of the cationic charge are able to destabilize the cell membrane of the bacteria. In order to study the different activity of nitric oxide conveyed by neutral and charged polymersome on different bacterial strains it was synthetized polymer **27** (Fig. 72A). Polymer **27**, as well as **21**, contains PEG, decyl alchil chain and cholesterol, but also a choline derivative group to confer a positive charge. DLS measurements of polymersome **27** (Fig. 72B), obtained at the same concentration of **21**, gave a Z-average of 130 nm, but a distribution composed of two families: 10 nm and 170 nm with a ratio 58:42. Poly Dispersity index is 0.218 and zeta potential ζ = +30 mV.

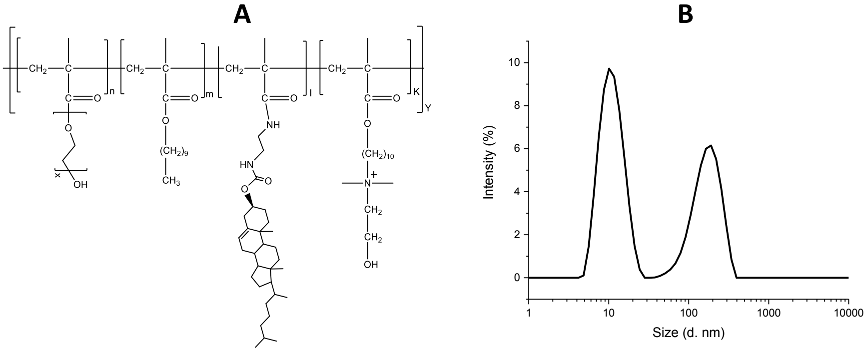

Fig. 72 (A) Structure of polymer **27**. (B) Intensity weighted hydrodynamic diameter distributions of **27.**

*6.2.15. Nanoassembly **27·28**: spectroscopical and dimensional characterization*

Compound **28** was encapsulated inside polymersome **27** in the same condition followed to obtain nanoassembly **21·28**. As demonstrated by the overlapping absorption spectra of **27·28** and **21·28** (Fig. 73), the capability of **27** to entrap **28** are the same of polymersome **21**, at the same concentrations.

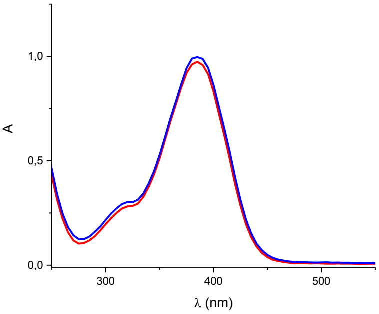

Fig. 73 Absorption spectra of **28** in phosphate buffer (pH 7.4, 10 mM) in the presence of **21** (5 mg/ml) (red line) and in the presence of **27** (5 mg/ml) (blue line) – Spectra collected by samples diluited 10 times.

DLS measurements (Fig. 74) gave a hydrodynamic a Z-average of 102 nm and, as for the polymersome empty, we found two peaks respectively centered at 11 nm and 120 nm with a ratio of 56:44. PolyDispersity Index (PDI) is 0.172 and a zeta potential ζ = +30 mV. The collected results suggest that also in this case entrapping of **28** does not influence the assembly of **27**.

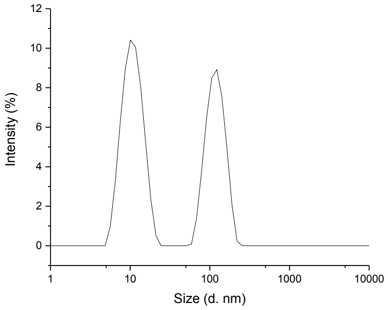

Fig. 74 Intensity weighted hydrodynamic diameter distributions of **27**.

6.2.16. Antibacterial activity of nanoassemblies **21·28** *and* **27·28**

The antimicrobial tests were performed at Ulster University in collaboration with Microbial Biotechnology group, direct by Prof. Ibrahim Banat, with the support of Mr. Victor Iro. Antibacterial properties of polymersomes, **21** and **27** empty, and entrapping nitric oxide photoprecursor, nanoassemblies **21·28** and **27·28**, were tested on four different bacterial strains. To have a broad spectrum of action two Gram Positive and two Gram Negative bacterial strains were choosen:

- *Staphylococcus aureus* (MRSA) ATCC 43300 (G+)
- *Staphylococcus epidermidis* DSM 28319 (G+)
- *Escherichia coli* ATCC 25922 (G-)
- *Pseudomonas aeruginosa* PA01(G-)

The bacterial cultures were kept in the dark or irradiated at different times with a 150 W Xenon lamp equipped with a cut-off filter at crc 400 nm. Fig. 75, 76, 77 and 78 report Time-kill curves in dark (A) and under irradiation (B) of the nanoassemblies **21·28** (blue), **27·28** (green) and, for comparison, **21** (red) and **27** (pink) alone, observed for *Staphylococcus aureus* (MRSA) ATCC 43300, *Staphylococcus epidermidis* DSM 28319, *Escherichia coli* ATCC 25922 and *Pseudomonas aeruginosa* PA01 respectively. In all experiments is reported a control in PBS (black) and during any experiment were collected pictures of the plates in dark and in light.

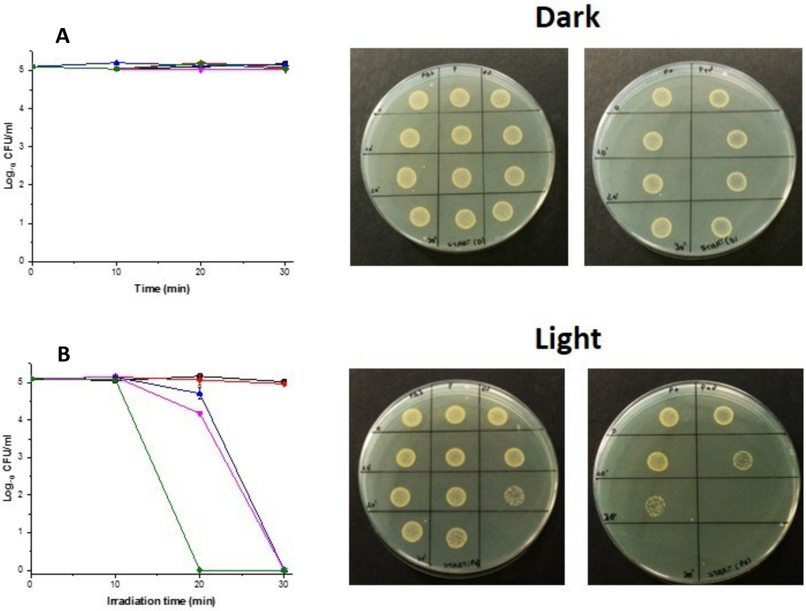

Fig. 75 Time-kill curves in dark (A) and under irradiation (B) of **21·28** (blue), **27·28** (green), **21** (red) and **27** (pink) alone, and in PBS (black) as control, observed for *Staphylococcus aureus* (MRSA) ATCC 43300.

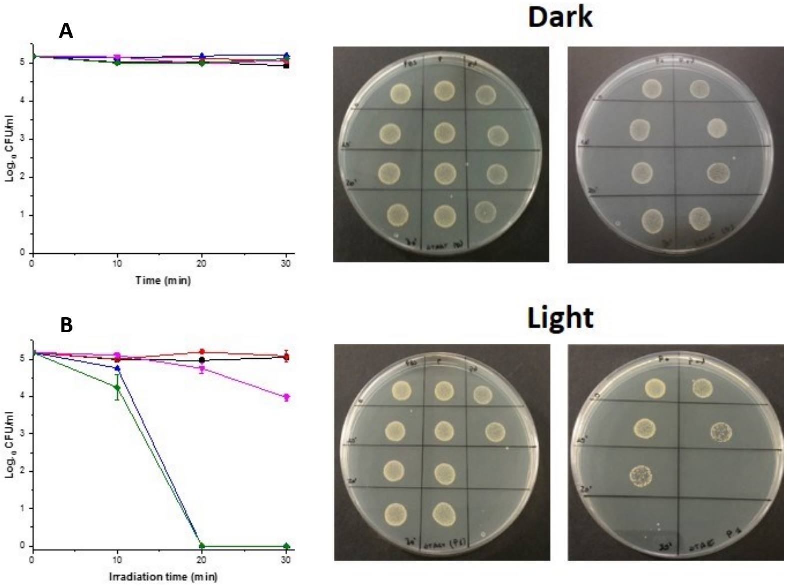

Fig. 76 Time-kill curves in dark (A) and under irradiation (B) of **21·28** (blue), **27·28** (green), **21** (red) and **27** (pink) alone, and in PBS (black) as control, observed for *Staphylococcus epidermidis* DSM 28319.

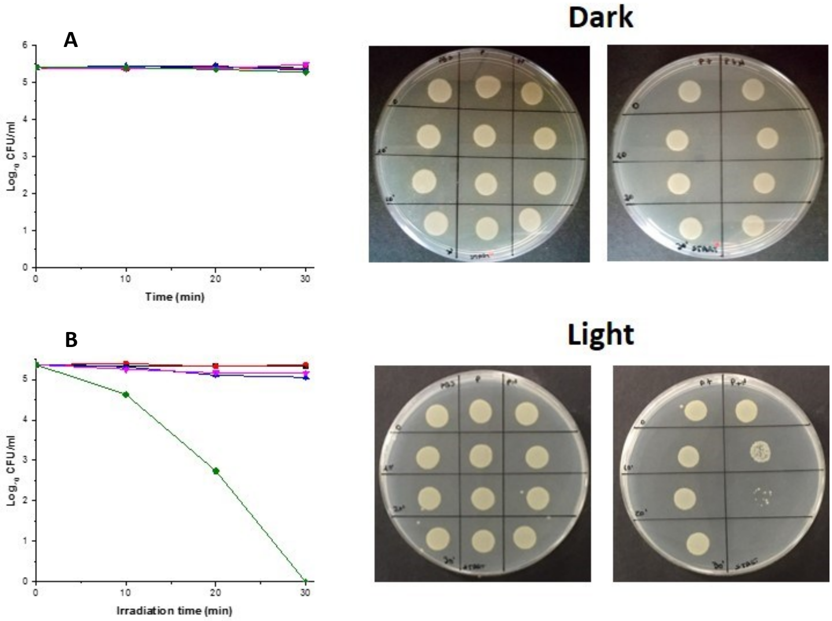

Fig. 77 Time-kill curves in dark (A) and under irradiation (B) of **21·28** (blue), **27·28** (green), **21** (red) and **27** (pink) alone, and in PBS (black) as control, observed for *Escherichia coli* ATCC 25922.

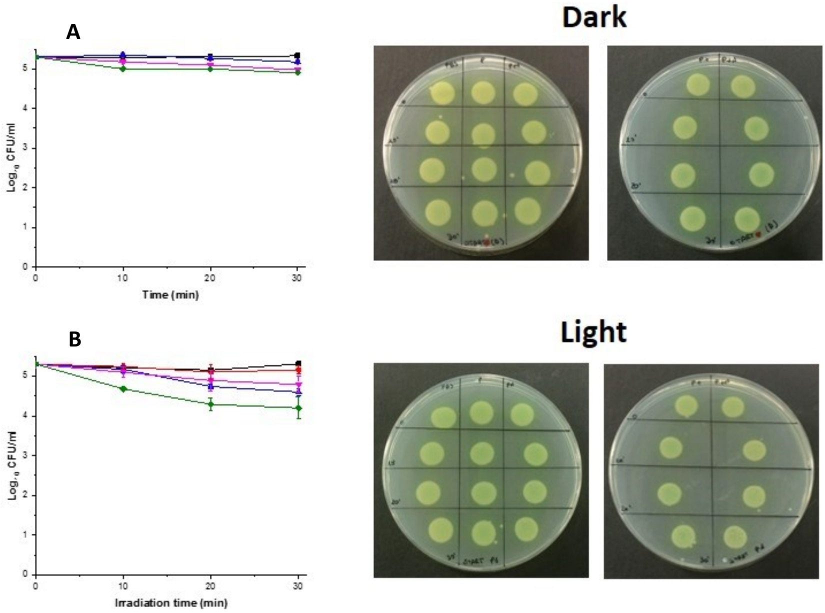

Fig. 78 Time-kill curves in dark (A) and under irradiation (B) of **21·28** (blue), **27·28** (green), **21** (red) and **27** (pink) alone, and in PBS (black) as control, observed for *Pseudomonas aeruginosa* PA01.

As shown in Fig.75 on *Staphylococcus aureus* (MRSA) ATCC 43300 there is not effect in dark (Fig. 75A), while under irradiation (Fig. 75B) there is a reduction of 0.4-log for **21·28** and 1-log *crc* for **27** after 20 minutes of irradiation, which gave total mortality after 30 minutes under light. There is, instead, a synergistic/additive effect, due to the combination of positive charge and NO, for **27·28** which led a total mortality after 20 minutes of irradiation. *Staphylococcus epidermidis* DSM 28319 no effect was observed in dark as well (Fig. 76A), while there is a reduction of 1-log because of the effect of **27** after 30 minutes. For both polymersomes, **21** and **27**, containing **28** there is a total mortality after 20 minutes of irradiation, though the slope for nanoassembly **27·28** is steeper than for **21·28** (Fig. 76B). Gram Positive bacterial strains were both highly sensitive to the effect **27·28**, while a different behaviour was observed for Gram Negative strains. *Escherichia coli* ATCC 25922 (Fig. 77B), in fact, showed to be sensitive to the presence of **27·28** under irradiation which is able to kill totally the strain after 30 minutes of treatment. A little effect was observed for both **27** and **21·28**, which have shown a similar effect. Totally different results were found for *Pseudomonas aeruginosa* PA01 although it is a gram negative as well as *E. coli*. It is known that PA01 is one of the strongest and resistant Gram Negative bacterial strains, responsible for a large number of infections hard to treat. Results reported in Fig. 78B shown a slight effect in dark, while under light was observed a reduction of 0.5-log, 0.7-log, and 1.1-log for **27**, **21·28** and **27·28** respectively, after 30 minutes of irradiation. The effect of **27**, **21·28** and **27·28** on PA01 can be better appreciated watching a picture of a diluition 1:10 reported in Fig. 79.

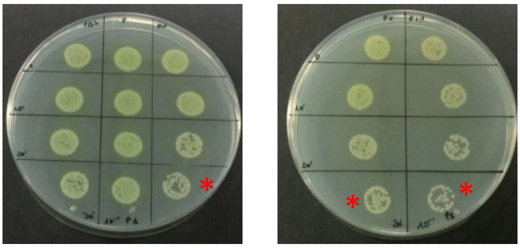

Fig. 79 Representative image of *Pseudomonas aeruginosa* PA01 under irradiation treated with **21**, **27**, **21·28**, **27·28** and in PBS as control by a diluition 1:10.

The different behaviour of PA01 respect to *E. coli* might be due to the production of rhamnolipids by *Ps. aeruginosa* species. Furthermore, it is known that among all *Pseudomonas*, PA01 is the largest producer of rhamnolipids. Rhamnolipids (RLs) are bacterial surfactants belonging to the glycolipid class, as they contain at least one sugar moiety (in this case rhamnose). A mixture of the four most common rhamnolipid representatives, RL1 to RL4 (Fig. 80), are produced by the bacterium *Pseudomonas aeruginosa* and released into the growth medium. A highly productive strain is a classified risk 2 pathogen, which means that the bacteria can cause human/animal disease.

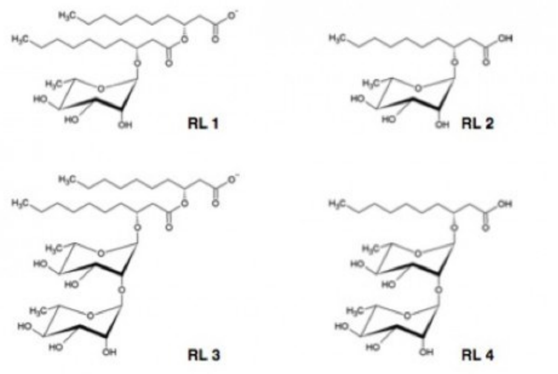

Fig. 80 Structures of most common rhamnolipids.

Biosurfactants can fulfill various physiological roles and provide different advantages to their producing strains:

- increase the surface area of water-insoluble substrates by emulsification,
- increase the bioavailability of hydrophobic substrates,
- bind heavy metals,
- be involved in pathogenesis,
- possess antimicrobial activity,
- regulate the attachment/detachment of microorganisms to and from surfaces.

In order to confirm the hypothesis that the different PA01 bearing was due to the production of rhamnolipids, an additional experiment was carried out. It was compared again the activity of all polymersomes on *E. Coli* in presence and in absence of rhamnolipids. Before to start the treatment under light, a solution of rhamnolipids (containing approximately 40% R1 and 60% R2) was added (to obtain a final concentration of rhamnolipds *crc* 1 g/l) to the bacterial solution and stirred for few minutes. The results are showed in Fig. 81. As expected, in presence and in absence of rhamnolipids the effects are totally different. In fact, in presence of rhamnolipids was observed just a slight reduction of 0.3-log and 0.5-log for **21·28** and **27·28** respectively, after 30 minutes of irradiation. It is evident that the bactericidal effect is essentially due to the nitric oxide photorelease, as observed for PA01. The capability as quaternary ammonium salts of polymersome **27** is inhibited by rhamnolipids, which having a pka 4.3÷5.5, at pH 7.4 they are in dissociated form, neutralizing the positive charge of polymersome.

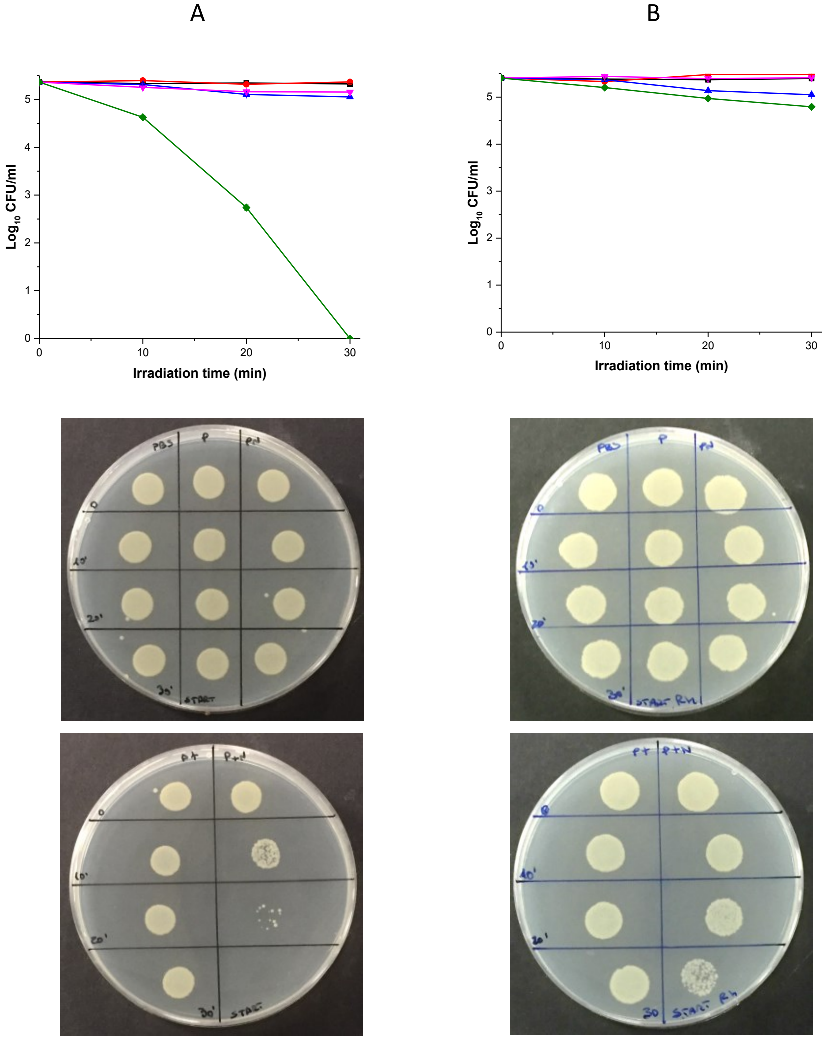

Fig. 81 Time-kill curves in absence (A) and in presence (B) of rhamnolipids for *Escherichia coli* ATCC 25922 treated with **21·28** (blue), **27·28** (green), **21** (red) and **27** (pink) alone, and in PBS (black) as control, under light irradiation.

6.3. Experimental section

6.3.1. Synthesis

Compound **30** was synthetized according to the procedure reported in *Int. J. Pharm.*, **2016**, 511,570.[38]

Compound **29** and **31** were synthetized according to the procedure reported in *J. Control. Rel.,* **2017** , 264, 136.[47]

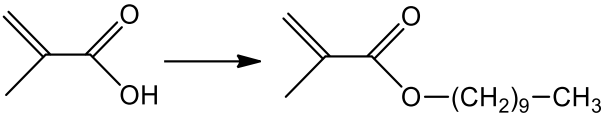

19

Decyl methacrylate (19)

Monomer **19** was synthesised starting from 250 mg of methacrylic acid (2.9 mmol), wich were added to 5 ml of 1-decanol and sulfuric acid in catalytic amounts. The solution was stirred for 48 h at room temperature. After reaction the mixture was purified by silica gel chromatography eluting with Exane/EtOAc, gradient from 100% Exane to 95:5 to give compound **19** in quantitative yield. ^{1}H NMR (CDCl$_3$, 500 MHz): δ = 6.10 (s, 1H), 5.57 (s, 1H), 4.14 (t, *J* = 7.0 Hz, 2H), 1.95 (s, 3H), 1.68 (t, *J* = 7.0 Hz, 2H), 1.26 (m, 14H), 0.88 (t, *J* = 7.0 Hz, 3H) ppm. ^{13}C NMR (CDCl$_3$, 125 MHz): *δ* = 167.6, 136.5, 125.2, 64.8, 31.9, 29.5, 29.5, 29.3, 29.2, 28.6, 25.9, 22.7, 18.3, 14.6 ppm.

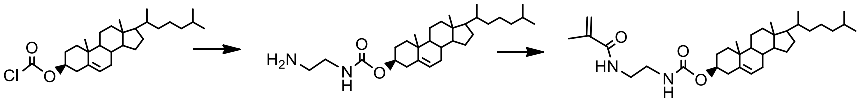

30 **20**

(*3S*)-10,13-dimethyl-17-(6-methylheptan-2-yl) 2,3,4,7,8,9,10,11,12,13,14,15,16,17-tetradecahydro-1*H*-cyclopenta[α]phenanthren-3-yl(2 methacrylamidoethyl)carbamate (20)

A mixture of **30** (500 mg, 1.05 mmol), methacrylic acid (109 mg, 1.26 mmol), EDC (405 mg, 2.11 mmol), and DMAP (25 mg, 0.21 mmol) was dissolved in 20 mL of CH$_2$Cl$_2$. After stirring at rt for 1 h, the solvent was removed under vacuum. The obtained crude product was purified by column chromatography (EtOAc/hexane 2:1) to give 550 mg of **20** as a white powder (yield, 96.4%).^{1}H NMR (CDCl$_3$, 500 MHz): δ = 6.59 (s, 1H), 5.73 (s, 1H), 5.36 (s, 1H), 5.00 (s, 1H), 4.48 (s, 1H), 3.43 (s, 2H), 3.36 (s, 2H), 2.29 (m, 2H), 1.96 (m, 2H), 1.84 (m, 2H), 1.55-0.65 (m, 41H) ppm. ^{13}C NMR (CDCl$_3$, 125 MHz): *δ* =

157.4, 139.7, 139.5, 122.5, 120.6, 74.7, 56.6, 56.1, 49.9, 42.3, 41.2, 40.4, 39.7, 39.5, 38.5, 36.9, 36.5, 36.1, 35.7, 31.9, 31.8, 28.2, 28.09, 28.02, 28.02, 24.2, 23.8, 22.8, 22.5, 21.0, 19.3, 18.7, 18.6, 11.8 ppm.

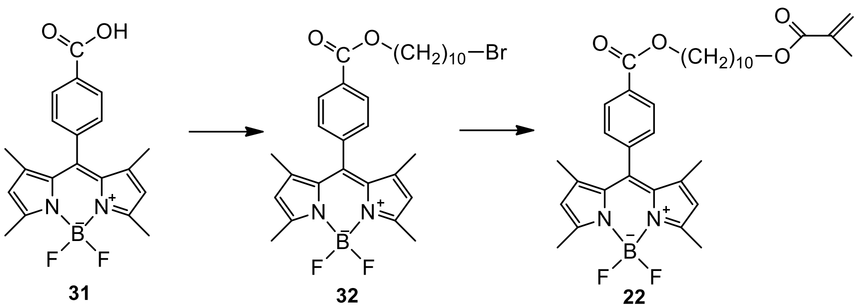

10-(4-(((10-bromodecyl)oxy)carbonyl)phenyl)-5,5-difluoro-1,3,7,9-tetramethyl-5*H*-dipyrrolo[1,2-*c*:2´,1´-*f*][1,3,2]diazaborinin-4-ium-5-uide (32)

Compound **31** (100 mg, 0.27 mmol), K_2CO_3 (74 mg, 0.53 mmol), and KI (88 mg, 0.53 mmol) were suspended in CH_3CN. The suspension was stirred at 50 °C for 1 hour, then 1,10-dibromodecane (400 mg, 1.3 mmol) was added to the suspension. After 24 h the mixture was cooled, the solvent was removed under vacuum condition and the crude product was extracted with EtOAc. The residue was purified by silica gel column chromatography (hexane/EtOAc 6:1 – 5:1) to give compound **32** as red oil (152 mg, 95% yield). ^{1}H NMR ($CDCl_3$, 500 MHz): δ = 8.19 (d, *J* = 8.0 Hz, 2H), 7.42 (d, *J* = 8.0 Hz, 2H), 6.00 (s, 2H), 4.36 (t, 2H), 3.41 (t, *J* = 6.5 Hz, 4H), 2.56 (s, 6H), 1.87-1.84 (m, 4H), 1.37 (s, 6H), 1.43-1.30 (m, 10H) ppm. ^{13}C NMR ($CDCl_3$, 125 MHz): *δ* = 166.0, 155.9, 142.9, 140.2, 139.7, 136.5, 131.1, 130.9, 130.4, 130.2, 128.4, 128.1, 124.5, 121.4, 65.5, 64.8, 29.2, 28.6, 25.9, 14.6, 14.5, 14.4, 14.2 ppm.

5,5-difluoro-10-(4-(((10-(methacryloyloxy)decyl)oxy)carbonyl)phenyl)-1,3,7,9-tetramethyl-5H-dipyrrolo[1,2-c:2',1'-f][1,3,2]diazaborinin-4-ium-5-uide(22) Compound **32** (160 mg, 0.27 mmol), acrylic acid (116 mg, 1.34 mmol), K_2CO_3 (746 mg, 5.4 mmol) and KI (890 mg, 5.36 mmol) were suspended in CH_3CN and the reaction was stirred at 50 °C for 4 days. After cooling the suspension was filtered and the solvent was removed under vacuum. The residue was then dissolved in CH_2Cl_2 and washed with water (3 x 100 mL). The organic layer was then dried over Na_2SO_4 and evaporated to remove the solvents. The obtained crude was purified by column chromatography (EtOAc : Hexane 1 : 9) to yield 136 mg (84% yield) of **22** as a red solid. ^{1}H NMR ($CDCl_3$, 500 MHz): δ = 8.19 (d, *J* = 8.0 Hz, 2H), 7.41 (d, *J* = 8.5 Hz, 2H), 6.10 (s, 1H), 5.99 (s, 2H), 5.54 (s, 1H), 4.36 (t, *J* = 7.0 Hz, 2H), 4.14 (t, *J* = 6.5 Hz, 2H), 2.56 (s, 6H), 1.94 (s, 3H), 1.81 (m, 2H), 1.68 (m, 2H), 1.47 (m, 2H), 1.37 (s, 6H), 1.33 (m, 10H) ppm. ^{13}C NMR ($CDCl_3$, 125 MHz): *δ* = 166.0, 155.9, 142.9, 140.2, 137.7, 136.5, 131.1, 130.9, 130.4, 130.2, 128.4, 128.1, 121.5, 121.4, 65.5, 64.9, 64.8, 29.2, 28.6, 28.5, 25.9, 14.6, 14.5, 14.4, 14.2 ppm.

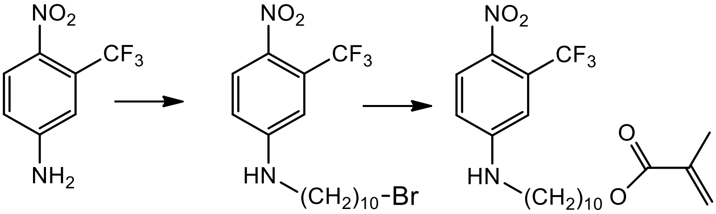

33 **23**

N-(10-bromodecyl)-4-nitro-3-(trifluoromethyl)aniline (33)

4-Nitro-3-(trifluoromethyl)aniline (2 g, 9.77 mmol) in a 250 ml round botton flask was dissolved in CH_3CN (100 mL). Then Cs_2CO_3 (2.7 g, 8.32 mmol) and excess of 1,10-dibromodecane (8.32 g, 0.027 mol) were added to the solution, and the reaction was carried out at reflux for 5 days. After cooling the mixture was filtered, and the solution was evaporated and purified by means of silica gel column chromatography (hexane/EtOAc 5 : 1) to give a pale yellow solid **33** (2.5 g, 60% yield). ^{1}H NMR ($CDCl_3$, 500 MHz): δ = 8.04 (d, *J* = 9.0 Hz, 1H), 6.87 (s 1H), 6.65 (d, *J* = 8.5 Hz, 1H), 4.62 (s, 1H), 3.42 (t, *J* = 7.0 Hz, 2H), 3.22 (m, 2H), 1.86 (m, 2H), 1.67 (m, 2H), 1.43 (m, 4H), 1.31 (m, 8H) ppm. ^{13}C NMR ($CDCl_3$, 125 MHz): *δ* = 151.8, 129.2, 123.3, 121.1, 112.3, 111.1, 43.4, 34.0, 32.7, 29.37, 29.32, 29.2, 28.9, 28.6, 28.1, 26.1 ppm. (Note: CF_3 tertiary C not observed).

10-((4-nitro-3-(trifluoromethyl)phenyl)amino)decyl methacrylate (23)

Compound **33** (500 mg, 1.17 mmol), K_2CO_3 (322 mg, 2.35 mmol) and KI (390 mg, 2.35 mmol) were suspended in DMF (5 ml). Then methacrylic acid (100 mg, 1.17 mmol), was added to the suspension and the reaction was stirred for 3 h at 70 °C. After cooling, the mixture was poured in water, extracted with EtOAc, and the organic phase was washed with brine. The solvent was removed under vacuum condition and the residue was purified by silica gel column chromatography (hexane/EtOAc 5: 1) to give compound

23 as yellow powder (346 mg, 70% yield). ^{1}H NMR (CDCl$_3$, 500 MHz): δ = 8.04 (d, *J* = 9.0 Hz, 1H), 6.87 (s, 1H), 6.65 (d, *J* = 9.0 Hz, 1H), 6.10 (s, 1H), 5.55 (s 1H), 4.59 (broad s, 1H), 4.15 (t, *J* = 6.5 Hz, 2H), 3.22 (m, *J* = 7.0 Hz, 2H), 1.95 (s, 3H), 1.65-1.69 (m, 4H), 1.32-1.41 (m, 12H) ppm. ^{13}C NMR (CDCl$_3$, 125 MHz): *δ* = 151.8, 136.5, 129.2, 125.2, 121.1, 118.7, 112.3, 111.1, 64.7, 43.4 (x2), 29.38, 29.36, 29.2, 29.1, 28.9, 28.5, 26.9, 25.9, 18.3 ppm. (Note: CF$_3$ tertiary C not observed).

***N*-hexyl-4-nitro-3-(trifluoromethyl)aniline (28)**

4-Nitro-3-(trifluoromethyl)aniline (500 mg, 2.42 mmol) was dissolved in acetonitrile (20 mL) and hexyl iodide (2 mL, 9.68 mmol) was added. The reaction mixture was stirred at reflux for 5 days. The solvent was removed under vacuum and the solid was purified by preparative TLC (CH$_2$Cl$_2$/hexane 7:3). ^{1}H-NMR (CDCl3): δ 0,91 (t, 3 H, J = 6.8 Hz, CH$_3$), 1,33 (m, 4 H, 2 × CH$_2$), 1,41 (m, 2 H, J = 6,8 Hz, CH$_2$), 1,66 (m, 2 H, J = 7,2 Hz, CH$_2$), 3,21 (m, 2 H, J = 6.8 Hz, NCH$_2$), 4,58 (1 H, br t, NH), 6,63 (1 H, dd, J = 2,5, J = 9,0 Hz, ArH), 6,86 (1 H, d, J = 2,5 Hz, ArH), 8,02 (1 H, d, J = 9,0 Hz, ArH).

6.3.2. Polymers Synthesis general procedure

Methacrylate monomers, comprising different molar (see tables in paragraph 5.1.), were added to a Carius reaction vessel together with poly(ethylene)glycol methacrylate in anhydrous tetrahydrofuran. Approximately 0.3 molar ratio of free radical generator 1,10Azobis(cyclohexanecarbonitrile) (AICN): polymer was also added to the vessel. After three consecutive freeze-pump-thaw cycles the reaction vessel was sealed under vacuum at 80 °C for 72 h. Hexane (60 ml) was added and the contents centrifuged at 6000 rpm for 5 min, the supernatant was discarded and the resulting pellet re-dissolved in THF:hexane 90:10. This was repeated 3 times. The resulting pellet was dried under vacuum to leave the resultant amphiphilic co-polymers (**21**, **25**, **26**, **27**) as an oil.

6.3.3. Preparation of polymerosomes entrapping non-polar guest

Polymerosomes with different quantities of guest were prepared using 1 ml of polymer solubilized in chloroform solution (1, 5 and 10 mg/ml) (phase1) then were added a suitable concentration of non-polar guest in $CHCl_3$. The mixture was stirred with vortex and sonicated for 3-5 minutes. The solutions were evaporated to dryness, purged with nitrogen flux, obtaining thin film which was suspended in 1 ml of dry chloroform and treated in vortex and sonicator for 5 minutes. A further 1 ml (1, 5 and 10 mg/ml) of polymer in PBS (phase 2) was added and the solution was sonicated using a Branson 3510 bath sonicator (230V) at room temperature for 25 min. The organic solvent was removed from the emulsion under reduced pressure at 40 °C and then the polymerosome solution was diluited at the final concentration with PBS and filtered with 0.45 µm filter.

6.3.4. Preparation of micelles

For the preparation of the micelles entrapping nitric oxide photoprecursor, compound **28** (different amount) was firstly dissolved in methanol and slowly evaporated to form a thin film. The film was then hydrated with a phosphate buffer solution of **21** (1 mg/ml). The mixture was stirred for 2 days at room temperature and then filtered with 0.45 µm filter.

The amount of **28** entrapped in the micelles and polymersomes after filtration was determined spectrophotometrically at 396 nm (ε = 10.000 M^{-1} cm^{-1}). Encapsulation efficiency (EE %) was calculated using the formulae below:

$$EE\ \% = (W_{IN}/W_i) \times 100$$

where W_{IN} is the amount of drug in the nanoassembly, W_i is the total amount of drug added during preparation.

6.3.5. Instrumentations

Spectra ^1H and ^{13}C NMR of were recorded on a Varian 500 and 125 MHz, respectively.

UV-Vis spectra absorption and fluorescence emission spectra were recorded with a Varian Cary Eclipse UV spectrophotometer and a Varian Cary Eclipse Fluorescence spectrophotometer, respectively, in air-equilibrated solutions, using either quartz cells with a path length of 1 cm.

Irradiation of the samples in solution was performed in a thermostated quartz cell (1 cm pathlength, 3 mL capacity) under gentle stirring, by using a continuum laser with λ_{exc} = 405 nm (ca. 100 mW) having a beam diameter of ca. 1.5 mm or with UVP UVGL-58 lamps, operating at 365 nm – 6 Watt (0.4 mW cm^{-2}).

DLS measurements of assembly of and zeta potential measurements of all systems were performed with a ZetaSizer NanoZS90 Malvern Instrument (UK), equipped with a 633 nm laser. (Scattering angle = 90°, T = 25 °C).

Biological assay was performed irradiating cell with UVP UVGL-58 lamps, operating at 365 nm – 6 Watt (0.4 mW cm^{-2}).

Antibacterial experiments were performed with 150 W Xenon Lamps equipped with a cut-off filter at *crc* 400 nm.

The fluorescence of the cells was detected by LUMIstar Omega plate reader.

Fluorescence images of cells were collected with a Nikon Eclipse E400 microscope.

NO release for samples in solution was measured with a World Precision Instrument, ISO-NO meter, equipped with a data acquisition system, and based on direct amperometric detection of NO with short response time (< 5 s) and sensitivity range 1 nM – 20 µM. The analog signal was digitalized with a four-channel recording system and transferred to a PC. The sensor was accurately calibrated by mixing standard solutions of $NaNO_2$ with 0.1 M H_2SO_4 and 0.1 M KI according to the reaction:

$$4H^+ + 2I^- + 2NO_2^- \rightarrow 2H_2O + 2NO + I_2$$

Irradiation was performed in a thermostated quartz cell (1 cm pathlength, 3 mL capacity) using the above continuum laser with λ_{exc} = 405 nm. NO measurements were carried out under stirring with the electrode positioned outside the light path in order to avoid NO signal artefacts due to photoelectric interference on the ISO-NO electrode.

6.3.6. *Antibacterial experiments*

The day before performing the experiments, pure cultures were inoculated in 100 mL of Mueller Hinton Broth (MHB) and incubated (37° C) to allow complete growth in the liquid growth medium. The overnight incubated broth culture was centrifuged at 10000 rpm for 20 minutes. Supernatant (MHB) was discarded leaving bacterial pellet at the bottom of the centrifuge tube. PBS was added to the tube and the bacterial pellet was washed by shaking it gently and resospended in 30 ml. The washed pellet was again centrifuged at 10000 rpm for 20 minutes. The pellet thus formed was then diluted with PBS. For experiment, bacteria (100 µL) were inoculated in 96 well plate to yield a final inoculums of ca. 2.5-6.5 × 105 CFU/mL.

Then 100 µL of PBS, **21**, **27**, **21·28**, and **27·28** were added giving a half concentration of the inoculated bacteria. For all experiments a control sample was also prepared in PBS. Before exposure to light, the samples to be irradiated were incubated in dark for 15 minutes at room temperature. 20 µL of each sample was taken and seeded as a spot in a ground plate of Mueller Hinton supplemented with agar (time t0). Irradiation was performed with a Xenon Lamp 150 W mounting a cut-off filter at crc 400 nm irradiating for 10, 20 and 30 minutes. The light source was designed in such a way so as to fit over the 5 cm culture plate with a fixed distance of irradiation of 4 cm. At different time, 20 µL of each sample were taken and seeded as a spot in a ground plate of Mueller Hinton supplemented with agar and 20 µL also were taken to count cells by serial dilutions. The viability count for each sample was done in duplicate plates.

6.3.7. Biological assay

Cell growth inhibition assays were carried out using cervical HeLa and pancreatic BxPc3 cancer cell lines. Hela and BxPc3 cells were cultured in DMEM and RPMI nutrient mixture respectively, supplemented with Fetal Bovine Serum (10%), Penicillin Streptomycin and non-essential Amino Acids. After reaching confluence, the cells were harvested by trypsinization and seeded in triplicate in 96 well plates at a density of 104 cells in 100 µl and left overnight at 37°C with 5% CO2. Cells were then washed twice with 100 µl PBS, then 100 µl of fresh media and 100 µl of polymersomes solution were added. Untreated cells were placed in every plate as a negative control. After 20 h of incubation the solution was removed and the cells were washed and left in PBS for the irradiation. The photocytotoxicity experiments were carried out by irradiating cells, incubated with photoactive components, with the irradiation source described above for 40 min. After the treatment PBS was removed and the cells were incubated with 180 µl of fresh medium. Cell viability was measured after 24 h. After incubation time 120 µL solution of MTT (5 mg/ml) were added. After three hours of incubation, the MTT solution was removed and 200 µL of DMSO were added to convert the MTT solution into a violet colored formazane. The solution absorbance, proportional to the number of live cells, was measured by spectrophotometer at 570 nm.

General conclusions

In this thesis, we have successfully integrated photoactivable molecules, by covalent or not covalent approach, in two different nanocarriers obtaining long-time and thermo-stable solutions under physiological conditions which can exhibit specific functions only in the presence of light.

In the first part it has been demonstrated that calixarene supramolecular systems represent interesting and versatile platforms to vehicle photostimulable molecules. The calixarene acts as a nanocontainer preserving the photodynamic properties of the PSs, and amplifing, in some cases, the NO photogeneration.

In the second part it has been demonstrated that polymersomes, due to their peculiar structure, show a very remarkable cellular uptake and are able to entrap hydrophobic and hydrophilic guests at the same time, allowing to transport in biological environment larger amount of drugs and pro-drugs than micelles.

Novel nanosystems able to elicit a significant light-dependent biocidal effect on bacteria and/or on cancer cells have been obtained.

Biocompatibility, cell penetrability, and light-controlled spatio-temporal generation of cytotoxic agents make the obtained systems promising for application in nanomedicine.

Publications

Antitumoral and antimicrobial activity of photostimulable polymersomes nitric oxide releasing. Ivana Di Bari, Nino Marino, Victor Irorere, Ibrahim Banat, Salvo Sortino and Bridgeen Callan. **2018** (BEING DEVELOPED).

***Simultaneous supramolecular activation of NO photodonor/ photosensitizer ensembles by a calix[4]arene nanoreactor*.** Ivana Di Bari, Giuseppe Granata, Grazia M. L. Consoli and Salvatore Sortino. *New J. Chem.* **2018**, 42, 18096-18101.

Electroneutral polymersomes for combined cancer chemotherapy. Noorjahan Aibani, Heather Nesbitt, Nino Marino, Joanna Jurek, Caolin O' Neill, Chloe Martin, Ivana Di Bari, Yingjie Sheng, Kieran Logan, Susan Hawthorne, Anthony McHale, John F. Callan, and Bridgeen Callan. *Acta Biomater.*, **2018**, 80, 327-340.

Design, Synthesis, and Antibacterial Activity of a Multivalent Polycationic Calix[4]arene–NO Photodonor Conjugate. Grazia M. L. Consoli, Ivana Di Bari, Anna R. Blanco, Antonia Nostro, Manuela D'Arrigo, Venerando Pistarà and Salvatore Sortino. *ACS Med. Chem. Lett.*, **2017**, 8, 881–885.

Supramolecular activation of the photodynamic properties of porphyrinoid photosensitizers by calix[4]arene nanoassemblies. Ivana Di Bari, Aurore Fraix, Roberta Picciotto, Anna R. Blanco, Salvatore Petralia, Sabrina Conoci, Giuseppe Granata, Grazia M. L. Consoli and Salvatore Sortino. *RSC Adv.*, **2016**, 6, 105573-105577.

A bactericidal calix[4]arene-based nanoconstruct with amplified NO photorelease. Ivana Di Bari, Roberta Picciotto, Giuseppe Granata, Anna R. Blanco, Grazia M. L. Consoli and Salvatore Sortino. *Org. Biomol. Chem.*, **2016***,* 14, 8047-8052.

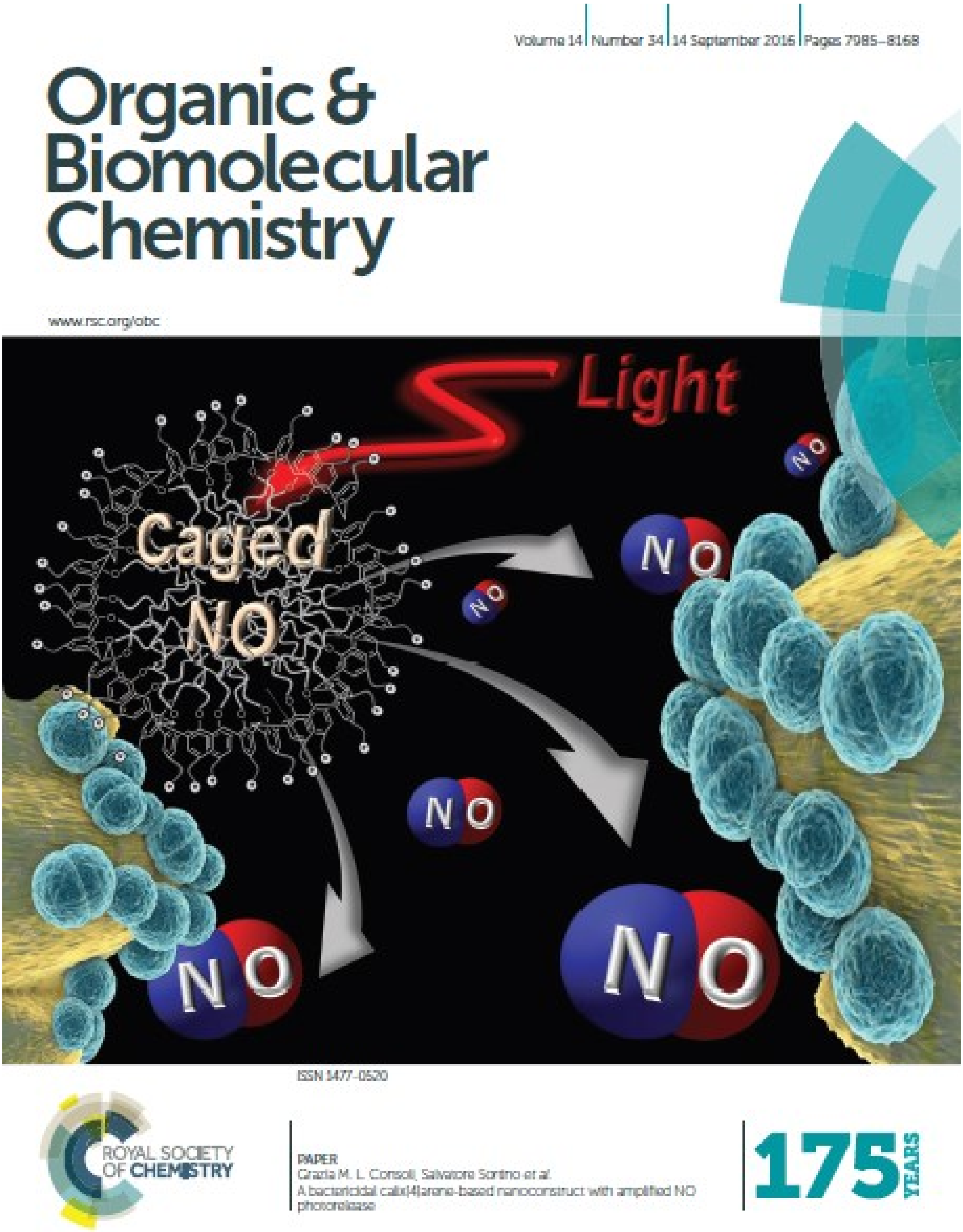

Volume 14 | Number 34 | 14 September 2016 | Pages 7985–8168

Organic & Biomolecular Chemistry

www.rsc.org/obc

ISSN 1477-0520

PAPER
Grazia M. L. Consoli, Salvatore Sortino et al.
A bactericidal calix[4]arene-based nanoconstruct with amplified NO photorelease

Acknowledgements

I would like to thanks firstly my supervisors Prof. Salvatore Sortino and Dr. Grazia Consoli for mentoring me, advising me and for making me a better woman passionate about science.

Thanks to Dr. Aurore Fraix and Dr. Marta Pèrez-Lloret…it is always amazing spending time with you in lab and beyond.

Thank you to Dr. Giuseppe Granata for helping me in lab during these three years and for your advices.

Thanks to all the people and researchers who work at ICB-CNR for making me feel good in these years and for your esteem and support.

Thanks to Dr. Bridgeen Callan for her kindness and for welcoming me in your research group, allowing me to become more than a chemist. Thank you to Dr. Noorjahan Aibani for your help and disposability.

Thank you also to Prof. John Callan, Dr. Federica Foglietta, Dr. Sukanta Kamila, Dr. Simanpreet Dhillon and Dr. Heather Nesbitt for time spent together.

Thank you to Prof. Ibrahim Banat and to all the lovely people who work with you, Dr. Victor Irorere, Dr. Lakshmi Tripathi, Nidhal Boutalbi, Dr.Lidia Ruiz and Abdulaziz juma Al Tamimi, for teaching me, for believing in me and in the possibility that I could learn more than I imagined in the world of microbiology.

Thanks to Dr. Davide Schiroli and Dr. Eleonora Maurizi, Dr. Diego Cobice, Dr. Valeria Cenini…you always will have a special place in my heart.

A particular thanks to Dr. Barry Hyland and his family, Wendy, Oscar and Toby…thank you for becoming part of our family.

I would like to thanks deeply all the people who somehow contributed to this thesis work: Dr. Roberta Picciotto, Dr. Anna Rita Blanco (Alfa Intes ITS), Dr. Antonia Nostro and Dr. Manuela D’Arrigo (University of Messina), for antibacterial test; Dr. Sabrina Conoci and Dr. Salvatore Petralia (ST Microelectronics), for AFM studies; Professors Gasco and Fruttero ant their research groups (University of Turin), for the synthesis of same samples.

Thanks to my PhD colleagues Noemi, Giuseppe, Gabriele e Antonella…it was a very pleasure make this journey together with you!

Thanks to my colleagues and friends Giacomo, Alessandra, Silvia, Erica, Enrico, Elena and Bobby, because despite the distance, I know that you will always be there and for spending a lot of time on phone/Skype with me and listening to my complaints! Also, thank you Enrico for picking me up every day when I was sick!

Thanks to ADI Catania DIRETTIVO group: Carlo, Enrico, Max, Carmela, Giulia, Giancarlo, Nadia and Pillo, for all the efforts and sacrifices made…you are amazing people.

Thanks to my parents, my parents in law, sisters and brothers, and to all my family for your support…because your hugs and your words make me a better person every day. Thank you to my little nephews Francesco, Beatrice, Sofia, Greta and Lorenzo…because your smiles make everything lighter.

Last but not least, thank you to my husband, friend, colleague and sometime teacher, Nino…you are my rock, my force and my support…thank you…without you all this would not have been possible…we are a very great team!

References

---

[1] X.Dai, Z. Fan, Y. Lu, P. C. Ray, *Appl. Mater. Interfaces.*, **2013**, 5, 11348.

[2] K. Lang, J. Monsinger, D.M. Wagnerovà, *Coord. Chem. Rev.*, **2004**, 248, 321.

[3] MM. Gottesman, *Annu. Rev. Med.*, **2002**, 53, 615.

[4] D. I. Andersson, D. Hughes, *Nat. Rev.*, **2010**, 8, 260.

[5] J. O'Neill, *Review on Antimicrobial Resistance* **2014**.

[6] J. O'Neill, *Review on Antimicrobial Resistance* **2016**.

[7] D.B. Buxton, *Wiley Interdiscip. Rev. Nanomed. Nanobiotechnol.* **2009**, 1, 149.

[8] K. Morris, *Lancet Infect. Dis.*, **2009**, 9, 215.

[9] A. Nazem, G.A. Mansoori, *J. Alzheimers Dis.*, **2008**, 13, 199.

[10] P. Couvreur, C. Vauthier, *Pharm. Res.*, **2006**, 23, 1417.

[11] A. Fraix, N. Marino, S. Sortino, *Topics Curr. Chem.*, **2016**, 370, 225.

[12] C.P. McCoy, C. Brady, J.F. Cowley, S.M. McGlinchey, N. McGoldrick, D.J. Kinnear, G.P. Andrews, D.S. Jones, *Expert Opin. Drug Deliv.*, **2010**, 7, 605.

[13] Á. Juarranz, P. Jaén, F. Sanz-Rodríguez, J. Cuevas, S. González, *Clin. Transl. Oncol.,* **2008**, 10, 148.

[14] C.M. Allen, W.M. Sharman, J.E. vanLier, *J. Porphirins Phathalocyanines*, **2001**, 5, 161.

[15] G. M. Fioramonti Calixto, J. Bernegossi, L. Marise de Freitas, C. R. Fontana, M. Chorilli, *Molecules*, **2016**, 21, 342.

[16] A. Fraix, N. Kandoth, S. Sortino, *Photochemistry*, **2013**, 41, 302.

[17] S. Moncada, R. M. Palmer, E. A. Higgs, *Pharmacol. Rev.,* **1991**, 43, 109.

[18] D. Tomasian, J. F. Keaney, J. A. Vita, *Cardiovasc. Res.,* **2000**, 47436.

[19] E. M. Battinelli, J. Loscalzo, *Nitric Oxyde and the Cardiovascular System,* **2000**, 8, 123.

[20] (a) P.A. Brennan, *Eur. J. Surg. Oncol.,* **2000**, 26, 434; (b) M. B. Grisham, D. Jourd' heuil, D. A. Wink, *Am. J. Physiology,* **1999**, 276, 315.

[21] (a) K. S. Kristopherson, D. S. Bredt, *J. Clin. Invest.,* **1997**, 100, 2424; (b) D. S. Bredt, *Free Rad. Res.,* **1999**, 31, 577.

[22] N. Ieda, Y. Hotta, N. Miyata, K. Kimura, H. Nagakawa, *J. Am. Chem. Soc.,* **2014**, 136 (19), 7085.

[23] (a) D. Fukumura, S. Kashiwagi, R. K. Jain, *Nat. Rev. Cancer*, **2006**, 6, 521;(b) S. Mocellin, V. Bronte, D. Nitti, *Med. Res. Rev.*, **2007**, 27, 317

[24] (a) C. Nathan, J. B. Hibbs, *Curr. Opin. Microbiol.,* **1991**, 3, 65; (b) E. Bonfoco, D. Krainc, M. Ankarcrona, P. Nicotera, S. A. Lipton, *Proc. Natl. Acad. Sci.,* **1995**, 927162; (c) B. Mitrovic, L. J. Ignarro, H. V. Vinters, M. A. Akers, I. Schmid, C.

Uittenbogaart, *Neuroscience,* **1995**, 65, 531; (d) M. W. Walker, M. T. Kinter, R. J. Roberts, D. R. Spitz, *Pediatr. Res.,* **1995**, 37, 41.

[25] (a) P. G. Wang, M. Xian, X. Tang, X. Wu, Z. Wen, T. Cai, A. J. Janczuk, *Chem. Rev*., **2002**, 102, 1091; (b) D. A. Riccio, M. H. Schoenfisch, *Chem. Soc. Rev*., **2012**, 41, 3731.

[26] A. Bishop, J. E. Andderson, *Toxicology*, **2005**, 208, 193.

[27] (a) C. D. Gutsche, *Royal Society of Chemistry*, Cambridge, **1989**, 210; (b) J. Vicens, J. M. Harrowfield, L. Baklouti, *Calixarenes in the Nanoworld*, **2007**.

[28] S. B. Nimse, T. Kim, *Chem. Soc. Rev*., **2013**, 42, 366.

[29] X. Ma, Y. Zhao, *Chem. Rev*., **2015**, 115,77.

[30] V. Saluja, B. S. Sekhon, *J. Pharm. Educ. Res*, **2013**, vol. 4.

[31] a) Y. Zhou, H. Li, Y.-W. Yang, *Chinese Chem. Lett.,* **2015**, 26, 825; b) G. M. L. Consoli, G. Granata, *Org. Biomol. Chem.*, **2011**, 9, 6491.

[32] A. Yousaf, S. Abd Hamid, N. M Bunnori, A. Ishola, *Drug Design, Development and Therapy*, **2015**, 9, 2831.

[33] Y. Cakmak, T. Nalbantoglu, T. Durgut, E. U. Akkaya, *Tetrahedron Lett.*, **2014**, 55, 538.

[34] M. Neagu, R.-M. Ion, G. Manda, C. Constantin, E. Radu, Z. Cristu, *Rom. J. Biochem*., **2010**, 47, 17.

[35] C. Tu, L. Zhu, P. Li, Y. Chen, Y. Su, D. Yan, X. Zhu, G. Zhou, *Chem. Commun.,* **2011**, 47, 6063.

[36] H. Yan, X. Pan, M. H. Chua, X. Wang, J. Song, Q. Ye, H. Zhou, A. T. Y. Xuan, Y. Liu, J. Xu, *RSC Adv.*, **2014**, 4, 10708.

[37] a) E. Wanigasekara, C. Gaeta, P. Neri, D. M. Rudkevich, *Org. Lett.,* **2008**, 10, 1263.; b) E. Wanigasekara, A. V. Leontiev, V. G. Organo, D. M. Rudkevich, Eur. J. *Org. Chem.,* **2007**, 14, 2254.

[38] G. Pasparakis, T. Manouras, M. Vamvakaki, P. Argitis, *Nat. Commun*., **2014**, 5, 3623.

[39] A. Bangham, *Chem. Phys. Lipids*, **1993**, 64, 275.

[40] C. Martin, E. Dolmazon, K. Moylan, C. Fowley, A. P. McHale, J. F. Callan and B. Callan, *Int. J. Pharm.*, **2015**, 481, 1.

[41] M. Alibolandi, F. Sadeghi, S.H. Sazmand, S.M. Shahrokhi, M. Seifi, F. Hadizadeh, *Int. J. Pharm. Invest.*, **2015**, 5, 134.

[42] J. Xu, Q. Zhao, Y. Jin, L. Qiu, *Nanomedicine*, **2014**, 10, 349.

[43] C. Martin, N. Marino, C. Curran, A. P. McHale, J. F. Callan and B. Callan, *Int. J. Pharm.*, **2016**, 511,570.

[44] L. Xu, M.F. Wempe, T. J. Anchordoquy, *Ther. Deliv.*, **2011**, 2, 451.

---

[45] S. Kolli, S.-P. Wong, R. Harbottle, B. Johnston, M. Thanou, A.D. Miller, *Bioconjug. Chem.*, **2013**, 24, 314.

[46] J.S. Lee, J. Feijen, *J. Control Release*, **2012,** 161, 473.

[47] Z.Y. He, B.Y. Chu, X.W. Wei, J. Li, C.K. 3rd Edwards, X.R. Song, G. He, Y.M. Xie, Y.Q.Wei, Z.Y. Qian, *Int. J. Pharm.*, **2014**, 469, 168.

[48] A. Magarkar, E. Karakas, M. Stepniewski, T. Róg, A. Bunker, *J. Phys. Chem. B*, **2012**, 116, 4212.

[49] P. K. Eggers, T. Becker, M. K. Melvin, R. A. Boulos, E. James, N. Morellini, A. H. Harvey, S. A. Dunlop, M. Fitzgerald, K. A. Stubbs, C. L. Raston, *RSC Adv.*, **2012**, 2, 6250.

[50] A. R. Blanco, M. L. Bondì, G. Cavallaro, G. M. L. Consoli, et al., WO2016055976 A1, **2016**; (b) R. V. Rodik, A.-S. Anthony, V. I. Kalchenko, Y. Mely, A. S. Klymchenko, *New J. Chem*., **2015**, 39, 1654.

[51] (a) E. B. Caruso, S. Petralia, S. Conoci, S. Giuffrida, S. Sortino, *J. Am. Chem. Soc.*, **2007**, 129, 480; (b) S. Conoci, S. Petralia, S. Sortino, EP 2051935A1/US20090191284, **2006**.

[52] L. Howe, J. Z. Zhang, *J. Phys. Chem. A,* **1997**, 101*,* 3207.

[53] F. Hoffmann, J. Cinatl, H. Kabickov´a, J. Kreuter and F. Stieneker, *Int. J. Pharm.*, **1997**, 157, 189.

[54] F. Wilkinson, W. P. Helman, A. B. Ross, *J. Phys. Chem. Ref. Data,* **1993**, 22, 113.

[55] 20 R. Bonnett, P. Charlesworth, B. D. Djelal, S. Foley, D. J. McGarvey, T. G. Truscott, *J. Chem. Soc.*, *Perkin Trans. 2*, **1999**, 325.

[56] W. Spiller, H. Kliesch, D. W. Herle, S. Hackbarth, B. R. DER, G. Schnurpfeil, *J. Porphyrins Phthalocyanines*, **1998**, 2, 145.

[57] A. Ogunsipe, J.-Y. Chen, T. Nyokong, *New J. Chem*., **2004**, 28, 822.

[58] I. Laville et al., *Bioorganic & Medicinal Chemistry*, 11, **2003**, 1643–1652

[59] Y. Chin et al., *PLOS ONE*, 9, **2014**, e97894.

[60] L. Huang, X. Yu, W. Wu, J. Zhao, *Org. Lett.*, **2012**, 14, 2594.

[61] A. P. Darmanyan, *J. Phys. Chem. A,* **1998,** 102*,* 9833.

[62] L. Huang, J. Zhao, S. Guo, C. Zhang, J. Ma**,** *J. Org. Chem*. **2013**, 78, 5627.

[63] F. W. Kotch,V. Sidorov,Y.-F. Lam,K. J. Kayser,H. Li,M. S. Kaucher, J. T. Davis**,** *J. Am. Chem. Soc*., **2003**, 125, 15140.

[64] I. Di Bari, R. Picciotto, G. Granata, A. R. Blanco, G. M. L. Consoli, S. Sortino, *Org. Biomol. Chem.*, **2016**, 14, 8047.

[65] N. Aibani ,P.F. da Costa, J. Masterson, N. Marino, F.M. Raymo, J. Callan, B. Callan., *J. Control. Release*., **2017**, 264, 136.